

**A REAL-TIME FINE PARTICULATE MATTER MONITOR BASED ON INERTIAL
SIZE-SEPARATION AND OPTICAL DETECTION IN A MICROCHANNEL**

by

LEON CHING FUNG YUEN

B.A.Sc., The University of British Columbia, 2012

A THESIS SUBMITTED IN PARTIAL FULFILLMENT OF
THE REQUIREMENTS FOR THE DEGREE OF

MASTER OF APPLIED SCIENCE

in

THE FACULTY OF GRADUATE AND POSTDOCTORAL STUDIES
(Mechanical Engineering)

THE UNIVERSITY OF BRITISH COLUMBIA

(Vancouver)

April 2015

© Leon Ching Fung Yuen, 2015

ABSTRACT

Exposure to fine particulate matter smaller than 2.5 μm in diameter (PM 2.5) is linked to increased mortality and morbidity. The real-time monitoring of PM 2.5 has important applications in indoor and outdoor air quality monitoring including occupational environments. However, commercially available real-time instruments are bulky and expensive, not suitable for personal exposure level monitoring.

This thesis presents a real-time, miniaturized PM 2.5 monitor which consists of a microfluidic-based particle trapping impactor and a forward light scattering optical detector with a 3D-printed housing. The particle trapping impactor channel includes a 90° turn, where larger particles experience a greater inertial force and enter and become captured in the particle trapping region. The detector, positioned downstream from the separator, illuminates the sized particles with a focused laser beam and detects light scattered by the particles using a photodiode to obtain the particle count.

The baseline geometry of the impactor is designed according to conventional impactor design methods and analytical calculations. The geometry is further optimized through an iterative process by simulating the flow velocity and particle behavior in the microchannel to obtain the sorting efficiency. The fabricated impactor channel is tested by transmitting particles from 0.5 to 3 μm through the device and is shown to have a 50% cut-off diameter of around 3 μm . The experimental sorting efficiency curve agrees with simulation-based predictions.

The arrangement of the detection system is optimized based on Mie scattering intensity and ray tracing calculations. Inexpensive, commercially available components are selected by modeling the optical power of scattered light on the photodiode surface. The detector is tested in parallel with a commercial instrument and shows good correlation at 1 minute sampling interval

for 2 μm particles. The measured pulse peak voltage and pulse width agree with the theoretical calculations. The integrated device requires a 10 minutes sampling time for a statistically significant measurement due to particle loss at the interface between the separator and detector. The experimental results demonstrate the potential of using microfluidics as a platform for a low-cost, real-time portable PM 2.5 sensor.

PREFACE

Part of the work in this thesis related to the design of the microfluidic particle trap impactor design (Chapter 2) and the optical detector (Chapter 3), the experimental setup (Chapter 5) and test results (Chapter 6) have been published [Yuen L, Chu WC, Stoeber B (2014) Microfluidic-Based Real-Time Detector For Fine Particulate Matter. Proceedings of the 13th Annual IEEE Conference on Sensors, Valencia, Spain, Nov. 2-5, 2014, pp. 775-778]. I was the lead investigator, responsible for the design, fabrication, experimental setup, data collection and analysis, and manuscript composition. Chu WC and Stoeber B provided supervisory feedback throughout the project. Stoeber B also contributed to manuscript edits.

A US Provisional Patent Application (No. 62/073811) has also been filed on October 31st, 2014 on the design of the microfluidic particle trap impactor. Materials from Chapter 2 and Chapter 6 are included in the application. I conducted all the theoretical calculations and simulations in the impactor design process and generated all the figures and experimental data.

TABLE OF CONTENTS

ABSTRACT.....	ii
PREFACE.....	iv
TABLE OF CONTENTS.....	v
LIST OF TABLES.....	x
LIST OF FIGURES.....	xi
LIST OF SYMBOLS.....	xvii
1 Introduction.....	1
1.1 Particulate Matter.....	1
1.1.1 Risks in PM Exposure.....	2
1.1.2 PM Regulatory Standards.....	3
1.1.3 Need for Real-time Personal Exposure PM Monitoring.....	3
1.2 Particle Separation.....	4
1.2.1 Overview of Separation Method.....	4
1.2.2 Inertial Separation.....	5
1.2.3 Separation in a Microchannel.....	7
1.3 Particle Detection.....	8
1.3.1 Detection Methods.....	8
1.3.2 Miniaturized Particle Detectors.....	9
1.4 Project Overview.....	11

2	Design of Separation System.....	13
2.1	Stochastic Model of Particle Counting.....	13
2.1.1	Expected Particle Counts	13
2.1.2	Poisson Process.....	14
2.1.3	Poisson Confidence Limit.....	15
2.1.4	Flow Rate Optimization.....	15
2.2	Impactor Design	18
2.2.1	Theory of Operation.....	19
2.2.2	Slip Correction Factor.....	20
2.2.3	Particle Relaxation Time and Stopping Distance	21
2.2.4	Stokes Number and Reynolds Number at Nozzle.....	23
2.2.5	Analytical Model	23
2.2.6	COMSOL Simulation	26
2.2.1	2D vs 3D Simulation Comparison	34
3	Design of Detection System.....	41
3.1	Particle Detection	41
3.1.1	Light Scattering Theory	41
3.1.2	Amplitude Scattering Function.....	43
3.1.3	Optical System Design.....	45
3.1.4	Coincidence Error	55

3.1.5	Design Optimization	57
4	Device Fabrication	60
4.1	Microfluidic Impactor	60
4.1.1	SU-8 Mold	60
4.1.2	PDMS Channel	62
4.2	Optical Detector	64
4.2.1	Optical Enclosure.....	64
4.2.2	Light Trap	65
4.2.3	Optical Component Assembly	66
4.3	Integrated Device	67
5	Experimental Setup and Design.....	68
5.1	Particle Generation System	68
5.1.1	Collison Nebulizer	69
5.1.2	Particle Suspension	70
5.2	Impactor Test Setup	70
5.2.1	Penetration Efficiency Test Setup.....	71
5.2.2	Particle Loss Characterization Test Setup	72
5.3	Real-time Detector and Integrated Device Test Setup.....	73
5.3.1	Data Acquisition and Analysis.....	73
5.3.2	Experiment Test Setup.....	73

6	Results and Discussion	76
6.1	Impactor Characterization	76
6.1.1	Penetration Efficiency.....	76
6.1.2	Particle Deposition.....	78
6.1.3	Effect of Humidity	81
6.1.4	Particle Re-entrainment	82
6.2	Particle Loss Characterization at Device Interface	83
6.3	Particle Pulse Characteristics of Detector	84
6.4	Real-time Detector Characterization.....	86
6.4.1	2 μm Test Particles	87
6.4.2	1.5 μm Test Particles	90
6.4.3	1 μm Test Particles	91
6.4.4	Counting Efficiency	94
6.5	Integrated Device	95
6.5.1	2 μm Test Particles	95
6.5.2	1 μm Test Particles	97
7	Conclusions and Future Work	99
7.1	Conclusions	99
7.1.1	Particle Separation	99
7.1.2	Particle Detection.....	100

7.2	Future Work	102
7.2.1	Experimental Setup.....	102
7.2.2	Impactor Design.....	103
7.2.3	Detector Design	104
	BILIOGRAPHY	105
	APPENDIX A – Impactor Width W_i Simulation Data.....	114

LIST OF TABLES

Table 1- Summary of Stochastic model parameters	18
Table 2 –Knudsen number and slip correction factor for desired particle range	21
Table 3 - 50% cut-off diameter and slope of S_0 simulation results.	38
Table 4 -50% cut-off diameter and slope of W_n simulation results.....	39
Table 5 –Summary of impactor geometry design.....	40
Table 6 - Signal pulse width of particles for varying channel widths with 0.5 L/min flow rate and 0.5 mm channel height h_c	46
Table 7- Optical power calculation for forward and 90° scattering.....	52
Table 8 - Optical power of the forward scattering system and the expected output voltage after signal conditioning circuit.....	55
Table 9 - Comparison of original forward scattering system and modified scattering system.....	59
Table 10 - Optical power of the forward scattering system and the expected output voltage after signal conditioning circuit.....	59
Table 11 - Summary of polystyrene suspension concentration	70
Table 12 - Penetration efficiency test measurement order.....	72
Table 13 - Particle loss test order for 3 test cases: detector, straight channel and combined	73
Table 14 - Summary of APS measured diameter.....	77
Table 15 – Average particle loss percentage for 3 test cases : detector, straight channel and combined.....	84
Table 16 - Peak voltage signal of particle pulses - Theoretical vs Experimental Average	85
Table 17 - Summary of detector test parameters and counting efficiency for 1, 1.5 and 2.0 μm diameter.....	95
Table 18 - Current specification of the optical detector	101

LIST OF FIGURES

Figure 1 - Typical particle distribution expressed as a percentage of total suspended particles [11]	2
Figure 2 - Inertial method - a) impactor, b) virtual impactor and c) cyclone [29].....	5
Figure 3 - Penetration efficiency curve - ideal vs typical	6
Figure 4 - Overview of detection system - particle trapping impactor (Left), optical particle counter (Right)	11
Figure 5 - Poisson probability distribution function for expected number of counts $N = 5, 20$ and 50	14
Figure 6 - Mass error (Left) and relative error (Right) for sampling time $t = 1$ to 10 minutes , flow rate = 500 mL/min, Red line indicates error requirements of $0.5 \mu\text{m}/\text{m}^3$ or 5%	17
Figure 7 – Required time to satisfy error requirement at mass concentration - Flow rate = 500 mL/min.....	17
Figure 8 - Critical dimension of the particle trapping impactor	18
Figure 9 - Balance of centrifugal force and viscous force acting on the particle making the turn	20
Figure 10 - Stopping distance of particles, $V_g = 10 \text{ m/s}$	22
Figure 11 – Outlet angle ϕ_{out} of $45^\circ, 90^\circ$ and 135°	24
Figure 12 - Radial displacement of particles for outlet angle ϕ_{out} of $45^\circ, 90^\circ$ and 135° at $V_g = 30$ m/s.....	25
Figure 14 – Sample simulated flow velocity profile, tapered outlet.....	28
Figure 15 - Schematic of the inertial focusing inlet.....	29
Figure 16- Penetration efficiency for sample device	30
Figure 17 - Acceleration inlet with round corners- 30, 45, 60, 75 degrees (Left to right)	31

Figure 18 – X position standard deviation for inlet focusing angles 15 °, 30°, 45 °,60 °, 75 ° and 90 °	32
Figure 19 – Transmission probability for inlet focusing angles 15 °, 30°, 45 °,60 °, 75 ° and 90 °	33
Figure 20 - Flow velocity profile of 75 degree inlet.....	34
Figure 21 - Flow velocity profile of the device : 2D (Left) , 3D (Right).....	35
Figure 22 - Transmission ratio of impactor: 2D vs 3D.....	35
Figure 23 - Flow velocity field for Distance to Impactor $S_0 = 0.5 W_0, W_0$ and $1.5 W_0$. (Left to right) (Not to same colour scale)	36
Figure 24 – Penetration efficiency for $S_0 = 0.5 W_0$ for freeze, 50% freeze and bounce wall condition	36
Figure 25- Penetration efficiency for $S_0 = W_0$ for freeze, 50% freeze and bounce wall condition	37
Figure 26 - Penetration efficiency for $S_0 = 1.5 W_0$ for freeze, 50% freeze and bounce wall condition	37
Figure 27 – Flow velocity field, streamline (left) and position of deposited particles for bounce wall condition (right) in the particle trapping region.....	38
Figure 28 - Light scattering angle θ	42
Figure 29 – Amplitude scattering function $[S_n(\theta)]^2$ for 2.5 μm diameter particles , $n_{\text{medium}} = 1.00027$, $n_{\text{particle}} = 1.5$, $\lambda = 650 \text{ nm}$	43
Figure 30 - Amplitude scattering function $[S_n(\theta)]^2$ for 1 μm diameter particles, $n_{\text{medium}} = 1.00027$, $n_{\text{particle}} = 1.5$, $\lambda = 650 \text{ nm}$	44
Figure 31 - Amplitude scattering function $[S_n(\theta)]^2$ for 0.5 μm diameter particles, $n_{\text{medium}} = 1.00027$, $n_{\text{particle}} = 1.5$, $\lambda = 650 \text{ nm}$	44

Figure 32 - Amplitude scattering function $[S_n(\theta)]^2$ for 1.5 μm diameter particles - Red, green and blue incident light source	45
Figure 33 – Sensing region within the flow channel	46
Figure 34 - Forward light scattering system, exaggerated light trap	48
Figure 35 - 90° scattering system	48
Figure 36 - OSLO ray tracing simulation for forward scattering	51
Figure 37 - Solidworks model of the 90° system.....	52
Figure 38 - Schematic of the signal conditioning circuit.....	54
Figure 39 - Maximum allowable concentration for 10% coincidence error at different flow rates	56
Figure 40 - Solid model of the original forward scattering system	57
Figure 41 - Flow streamline of the original forward scattering detection chamber (Left) and detection chamber with flow restricting aperature.....	58
Figure 42 - Modified forward scattering detector enclosure: cross section drawing (left) and flow simulation (right)	58
Figure 44 - Fabrication process of the PDMS microchannel.....	60
Figure 45 - SU-8 wafer of the microchannel	62
Figure 46 - Fabrication of inlet port - side view of PDMS device	63
Figure 47 - Microfluidic particle trapping impactor	64
Figure 48 - Assembly of the detector.....	66
Figure 49 - Integrated device: microfluidic impactor attached to detector enclosure	67
Figure 50- Schematic of experiment setup	68
Figure 51 - 1.5 μm particle count over 1 hour	69
Figure 52 - Straight channel device	71

Figure 53- Ideal particle output from nebulizer for real-time continuous test.....	75
Figure 54 - Penetration efficiency curve of particle trap impactor: experiment vs COMSOL simulation.....	76
Figure 55 - Microscope image of florescent 1 μm particles after a) 1 minute, b) 5 minutes, c) 10 minutes and d) 20 minutes.	79
Figure 56 - Microscope image of florescent 2.5 μm particles after a) 1 minute, b) 5 minutes, c) 10 minutes and d) 20 minutes.	80
Figure 57 - Penetration efficiency curve of particle trap impactor: Simulation vs experiment for wet and dry particles	81
Figure 58 - Penetration efficiency data from failed microfluidic impactor	82
Figure 59 - Sample pulse from the detector - 1.5 μm (Left) vs ambient air particle (Right)	84
Figure 60 - Pulse voltage histogram for 1 μm test particles	85
Figure 61 - Pulse voltage histogram for 1.5 μm test particles	86
Figure 62 - Pulse voltage histogram for 2 μm test particles	86
Figure 63- APS size distribution of test particles from 2 μm polystyrene suspension, two peaks at 1.843 and 2.839 μm	87
Figure 64 - Detector count vs APS reference count of larger peak centered at 2.839 μm for 2 μm particle suspension- Left: 1 minute sampling interval, Right: Average count at each particle concentration, error bars represents ± 1 standard deviation.	88
Figure 65 - Detector count vs APS reference count of smaller peak centered at 1.843 μm for 2 μm particle suspension- Left: 1 minute sampling interval, Right: Average count at each particle concentration, error bars represents ± 1 standard deviation.	89

Figure 66 - Count levels of detector and APS measurement of 1.843 and 2.839 μm diameter peaks for 2 μm particle suspension over entire test period normalized to the average concentration of the highest particle concentration 89

Figure 67 - APS size distribution of test particles from 1.5 μm polystyrene suspension 90

Figure 68 - Detector count vs APS reference count for 1.5 μm particle suspension- Left: 1 minute sampling interval, Right: Average count at each particle concentration, error bars represents ± 1 standard deviation. 90

Figure 69 - Count levels of detector and APS measurement 1.5 μm particle suspension over entire test period normalized to the average concentration of the highest particle concentration 91

Figure 70 - APS size distribution of test particles from 1.0 μm polystyrene suspension 92

Figure 71 - Detector count vs total APS reference count for 1 μm particle suspension- Left: 1 minute sampling interval, Right: Average count for each particle concentration, error bars represents ± 1 standard deviation..... 92

Figure 72 - Detector count vs APS reference count larger than 2.129 μm diameter for 1 μm particle suspension- Left: 1 minute sampling interval, Right: Average count at each particle concentration, error bars represents ± 1 standard deviation. 93

Figure 73 – Count levels of detector and APS measurement for 1 μm particle suspension over entire test period normalized to the average concentration of the highest particle concentration 94

Figure 74 – Integrated device count (impactor and detector) vs total APS reference count for 2 μm particle suspension - Left: 1 minute sampling interval, Right: Average count for each particle concentration, error bars represents ± 1 standard deviation. 96

Figure 75 - Count levels of integrated device and APS measurement for 2 μm particle suspension over entire test period normalized to the average concentration of the highest particle concentration..... 96

Figure 76 - Integrated device count (impactor and detector) vs total APS reference count for 1 μm particle suspension - Left: 1 minute sampling interval, Right: Average count for each particle concentration, error bars represents ± 1 standard deviation. 97

Figure 77 - Integrated device count (impactor and detector) vs APS reference count greater than 2.129 μm for 1 μm particle suspension - Left: 1 minute sampling interval, Right: Average count for each particle concentration, error bars represents ± 1 standard deviation. 98

Figure 78 - Count levels of integrated device and APS measurement for 1 μm particle suspension over entire test period normalized to the average concentration of the highest particle concentration..... 98

Figure 79 - Flow velocity field for Impactor width $W_i = W_0, 1.5 W_0$ and $2W_0$ (Not to same colour scale). 114

Figure 80 - Penetration efficiency for $W_i = W_0$ for freeze, 50% freeze and bounce wall condition 114

Figure 81 - Penetration efficiency for $W_i = 1.5W_0$ for freeze, 50% freeze and bounce wall condition 115

Figure 82 - Penetration efficiency for $W_i = 2 W_0$ for freeze, 50% freeze and bounce wall condition 115

LIST OF SYMBOLS

α	1 – confidence interval
α_c	Cunningham slip correction coefficient
α_p	Size parameter
β_c	Cunningham slip correction coefficient
γ_c	Cunningham slip correction coefficient
θ	Scattering angle
λ	Wavelength of light
λ_g	Mean free path of the gas
μ	Gas viscosity
ρ_g	Gas density
ρ_p	Particle density
τ	Particle relaxation time
φ_{acc}	Acceleration inlet angle
φ_{out}	Outlet angle
a	Flow channel width
B	Bandwidth
b	Flow channel height
C_c	Cunningham slip correction factor
C_d	Drag coefficient
C_{de}	Detector capacitance
C_f	Feedback capacitance
c	Particle concentration
D_H	Hydraulic diameter
d_s, d	Distance between particles and detector
Δd	Radial displacement
d_p	Particle diameter
E	Penetration efficiency
$e\%$	Relative percent error
e_{mg}	Mass concentration error
$F_{centrifugal}$	Centrifugal force
$F_{viscous}$	Drag force
$f_{.3dB}$	Corner frequency
GBP	Gain-bandwidth product
h_c	Detector channel height
I	Scattered light intensity
I_0	Incident light intensity
K	Wave number
Kn	Knudsen number
l_s	Sensing length
m	Relative refractive index

m_{conc}	Mass concentration
m_p	Particle mass
N	Particle count
N_H	Upper confidence limit
N_L	Lower confidence limit
NEP	Noise equivalent power
n_{air}	Air refractive index
n_{particle}	Particle refractive index
$n_{\text{particle},}$	Refractive index
P	Optical power
Q	Flow rate
Re	Flow Reynolds number
Re_p	Particle Reynolds number
R_f	Feedback resistor
r	Bend radius
r_d	Radius of detector
r_p	Particle radius
S	Stopping distance
S_0	Impactor outlet width (Distance to impactor)
$S_n(\theta)$	Chord length on circular detector at x
Stk	Stokes number
t	Sampling time interval
U	Terminal velocity of particle
V_g	Flow velocity
V_p	Particle velocity
W_i	Impactor entrance width
W_{inlet}	Acceleration inlet width
W_o	Impactor nozzle width
w_c	Detector channel width
x	Distance from center of detector
$y(x)$	Chord length on circular detector at distance x

1 Introduction

The environmental monitoring of particulate matter concentration is traditionally implemented by government agencies at sparsely distributed monitoring stations and does not provide any real-time personal exposure information. Existing commercial instruments for real-time sampling are bulky and expensive. With demonstrated applications in biological sensing for cell sorting and particle counting [1]–[3], microfluidics provides an ideal platform for a low-cost personal exposure monitor. This thesis investigates the feasibility and challenges of separating and detecting particles in a microfluidic channel. A miniaturized detector for particulate matter 2.5 μm or smaller (PM 2.5) is developed by adapting conventional design principles for particle separation and optical detection to a microscale device, which is then fabricated with microfabrication techniques.

1.1 Particulate Matter

Particulate matter describes the mixture of both solid particles and liquid droplets suspended in the air. Particulate matter can originate from a wide range of sources, for example, diesel exhausts from cars, metal particulates from mines or dust from farms. Consequently, the physical properties of a single particle such as size, density, shape and chemical composition can vary significantly. One of the most critical characteristics in determining the particle's behavior in air is the physical size of the particles. Particles with sizes comparable to gas molecules are sensitive to diffusion caused by Brownian motion. Due to its small size, motion can also be induced in a particle by relatively weak thermal and electrostatic forces. For larger particles, the interaction between the particle and the gas is dominated by inertial and viscous effects such as gravity and drag forces, respectively. To compare the size of particles of different shape and

density in motion, the aerodynamic diameter is used in which the particle is referenced to the diameter of a spherical particle with a density of 1000 kg/m^3 with an equivalent aerodynamic behaviour.

1.1.1 Risks in PM Exposure

PM 2.5 and PM 10 are particulate matter smaller than $2.5 \mu\text{m}$ and particulate matter smaller than $10 \mu\text{m}$ in aerodynamic diameter, respectively. When inhaled, PM 10 are likely to deposit in the tracheobronchial branch of the lungs while PM 2.5 can deposit in the respiratory bronchioles and alveoli where gas exchange occurs [4]. These particles can enter the blood stream and cause a wide range of significant cardiovascular and respiratory health issues [5]. Many recent cohort studies conducted around the world have consistently linked particulate matter exposure to increased mortality [6]–[8]. The short-term and long-term mortality increase is reported to be 0.4-1% and 6% per $10 \mu\text{g/m}^3$ [9]. An estimate of 223,000 annual lung cancer deaths worldwide is associated with air pollution [10]. The typical particle distribution of PM 2.5 and PM 10 for various emission sources expressed as a percentage of total suspended particles (TSP) is shown in Figure 1.

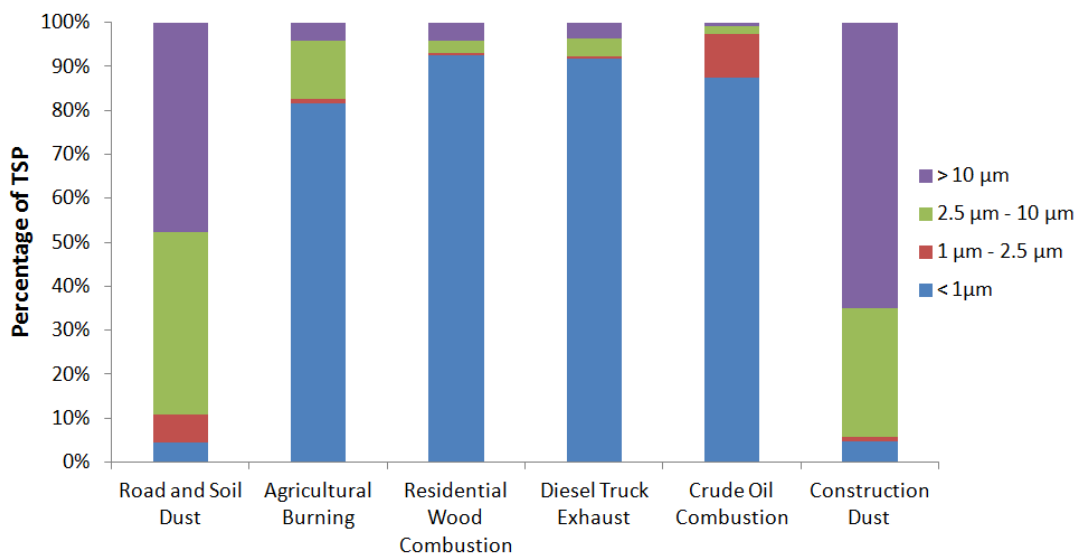


Figure 1 - Typical particle distribution expressed as a percentage of total suspended particles [11]

1.1.2 PM Regulatory Standards

The mass concentration of both PM 2.5 and PM 10 in the environment are closely monitored by government agencies. The World Health Organization recommends an annual PM 2.5 average exposure of $10 \mu\text{g}/\text{m}^3$ and a 24 hours average exposure of $24 \mu\text{g}/\text{m}^3$ [12]. The US Environmental Protection Agency (EPA) reduced its annual exposure limit of PM 2.5 from 15 to $12 \mu\text{g}/\text{m}^3$ in 2013 and estimated that \$4 to 9 billion annual health costs can be saved by meeting the new standard in 2020 [13].

Gravimetric analysis is the standard method accepted by the EPA for PM mass concentration measurements [14]. Air is drawn through a filter at a controlled flow rate and the mass of the captured particles is weighed to calculate the mass concentration. The process is very time-consuming and does not offer real-time concentration data.

1.1.3 Need for Real-time Personal Exposure PM Monitoring

Particulate matter concentration is directly related to human activities with urbanization being the primary cause for increased human exposure [14] [15]. This is especially problematic in developing countries where the government focus is in on economical and industrial development and environmental regulations are more lenient [16] [17]. For example, the daily average PM 2.5 mass concentration in Beijing, China is reported to be $75 \mu\text{g}/\text{m}^3$ in the month of January of 2013, exceeding the WHO recommended limit by 7 times [19]. Citizens often rely on air quality index readings provided by weather stations to determine whether it is safe to go outdoors. Because PM concentration is geographic dependent [20], a low-cost portable monitor will allow users to evaluate their exposure risk in their local environment.

Many occupations are at risk to high PM exposure even when the concentration level is not critically high because of prolonged hours in the work environment. Some examples include welders, farmers, miners and highway workers [21]–[23]. Due to the high cost of instruments, air

quality monitoring is rarely utilized in the workplace. Air quality studies are conducted by attaching sampling pumps to workers to capture particles for gravimetric analysis [23]. An inexpensive, real-time, portable PM monitor could be widely implemented, allowing workers to quickly identify and address hazards in the workplace.

One of the emerging features of sustainable buildings is a natural ventilation system. A natural ventilation system takes advantage of the natural movement of air due to indoor and outdoor temperature and pressure difference to reduce the requirements of the traditional HVAC system, hence, lowering energy cost. The stack effect in atriums and displacement ventilation systems which release cool air from the floor and rely on heat from occupants to circulate air in the space are common examples of natural ventilation [24]. However, indoor air quality (IAQ) in these buildings is heavily correlated with the outdoor environment due to the minimized effect of air filter from the HVAC system [25][26]. Outdoor air is still required to be treated if deemed unacceptable according to the ventilation for acceptable IAQ standard set by the American Society of Heating, Refrigerating and Air Conditioning Engineers [27]. The carbon dioxide level is often monitored and used as a feedback for the HVAC system [28]. There is a need for a low-cost, real-time PM monitor to provide a better metric of building health and IAQ.

1.2 Particle Separation

1.2.1 Overview of Separation Method

Particles are typically passed through a classification stage to separate PM 2.5 and PM 10 from other particle sizes. Inertial methods such as impactor, virtual impactor and cyclones are most commonly used for this size range [29]. The particles are sized by taking advantage of the exponential increase in particle mass and consequently the inertial force as the particle diameter increases. The inertial force on the particle overcomes the viscous drag force to drive the

particles onto an impaction plate for inertial impactors (Figure 2a), into a minor flow stream for virtual impactors (Figure 2b), and the walls of a collection cup for cyclones (Figure 2c).

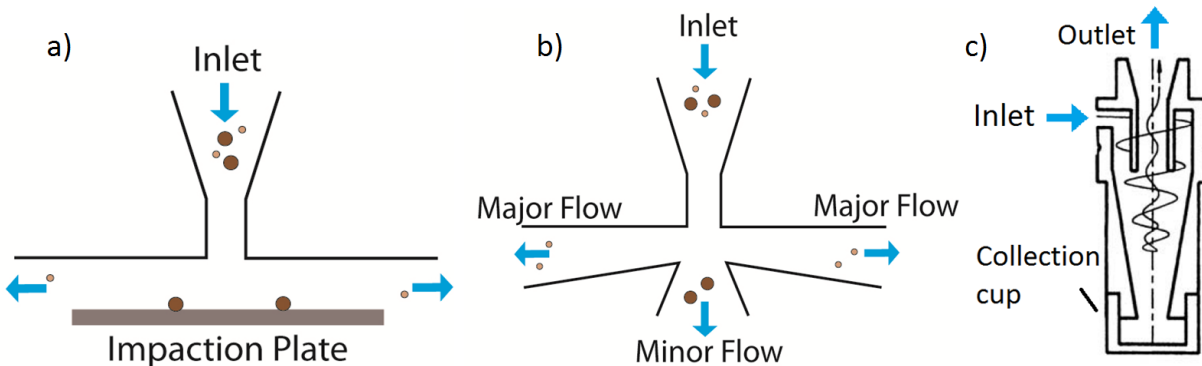


Figure 2 - Inertial method - a) impactor, b) virtual impactor and c) cyclone [29]

Inertial sizing of submicron range particles becomes difficult and requires the use of a microorifice or high flow velocity [30]. These particles are more commonly precipitated by inducing particle motion using thermophoresis and electrostatic forces [29][31]. Particles passing through a strong temperature gradient will move towards the cold direction as the air molecules strike the hotter side of particle with higher energy. This method is implemented in thermal precipitators using a simple heat source and a cold collection surface. In an electrostatic precipitator, particles are charged with a corona discharger and passed through a electric field to deposit the particles. For nanoparticles, the size distribution can be determined using diffusion batteries by passing sample air through a long tube or parallel plates of different lengths to collect the particles by diffusion [32].

1.2.2 Inertial Separation

Particle separation by inertial method is the most relevant for the size range of PM 2.5 and PM 10. Inertial impactors have been used extensively for a wide range of applications such as ambient air sampling, personal sampling and pharmaceutical applications [33]–[37]. Marpole et al. conducted the first theoretical study of impactors in 1973 by developing a mathematical

model based on Navier-Stokes to describe the flow field in an impactor [38] and provided a design guideline for the impactor geometry based on the desired 50% cut-off diameter [39]. The 50% cut-off diameter is defined as the aerodynamic particle diameter at which 50% of the particles are transmitted through the impactor denoted as d_{p50} . The penetration efficiency curve of impactors, which provides the percentage of particles transmitted through the impactor as a function of particle size, is used to compare impactor performance. A steeper slope of the cut-off curve around the 50% cut-off diameter represents a more effective impactor. Ideally all particles below the cut-off diameter are transmitted and all particles above the cut-off diameter are impacted (Figure 3). The collection efficiency, the inverse of the penetration efficiency, is also used interchangeably in literature for impactor evaluation.

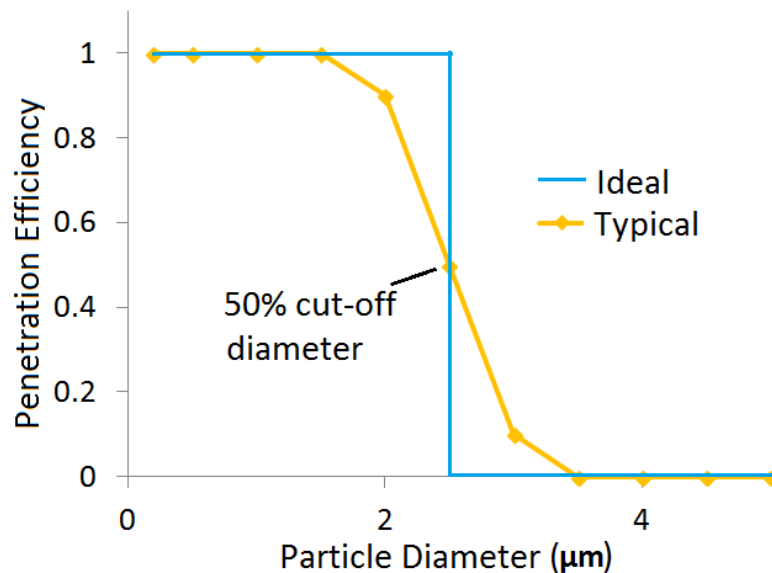


Figure 3 - Penetration efficiency curve - ideal vs typical

The slope of the penetration efficiency curve for inertial impactors is the sharpest of all impactors [40][41]. However, impaction oil is typically required on the impaction plate to improve particle adhesion. Inertial impactors suffer from particle re-entrainment as particles build up on the impaction plate over time [41].

The impacted particles in virtual impactors remain airborne and exit through the minor flow, allowing easy transport for analysis [42]. Virtual impactors also do not require impaction oil. However, to balance the minor and major flow, a delicate flow resistance balance or complex flow control is required. Virtual impactors also suffer from small particles exiting through the minor flow streamlines. The penetration curves of these devices are not as sharp compared to inertial impactor [40].

Biswas et al. developed the particle trap impactor which replaces the impaction plate with a cavity similar to a virtual impactor without the minor flow outlet [43]. The penetration efficiency is comparable to impactors with greased substrate with extended life-time until the trap is full. The flow complexity is also reduced compared to virtual impactors [44][45].

All impactors can be classified as a variation of these 3 types. In a cascaded impactor, many impactor stages with a different 50% cut-off diameter are connected in series to obtain the particle size distribution in the sample air [30]. A perforated plate often acts as a collection of jet orifices to achieve small particle diameter cut-off at a high sampling rate [46].

1.2.3 Separation in a Microchannel

While particles separation techniques are commonly used for biological applications to sort cells in microfluidics, the hydrodynamics of particles in water differs significantly from the aerodynamics of particles in air. Due to the higher viscosity of water and similar density of water and particles, the behavior of particles in water is very different from their behavior in air, and they are less likely to cross the flow streamlines in water due to inertial effects. The flow physics for particles suspended in water or air are fundamentally different; as a result the particle separation strategies that have been developed for water-based systems cannot be applied for air-based systems. The flow rate of the water-based devices are also in the $\mu\text{L}/\text{min}$ range [1].

Both the inertial impactor and the virtual impactor have been successfully miniaturized and tested in a microfluidic device [47]–[50]. The channel design of these prototype devices is fabricated on a silicon wafer by patterning SU-8 photoresist, not suitable for large scale production. Schaap et al. developed a microchannel design to size particles by centrifugal force around 180 ° curve [51]. The separation efficiency is 82% for 1.0 μm particles and 87% for 1.9 μm particles. However, this device requires sheath air to initially focus the particles to the center of the channel complicating operations. The flow rate of the separation device is also extremely low at 120 μL/min.

1.3 Particle Detection

1.3.1 Detection Methods

The alternative to measuring the mass of captured particles on a filter by gravimetric analysis is to measure mass indirectly using a semi-continuous method such as a tapered-element oscillating microbalance and a quartz crystal microbalance (QCM) [52]. Particles are accumulated on an oscillating structure and the resonant frequency shift is correlated to the particle mass, providing a time-integrated mass measurement. The disadvantage of these devices is it relies heavily on particle deposition. If the oscillation is too fast, particles will tend to flake off the device. The sensor can also be overloaded over time and requires cleaning or replacement.

Optical techniques are most commonly used for real-time measurements in commercial instruments [53]. The sample air path is illuminated by a high intensity light source and a photodetector senses the light scattered from the particles. This is the basic theory of operation for most commercial optical particle counters. The aerodynamic particle sizer (APS 3321, TSI) uses the time-of-flight information between two detectors to accurately determine the

aerodynamic size distribution of particles. Alternatively, with calibration to the particle's optical property, the handheld instrument Dustrak (8532, TSI) can correlate particle size to the intensity of the scattered light pulse [54]. The costs of these instruments have dropped significantly due to the rise of affordable laser diodes [55]. However, these instruments are typically large in size and still relatively costly, not suitable for personal exposure monitoring.

When the particle size is smaller than the wavelength of light, the scattered light intensity is weak and becomes difficult to detect. Nephelometers measure the concentration of small particles by illuminating a large volume of sample air. The voltage level measured by the photodiode is proportional to the light intensity collectively scattered by all the particles in the volume [56]. Condensation particle counters detect submicron particles by passing the sample air through a region of vapour supersaturation to induce condensation on individual particles until they reach a detectable size [57]. Alternatively, submicron particles can be detected electrically by first precipitating the particles by electrostatic force and measuring the charge on the sensing element [58]. Detecting particles electrically is typically only feasible for research and analytical purposes in laboratory environment as it requires a high voltage source and a sensitive current detector to operate.

1.3.2 Miniaturized Particle Detectors

Microelectromechanical system (MEMS) technology has been widely used to create compact, high sensitivity sensors such as accelerometer and pressure sensors. With the goal to develop a personal exposure monitor, microfabrication methods have been adapted to produce miniaturized particle detectors. Mass resonators are the most common class of devices. Similar to the macroscopic microbalance technique, particles are deposited on a vibrating structure, which is typically a piezoelectric element such as a surface acoustic wave device (SAW) [59] or a film bulk acoustic resonator (FBAR) [60] in MEMS. The vibrating structure can also be

actuated thermally [61]. The shift in resonant frequency corresponds to the mass of the particles. To obtain the mass concentration of the desired particle size range, the detection stage is preceded by a miniaturized particle separation stage such as a virtual impactor or an inertial impactor [62][63]. The sensitivity of these sensors is limited by the size of the oscillating structure relative to the particles. Particles which are not sufficiently large to cause a frequency shift cannot be detected. Conversely, particles much larger than the structure will easily overload the sensor. Depositing the particles on the microstructure is also very challenging. Thermal or electrostatic precipitation is used in some cases [560][64]. Like their macroscopic counterparts, the sensors need to be cleaned or replaced over time.

Electrical particle detectors to sense submicron particles have also been miniaturized. The concentration of naturally charged diesel particulates is sensed as they build up on a dielectric layer on a silicon wafer measuring the induced charge on the silicon [65]. A micro corona discharger tip is produced by anisotropically etching a masked silicon wafer [66][67]. By supplying a high voltage between the tip and the ground plane, the sample air and the particles are ionized and then captured on a HEPA filter. The induced current on the filter provides a time-integrated reading of mass concentration.

Optical detection in microfluidics is most commonly used for biological applications for flow cytometry or cell counting [3]. Although the basic detection theory is analogous to particle detection, the specimens are naturally fluorescent or labeled with dyes in biological analysis and the flow velocity of the fluid is much slower. Non-fluorescent detection is difficult in liquid due to the similarity in refractive index of cells and water. Li et al. fabricated an optical PM detection system in which the flow channels and the detection microchamber are etched from a silicon wafer [68]. The sample air passes through the microchamber consisting of a laser diode and a photodiode mounted at a right angle and the particle concentration is obtained using the

nephelometer approach. The device was tested with tobacco smoke at a high concentration of $300 \mu\text{g}/\text{m}^3$ and was able to only detect a small signal change of 55 mV. The fabrication of the detector requires an expensive deep reactive ion etching process and the device cannot sense individual particles.

1.4 Project Overview

The objective of this project is to develop a low-cost, real-time PM 2.5 personal exposure monitor. The design focus is on PM 2.5 because a functional PM 2.5 system can be more easily scaled up to detect PM 10. Our approach is to design a particle trapping impactor as part of a transporting micro-channel to size PM 2.5 particles (Figure 4 Left) and integrate with a simple optical particle detection system (Figure 4 Right). The microchannel flow path makes a 90° turn and large particles continue to travel straight into the particle trapping region due to their higher inertia. By replacing the impaction plate with a cavity, the particle trapping impactor aims to eliminate the need for impaction oil and reduces particle entrainment compared to inertial impactor designs. Compared to virtual impactors, particle loss through minor flow is eliminated and the operation of the device is simple. The microfluidic device will be integrated as a disposable cassette with the miniaturized, light scattering detection system. Since the particles are already sized, the goal of the detection system is to be able to count individual PM 2.5 particles using low cost components to obtain a high resolution, real-time measurement.

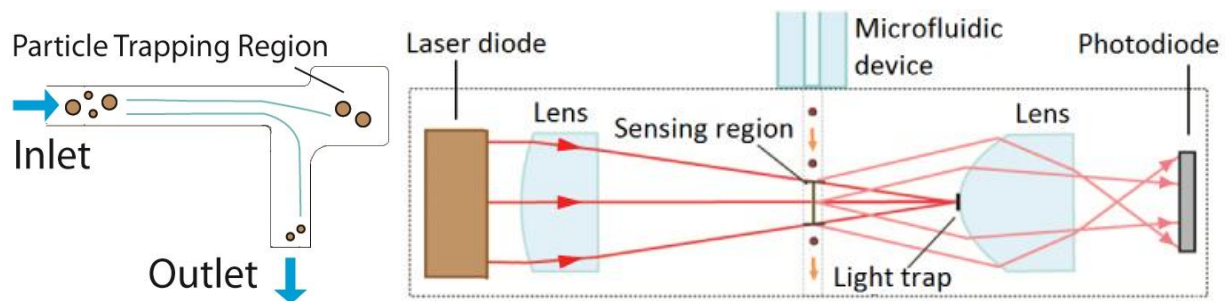


Figure 4 - Overview of detection system - particle trapping impactor (Left), optical particle counter (Right)

The theory of operation of the impactor channel is presented in Chapter 2. The stochastic model of particle counting, the analytical model of particle motion and the simulation of flow and particle to determine the parameters of the impactor are discussed. The theory of light scattering and its application to the particle detector is presented in Chapter 3. The theoretical optical power on the detector and expected signal are calculated to explore optical system alignment options. Chapter 4 describes the fabrication process of the microchannel and the assembly of the detector. The experimental setup to validate the separation and detection system is presented in Chapter 5. The experimental results are presented and compared to theoretical calculations in Chapter 6. The research contributions of this project and recommendations for future work are discussed in Chapter 7.

2 Design of Separation System

2.1 Stochastic Model of Particle Counting

The mass of a single particle increases for a larger particle size and for a higher mass density. Consequently, a lower particle count is expected for the same mass concentration of larger particles or particles of a higher density since there are fewer particles within the same volume. At the low detection limit of the system, the number of particle counts must be sufficiently high to obtain a statistically significant measurement. A stochastic model of particle count is used to calculate the minimum counts needed to satisfy the relative error and mass concentration error requirement. Based on this value and the minimum concentration detection limit, the required flow rate of the system is established.

2.1.1 Expected Particle Counts

At a fixed flow rate Q and particle number concentration c , the total expected number of particles N entering the detection system over sampling interval t is given by $N = cQt$. The particle number concentration

$$c = \frac{m_{conc}}{m_p} = \frac{m_{conc}}{\frac{\rho_p \pi d_p^3}{6}}, \quad (1)$$

defined by the mass concentration m_{conc} of particles and the mass of a single particle m_p , is a function of particle density ρ_p and particle diameter d_p . Since the particle concentration is inversely proportional to the cube of the particle diameter, the expected number of counts at the same mass concentration drops significantly as the particles increase in size. The low counts can be compensated by increasing the sampling time or the flow rate.

2.1.2 Poisson Process

Particle counting is modeled with the Poisson process where each particle entering the system corresponds to an independent event. The probability such that the total counts N hold the integer value k when the expected value of $N = cQt$ is given by the Poisson probability distribution

$$P(N = k) = \frac{e^{-cQt}(cQt)^k}{k!}. \quad (2)$$

The relative error, calculated by

$$e_{\%} = \frac{\Delta N}{N} = \frac{N_H/L - N}{N}, \quad (3)$$

where N_H and N_L are the respective upper and lower confidence limits, is high when the expected value of N is low due to a higher ratio between the difference between the confidence limits and the expected value ΔN compared to the expected value N . This can be seen from the Poisson probability distribution in Figure 5 by taking the difference between confidence limits and the expected value. The relative error is approximately 100% for $N = 5$ and 20% for $N = 50$.

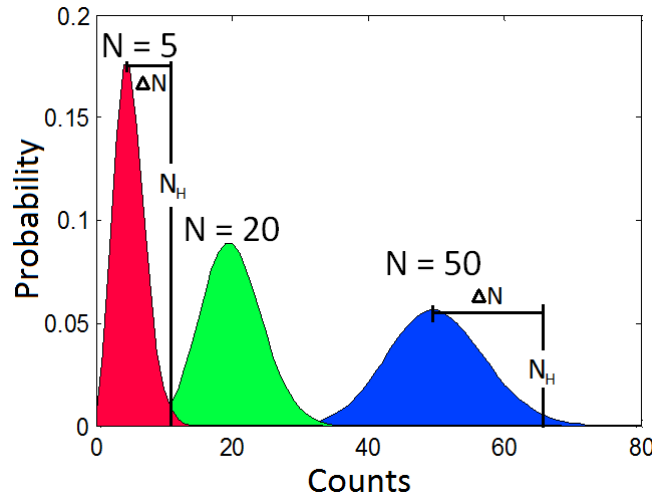


Figure 5 - Poisson probability distribution function for expected number of counts $N = 5, 20$ and 50 .

2.1.3 Poisson Confidence Limit

The upper and lower bounds of Poissons confidence interval can be computed with various methods. For large values of N, the Poisson probability distribution approaches the normal distribution and the confidence interval can be computed with normal approximation. For better accuracy at low counts, the chi-square and Poisson relationship

$$N_L = \frac{\chi_{2N+2,1-\alpha/2}^2}{2} \quad (4)$$

$$N_H = \frac{\chi_{2N,\alpha/2}^2}{2} \quad (5)$$

is used where N is the expected value and $\alpha = 1 - \text{Confidence Interval (C.I.)}$ [69]. For each count value N, the upper and lower relative error can be computed by calculating the upper and lower bounds of the Poissons confidence interval.

2.1.4 Flow Rate Optimization

The detection system is designed to meet the error requirements for 2.5 μm diameter particles, the largest size to be detected where the particle concentration is lowest. The minimum detection limit of the device is set at 1 $\mu\text{g}/\text{m}^3$ to provide good resolution below the WHO recommended limit of 10 $\mu\text{g}/\text{m}^3$. The initial error requirements are set to be $\pm 5\%$ or $\pm 0.5 \mu\text{g}/\text{m}^3$ with a 95% confidence interval. Because the percent error is difficult to satisfy due to the nature of the Poisson distribution, the mass concentration error requirement is included to accept measurement accurate to 0.5 $\mu\text{g}/\text{m}^3$. As a requirement for a real-time system, the maximum sampling time t is set to be 5 minutes.

For a fixed flow rate Q and sampling time t, the expected number of counts N is calculated for 2.5 μm particles for a range of mass concentrations starting at the detection limit of 1 $\mu\text{g}/\text{m}^3$. From the expected counts, the Poisson confidence limit is found using the chi-square relationship at each mass concentration value and the relative error $e_{\%}$ is determined. The mass concentration

error e_{mg} is solved by $e_{mg} = e_{\%} c$. The calculation is repeated for sampling time of 1 to 10 minutes for a range of flow rates to determine the minimum flow rate which satisfies the error requirements.

The mass concentration error satisfies the error requirements at low concentration but the error increases with increasing concentration or sampling time (Figure 6 Left). Conversely, the relative percent error meets the requirement at high concentration but increases for low concentration (Figure 6 Right). The concentration at which the calculated error curve crosses the error requirement is plotted for each sampling time shown in Figure 7. Above the relative error curve are the concentration values which satisfy the relative error requirements. Concentration values below the mass concentration error curve meet the error requirement.

500 mL/min is determined to be the minimum flow rate from the series of calculations which satisfies both error requirements after 5 minutes of sampling time. This corresponds to a required count N of 2600. Given $N = cQt$, the flow rate and the sampling time is inversely proportional and increasing the flow rate can reduce the sampling time further. However, the flow rate is minimized to reduce the requirements and size of the sampling pump. As a result, the flow rate for the detection system is set at 500 mL/min. A summary of the stochastic model parameters is shown in Table 1.

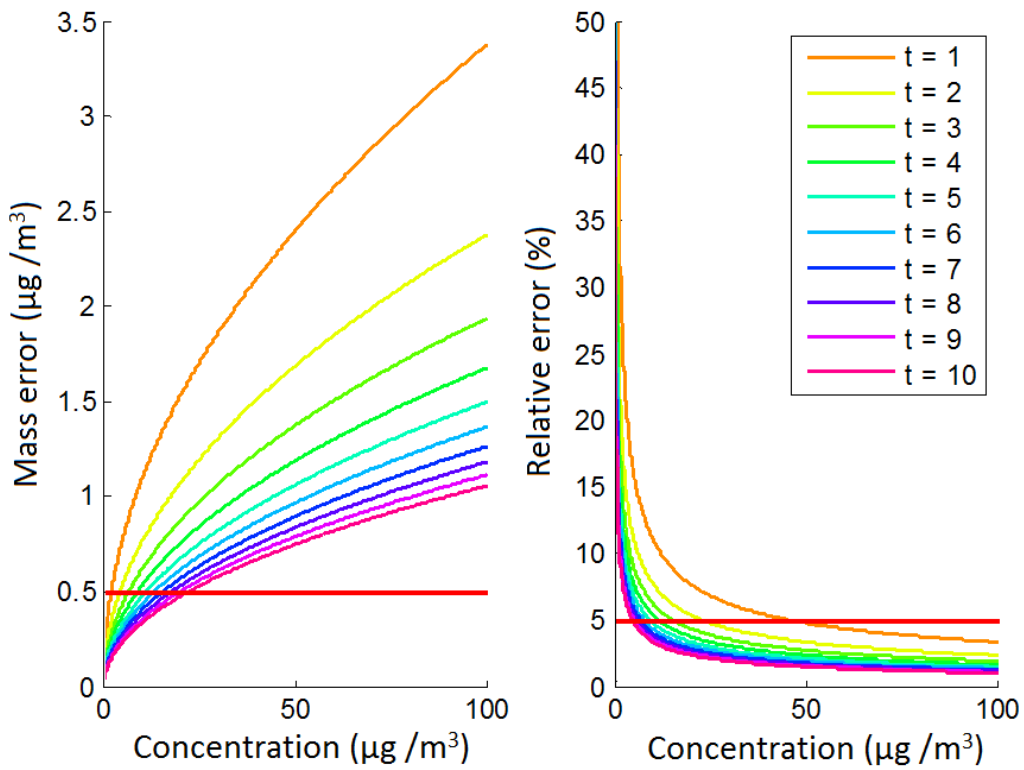


Figure 6 - Mass error (Left) and relative error (Right) for sampling time $t = 1$ to 10 minutes , flow rate = 500 mL/min, Red line indicates error requirements of $0.5 \mu\text{m}/\text{m}^3$ or 5%

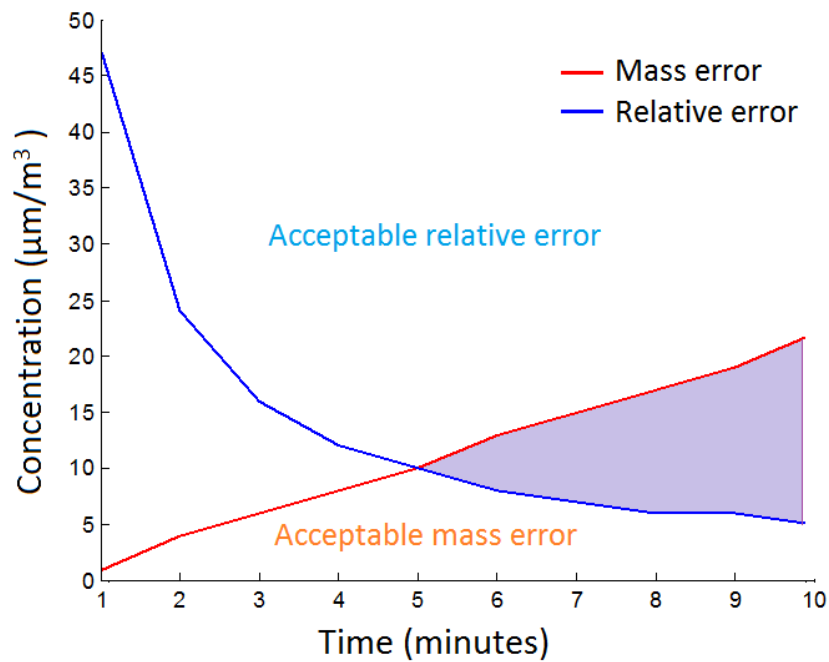


Figure 7 – Required time to satisfy error requirement at mass concentration - Flow rate = 500 mL/min

Table 1- Summary of Stochastic model parameters

Requirements	
Relative percent error	$\pm 5\%$
Mass concentration error	$\pm 0.5 \mu\text{g}/\text{m}^3$
Sampling time	5 minutes
Minimum detection limit	$1 \mu\text{g}/\text{m}^3$
Confidence interval	95%
Calculated Value	
Flow rate Q	0.5 L/min

2.2 Impactor Design

The target 50% cut-off diameter for the particle trapping impactor is $2.5 \mu\text{m}$ to size PM 2.5. The cut-off characteristic of the device is set by its geometry. The critical impactor dimensions include the nozzle width W_0 , the nozzle length L , the channel height h_0 , the distance to impactor S_0 , the impactor entrance width W_i and the outlet angle ϕ_{out} (Figure 8).

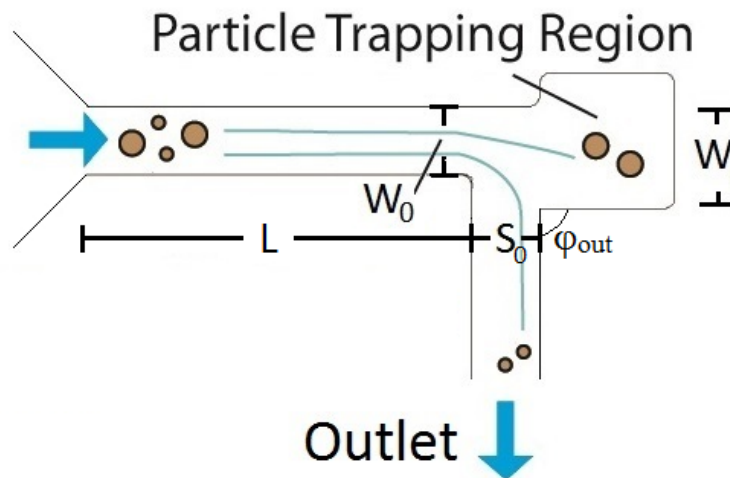


Figure 8 - Critical dimension of the particle trapping impactor

To design the impactor, an analytical model describing the particle motion is first developed by analyzing the forces on a particle as it makes a turn. The effect of the outlet angle ϕ_{out} , defined as the angle of the turn, on radial displacement and penetration efficiency is evaluated. The basic impactor dimensions such as the nozzle width W_0 and channel height h_0 are

set based on conventional impactor design theory. The distance to impactor S_0 and the impactor entrance width W_i are further optimized through an iterative process based on penetration efficiency obtained by simulating the fluid velocity profile and particle motion within the channel using computation fluid dynamics.

2.2.1 Theory of Operation

Particles making a turn experience a centrifugal inertial force, causing them to move outwards away from the center of the curved path to cross the flow streamlines. The centrifugal force is given by

$$F_{centrifugal} = \frac{m_p V_g^2}{r} = \frac{\pi \rho_p d_p^3 V_g^2}{6r} \quad (6)$$

where m_p is the mass of the particle, ρ_p is the density of the particle, r is the bend radius of the particle path, V_g is the flow velocity and d_p is the particle diameter. A viscous drag force acts on the particle to oppose the motion induced by the inertial force. The drag force is defined as

$$F_{viscous} = \frac{\pi}{8} C_d \rho_g U^2 d_p^2 \quad (7)$$

where C_d is the drag coefficient, ρ_g is the density of air and U is the particle velocity with respect to air. The drag coefficient is dependent on the dimensionless particle Reynolds number

$$Re_p = \frac{\rho_g U d_p}{\mu} \quad (8)$$

where μ is the viscosity of air. For small particles where $Re_p < 0.1$, the drag coefficient is defined by the empirical formula

$$C_d = \frac{24}{Re_p} \quad (9)$$

which simplifies the drag force expression to

$$F_{viscous} = 3\pi\mu U d_p, \quad (10)$$

commonly referred to as the Stokes' drag. Since the particle velocity V_p in the tangential direction is assumed to be the same as the flow (Figure 9), the terminal velocity U of the particle resulting from the balance of the forces is in the radial direction outwards.

The terminal velocity

$$U = \frac{1}{18} \left(\frac{\rho_p d_p^2 V_g}{r \mu} \right) \quad (11)$$

is solved by equating the drag force (equation 10) and the centrifugal force (equation 6). Because the terminal velocity U is proportional to the square of the particle diameter, a larger percent of particles will be driven into the particle trap region as the particle diameter increases.

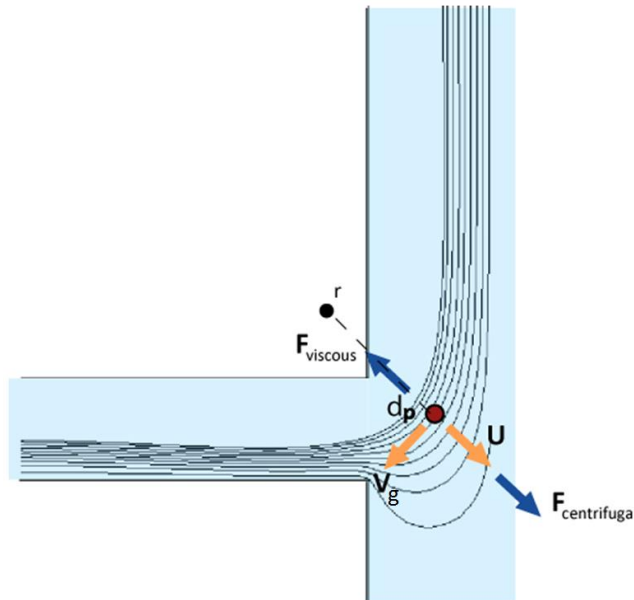


Figure 9 - Balance of centrifugal force and viscous force acting on the particle making the turn

2.2.2 Slip Correction Factor

The drag force given in equation 10 is for the continuum regime where the flow around the particles acts as a continuous medium. In cases where particles are small with respect to the mean free path of the molecules in the fluid, defined as the mean distance a molecule travels before collision with another molecule, the particles can travel between the molecules of the

fluid, reducing the effect of drag. The flow is in the slip regime for Knudsen number $Kn = \frac{2\lambda_g}{d_p}$

$\gg 1$, where λ_g is the mean free path of the fluid ($\lambda_g = 0.0665 \mu\text{m}$ for air in room temperature, atmospheric pressure), and continuum regime for $Kn \ll 1$. The slip correction factor

$$C_c = 1 + Kn[\alpha_c + \beta_c e^{-\frac{\gamma_c}{Kn}}], \quad (12)$$

where $\alpha_c = 1.142$, $\beta_c = 0.558$, $\gamma_c = 0.999$ [70] determined empirically, modifies the drag force to

$$F_{viscous} = \frac{3\pi\mu U d_p}{C_c}. \quad (13)$$

Table 2 –Knudsen number and slip correction factor for desired particle range

dp (um)	Kn	C_c
0.5	0.266	1.31
1	0.133	1.15
1.5	0.089	1.10
2	0.067	1.08
2.5	0.053	1.06

With the slip correction factor converging to 1, the effect of the slip flow on the drag force is negligible for particles to be impacted ($d_p > 2.5 \mu\text{m}$) as shown in Table 2.

2.2.3 Particle Relaxation Time and Stopping Distance

To understand how quickly the particles respond to the change of flow, the particle relaxation time $\tau = \frac{\rho_p d_p^2 C_c}{18\mu}$ can be derived from the particle equation of motion assuming

Stoke's drag on the particles:

$$F_{viscous} = m_p \ddot{x} = \frac{3\pi\mu d_p}{C_c} \dot{x} \quad (14)$$

$$C_c \frac{\pi\rho_p d_p^3}{6r} \ddot{x} = 3\pi\mu d_p \dot{x} \quad (15)$$

$$V_p(t) = V_g(1 - e^{-t/\tau}) \quad (16)$$

The relaxation time is defined mathematically as the time it takes for the particle velocity V_p to reach 63% of the fluid velocity V_g . The stopping distance S for particles

$$S = \tau V_g = \frac{\rho d_p^2 C_c V_g}{18\mu} \quad (17)$$

estimates the distance the particle with flow velocity V_g will travel before it comes to a stop.

The stopping distance of the particles increases exponentially as particle diameter increases as shown in Figure 10. The longer stopping distance indicates that the particles will enter the particle trapping region with increased efficiency as the particle size increases.

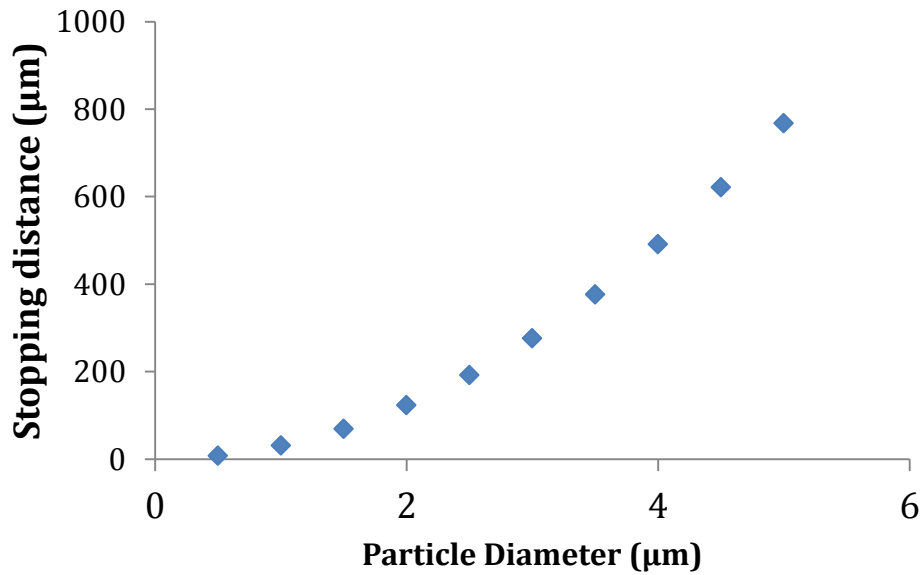


Figure 10 - Stopping distance of particles, $V_g = 10$ m/s

The same analysis can be applied to estimate the required acceleration distance of the particle to reach the velocity of the fluid to design the nozzle length L once the flow velocity of the microchannel is defined.

2.2.4 Stokes Number and Reynolds Number at Nozzle

The Stokes and Reynolds number are commonly used in the design of conventional inertial impactor. The Stokes number

$$Stk = \frac{\rho_p C_c V_g d_p^2}{9\mu W_o} \quad (18)$$

is the ratio of the stopping distance to the characteristic dimension, which is the nozzle width W_o for impactors. The Stokes number describes how well the particles follow the fluid streamlines.

The square root of the Stokes number $\sqrt{Stk_{50}}$ is commonly reported in impactor literature at which d_p in equation 18 is the 50% cut-off diameter. $\sqrt{Stk_{50}}$ is a function of the Reynolds number and typically ranges between 0.45 and 0.8 depending on the type of impactors [38][41][43][47].

The flow Reynolds number, which differs from the particle Reynolds number, is defined as

$$Re = \frac{\rho_g V_g D_H}{\mu} \quad (19)$$

where D_H is the hydraulic diameter given by $2ab/(a+b)$ for a rectangular channel with a width a and a height b . The Reynolds number at the nozzle is recommended to be between 500 – 3000 for a sharp size cut-off [39]. The height of the channel is limited by the fabrication process because SU-8 polymer molds are difficult to spin-coat and expose uniformly by photolithography for thicknesses above 600 μm . As a result, the channel height and the nozzle width of the device were set at 200 μm and 1700 μm respectively for the 50% cut-off diameter to be 2.5 μm at a flow rate of 500 mL/min to satisfy these initial design conditions.

2.2.5 Analytical Model

2.2.5.1 Radial Displacement of Particles

To more accurately estimate particle position after the bend, the radial displacement Δd of particles in the desired size range is calculated with the terminal radial velocity U by

$$\Delta d = U * t = \frac{1}{18} \left(\frac{\rho_p d_p^2 V_g^2}{r \mu} \right) \frac{2\pi r}{4} \frac{1}{V_g} = \frac{\pi \rho_p d_p^2 V_g}{2 * 18\mu} \quad (20)$$

where t is the time it takes the particles to travel around the bend. Time t is defined by the path of the particle, which is a quarter of the circumference for a 90° bend, and the tangential velocity of the particle. In this case, the expression differs from the stopping distance given in equation 17 by $\frac{\pi}{2}$. The radial displacement is independent of the radius of curvature of the particle path. The same calculation is repeated for 45° and 135° outlet angles (Figure 11) which increases or decreases the length of time it takes for the particles to be in the bend, consequently increasing or decreasing the angular displacement. With a rectangular channel of 200 by 1700 μm and a flow rate of 0.5 L/min, the average flow velocity is 24.5 m/s. Assuming the particle velocity is uniform along all streamlines in the channel, the radial displacement with an average velocity of 30m/s exponentially increase for larger particles shown in Figure 12 even though the relationship between the outlet angle and the radial displacement is linear. Consequently, the outlet angle provides another degree of freedom to set the cut-off diameter if necessary.

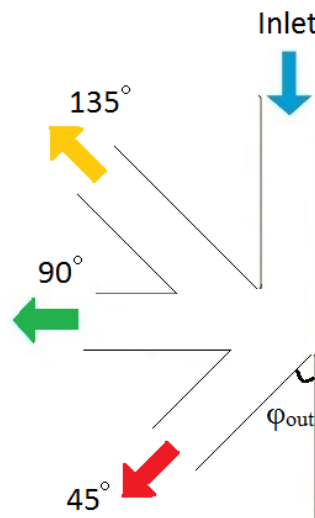


Figure 11 – Outlet angle ϕ_{out} of 45 °, 90 ° and 135 °

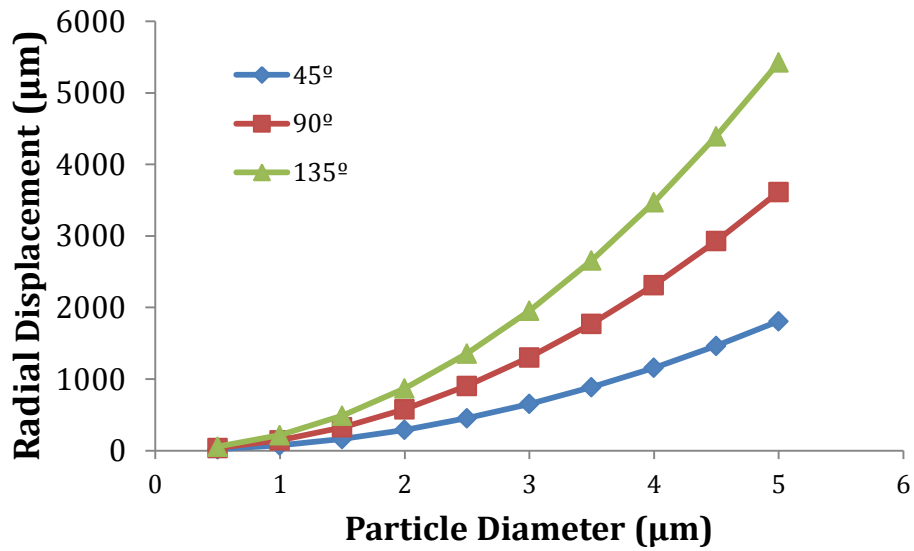


Figure 12 - Radial displacement of particles for outlet angle ϕ_{out} of 45°, 90° and 135° at $V_g = 30$ m/s

2.2.5.2 Penetration Efficiency

For each flow streamline along the width of the channel, if the radial displacement is greater than the distance between the particle and the particle trapping region, the particles can be assumed to enter the particle trapping region and are removed from the flow. As such, the penetration efficiency is estimated by the expression $E = 1 - \frac{\Delta d}{S_0}$ where S_0 is the width of the outlet. Setting S_0 to be equal to the nozzle width of 1700 μm, the penetration efficiency of the particle trap impactor for outlet angle 45°, 90° and 135° is shown in Figure 13.

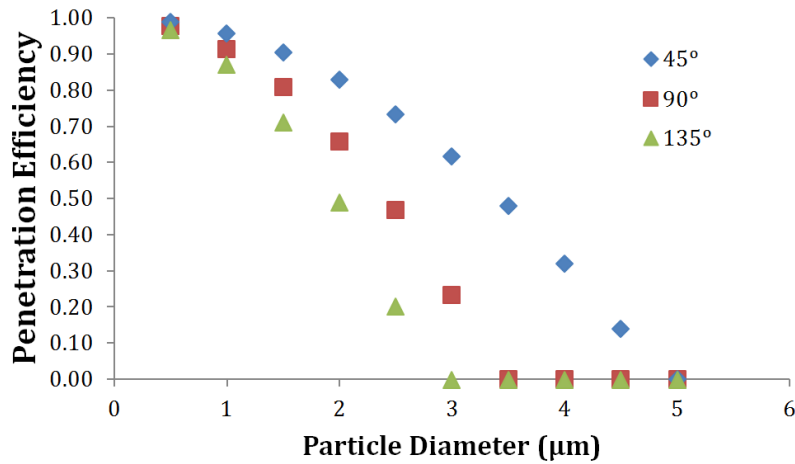


Figure 13 – Penetration efficiency based on analytical expression of particle radial displacement for outlet angle of 45°, 90° and 135°

This model assumes the particles are uniformly distributed along the channel with the same velocity. However, particles are typically faster in the center of the channel and slower near the walls due to the parabolic flow profile. Increasing the outlet angle shifts the penetration efficiency towards smaller diameters as expected since the radial displacement of the particle increases allowing smaller particles to be impacted.

2.2.6 COMSOL Simulation

2.2.6.1 Initial Parameter Selection

With a known design flow rate of 0.5 L/min, the critical dimensions for the design of the particle trapping impactor are the nozzle width W_0 , the outlet width which is also the distance to impactor S_0 , the impactor entrance width W_i and the impactor length L . The channel height h_0 and nozzle width W_0 are set to be 200 µm and 1700 µm respectively from the Stokes and Reynolds number design requirement. Because increasing the outlet angle does not significantly improve the slope of the penetration efficiency curve (Figure 13), 90° is used for practicality so the device can easily interface with other components. Based on the particle relaxation time

calculations, the nozzle length L is set to 4 times the nozzle width such that the particles will have the sufficient length to accelerate to the flow velocity at the nozzle. A tapered outlet to expand the flow is included in the simulations to allow a more continuous flow deceleration when integrated with the rest of the test system. The penetration efficiency of the impactor is simulated in COMSOL (4.3b) with these initial parameters for validation. The distance to the impactor S_o and the entrance width W_i are optimized through an iterative process by comparing the slope of the penetration efficiency curve for different values of S_o and W_i . The angle of the inertial focusing inlet ϕ_{acc} and the inlet reduction ratio are also optimized using simulation by evaluating the particle position and particle loss after the channel constriction.

2.2.6.2 Flow Simulation Setup

The Laminar Flow module is first used in COMSOL to simulate the flow of air within the channel. The channel geometry is generated with the dimensions of the channel defined as variables so they can be easily modified parametrically. Air in the material library provided by software is selected as the fluid material. The steady state velocity field within the channel is solved by defining a constant velocity at the inlet and a constant pressure at the outlet with a no-slip channel wall boundary condition. A constant velocity is used instead of a constant flow rate at the inlet as it improves solution convergence. Extra length is added to the inlet channel to ensure the flow is fully developed by the actual entrance of the inlet (Figure 14).

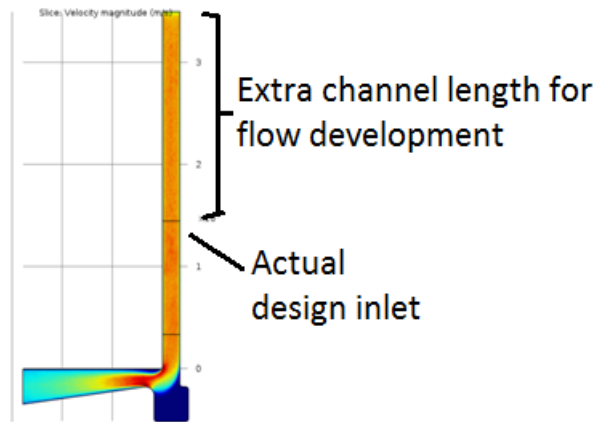


Figure 14 – Sample simulated flow velocity profile, tapered outlet

2.2.6.3 Particle Simulation Setup

The Particle Tracing module is set with initial conditions from the velocity field solution of the Laminar flow module. As a particle travels through the channel, it will see the solved flow velocity at its instantaneous position. The particles are released closer to the nozzle, away from the inlet of the laminar flow simulation to ensure the initial particle velocity is the developed flow velocity. The particles are randomly distributed at the design inlet using the *Density* setting in COMSOL in order to improve the accuracy of the results. The results are less dependent of the number of particles released compared to other settings such as *Uniform grid* or *Mesh*. 500 particles are released to provide sufficient coverage over the cross sectional area of the channel while minimizing computation time. Further increasing the particle number does not change the simulation results. The density of the particle is set to 1000 kg/m^3 such that the simulation results represent the aerodynamic diameter of the particle. For simplicity, the only two forces acting on the particles are drag force and inertial force. The effect of gravity, particle diffusion and any electrostatic surface effects with the channel walls are neglected. The wall conditions can be set to three options: *bounce*, *freeze* and *probability*. All the particles either bounce off or stick to the channel wall for the *bounce* and the *freeze* setting, respectively. The user can also define a

probability at which the particles will stick or bounce off the wall with the *probability* setting. Simulations are repeated for all 3 cases as the actual wall behaviour is not fully understood. The number of particles transmitted to the outlet is computed with the *transmission probability* setting in the software for a parametric sweep of the particle diameter from 0.5 to 4.5 μm .

2.2.6.4 Inertial Focusing Inlet

The effect of a channel reduction inlet on the penetration efficiency curve is investigated. The inlet is placed before the impactor to focus the particles towards the center of the channel. The theory of operation is similar to the impactor at which the inertial force acting on the particle when the flow constricts from inlet width W_{inlet} causes the particle to cross the streamline and travel towards the center of the channel as shown in Figure 15.

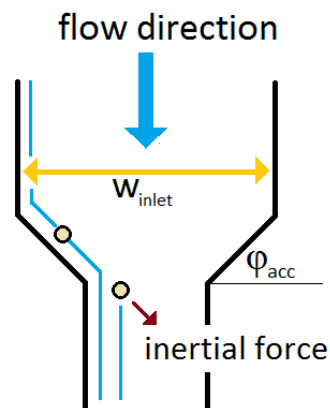


Figure 15 - Schematic of the inertial focusing inlet

By driving the particles closer to the center of the channel where the flow velocity is highest, the velocity of the particles increases and becomes less dependent the particle's starting streamline location. This improves the performance of the device as shown in the penetration efficiency curves example in Figure 16. The cutoff diameter is always higher for the *bounce* setting compared to *freeze* as the impacted particles have a chance of reentering the flow streamlines to

exit through the outlet. The effects of the wall conditions settings will be described in detail later in the section. By including the acceleration inlet, the slope of the bounce wall condition curve increases significantly. The penetration efficiency and the 50% cut-off diameter shifts left towards a smaller size when the acceleration inlet is included indicating more effective impaction at the same flow rate. Consequently, the acceleration inlet is included in all the simulations to better represent an optimized impactor.

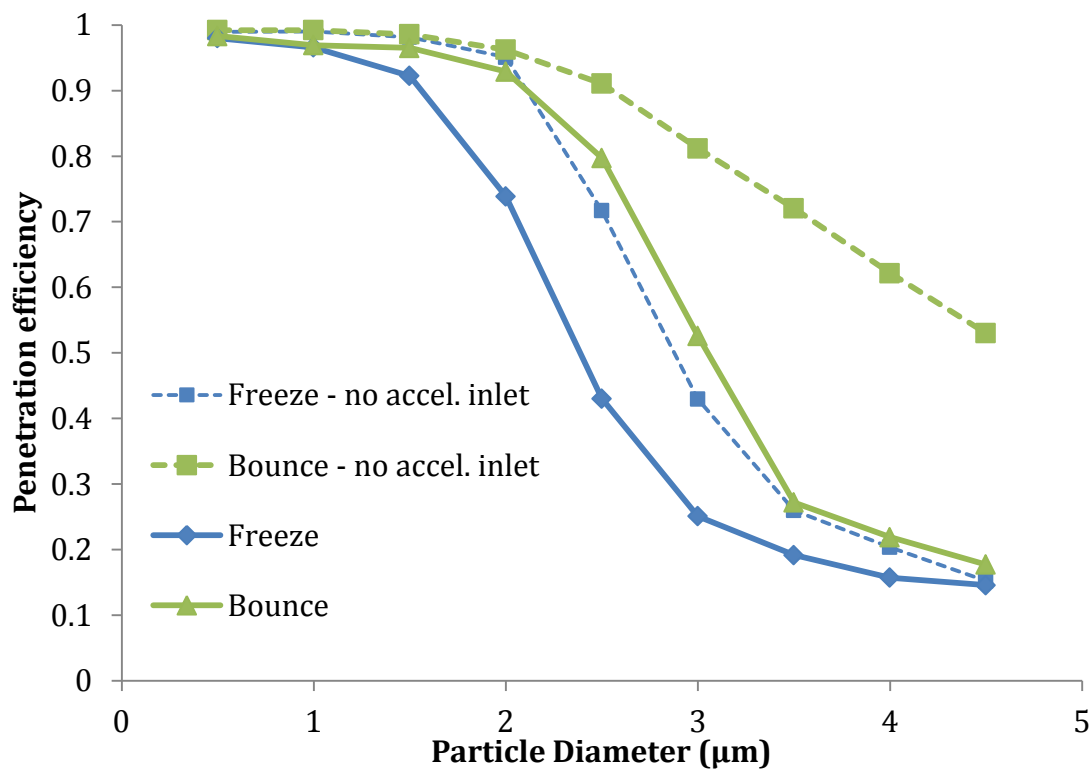


Figure 16- Penetration efficiency for sample device

Various acceleration angles ϕ_{acc} (Figure 15) are simulated to determine the best design based on particle loss and standard deviation of particle position. The effects of sharp and round corners with radius equal to the nozzle width (Figure 17) were also compared. Figure 18 shows the standard deviation of particle position from the center of the channel for different particle sizes. Increasing the angle increases the inertial focusing effects. However, particles near the side

walls are impacted into the inlet wall if the angle is too large; the percentage of particle transmitted decreases as the angle increases (Figure 19). This is caused by a region of low flow velocity at the corners of the focusing inlet as seen in Figure 20. Unless the channel shape matches the curve of the flow profile, a rounded corner only introduces a larger low velocity region, resulting in more particles to be impacted at the corner. A 45 degrees inlet angle is chosen to provide good focusing and acceptable particle loss for particles less than 2.5 μm particles. The same trade-off occurs for the inlet width W_{inlet} . Larger inlet width provides better focusing at the expense of higher particle loss by impaction near the channel walls. The channel width reduction is set at 4 to 1.

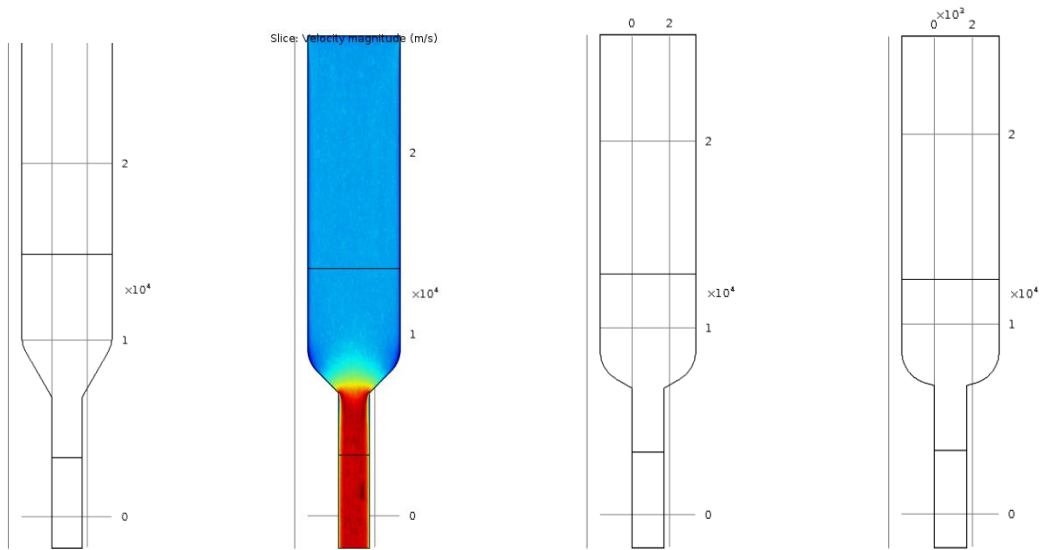


Figure 17 - Acceleration inlet with round corners- 30, 45, 60, 75 degrees (Left to right)

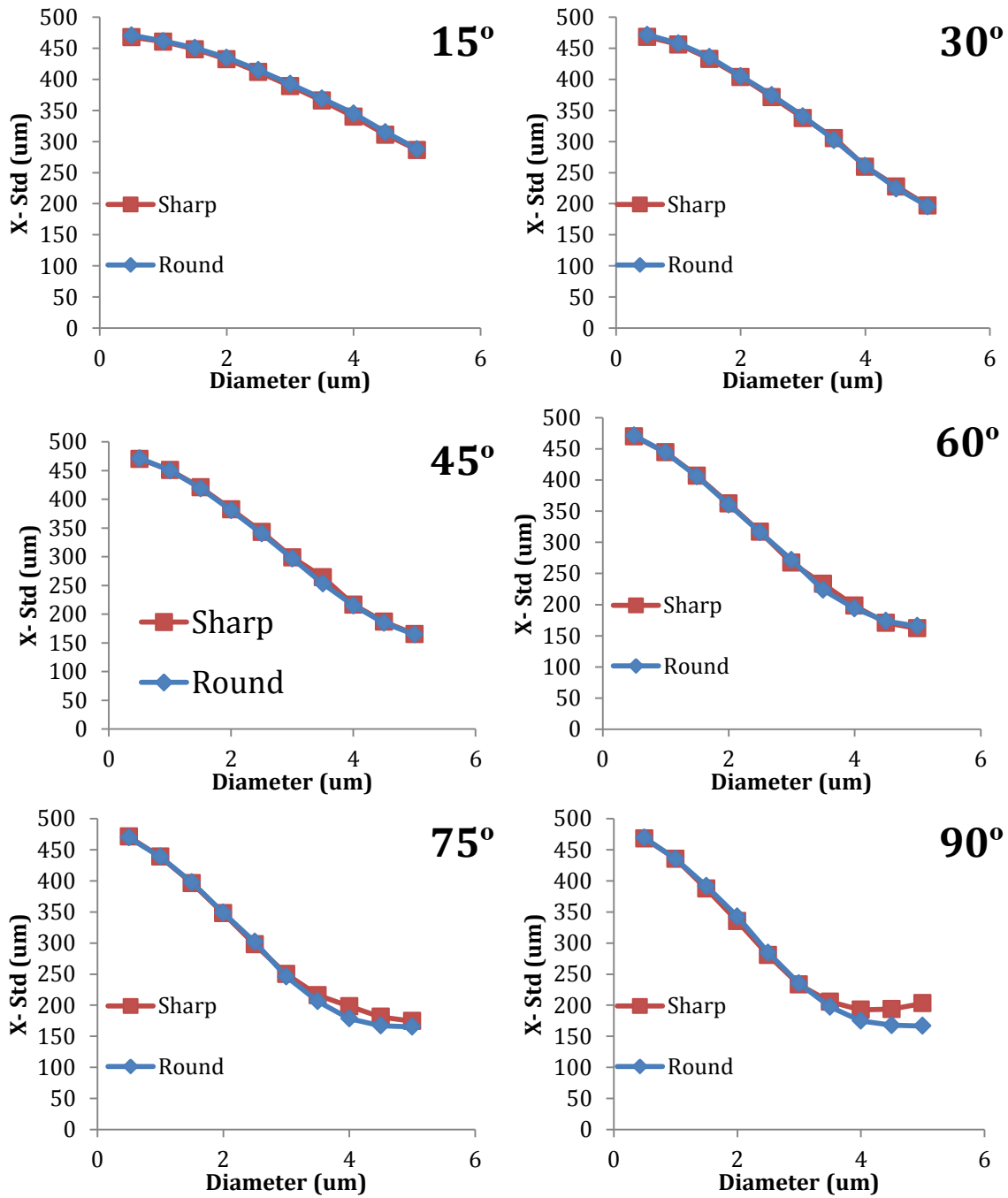


Figure 18 – X position standard deviation for inlet focusing angles 15 °, 30°, 45 °, 60°, 75 ° and 90 °

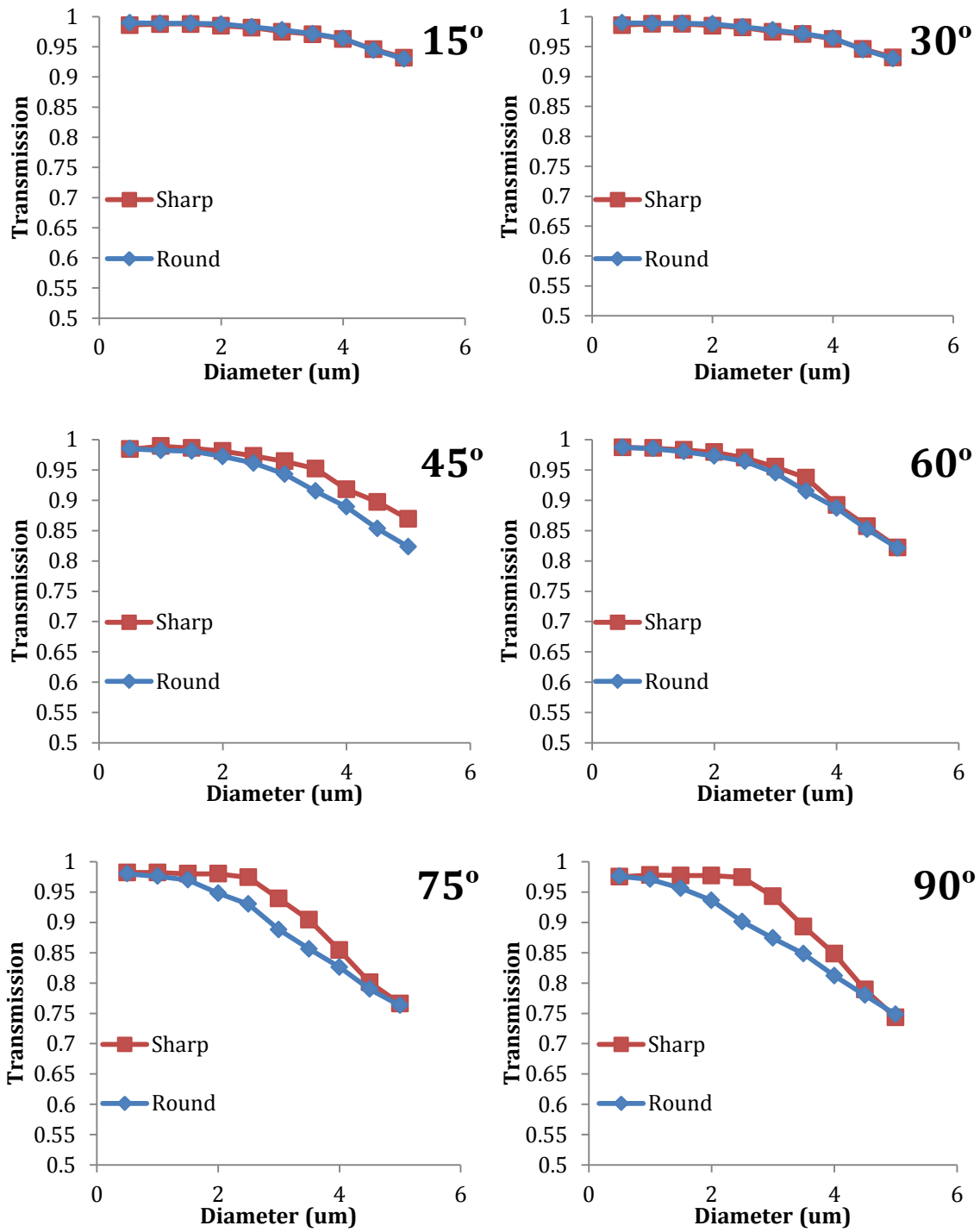


Figure 19 – Transmission probability for inlet focusing angles 15 °, 30°, 45 °,60 °, 75 ° and 90 °

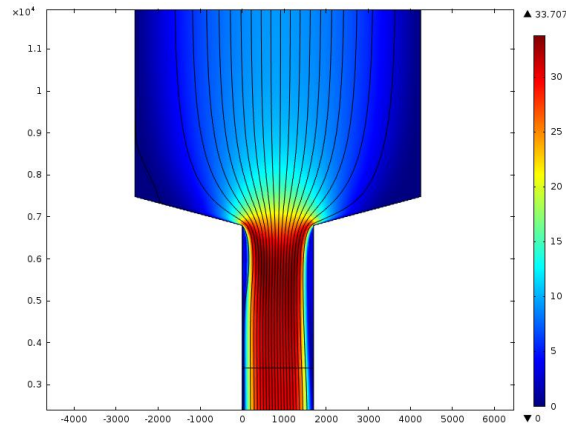


Figure 20 - Flow velocity profile of 75 degree inlet

2.2.1 2D vs 3D Simulation Comparison

The simulations were initially conducted in 2D to minimize computation time, allowing for a more thorough parametric sweep of the design variables. However, discrepancies are found in the flow profile and the transmission curve when the 2D simulations are compared with 3D simulations. The viscosity of the fluid appears to be lower in 2D, likely caused by the lack of viscous effects along the height of the channel. As shown in Figure 21, all the flow streamlines are compressed towards one side of the channel in the 2D simulation which is physically unfeasible. 2D simulation also does not account for the slower particles released near the top and bottom wall, resulting in a steeper penetration efficiency curve as shown in Figure 22. All the simulations to design the impactor geometry were done in 3D as a result.

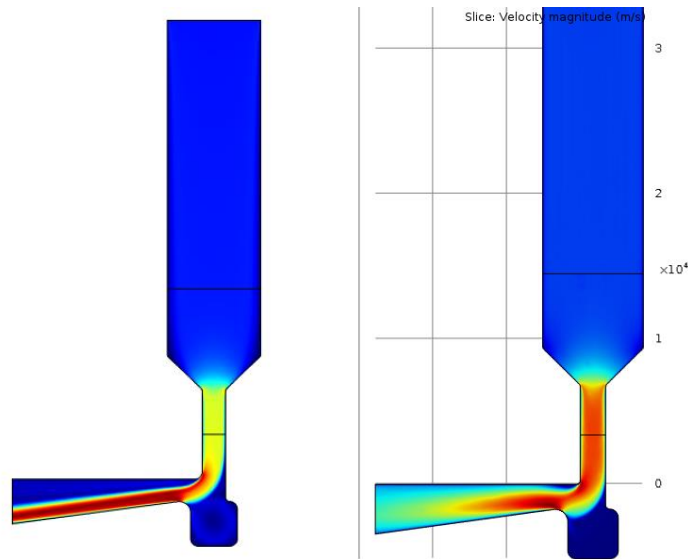


Figure 21 - Flow velocity profile of the device : 2D (Left) , 3D (Right)

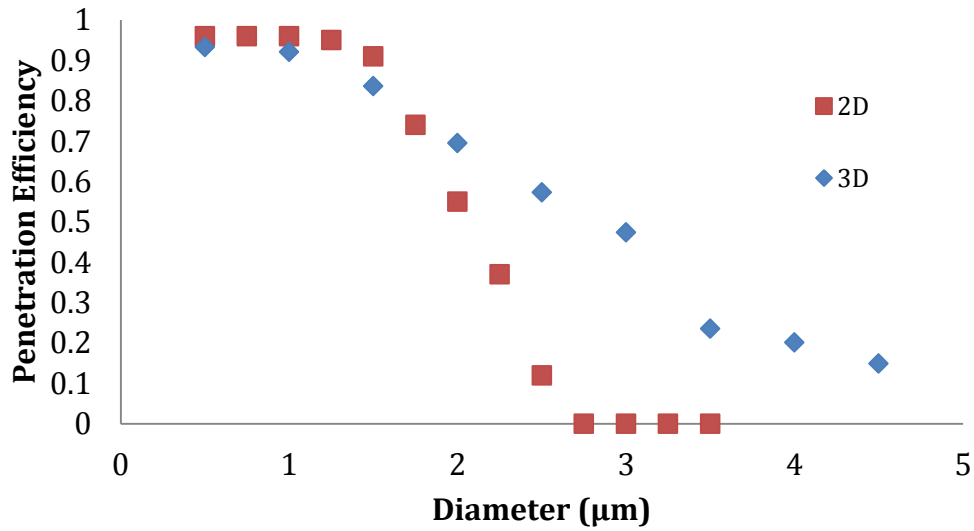


Figure 22 - Transmission ratio of impactor: 2D vs 3D

2.2.1.1 Distance to Impactor S_0

The penetration efficiency of the impactor for three values of the distance to impactor value S_0 expressed as ratios to the nozzle width W_0 are compared. All of the other geometric parameter values within the models are identical with the impactor width set to equal $2 W_0$.

Figure 23 is the velocity field of the three simulations.

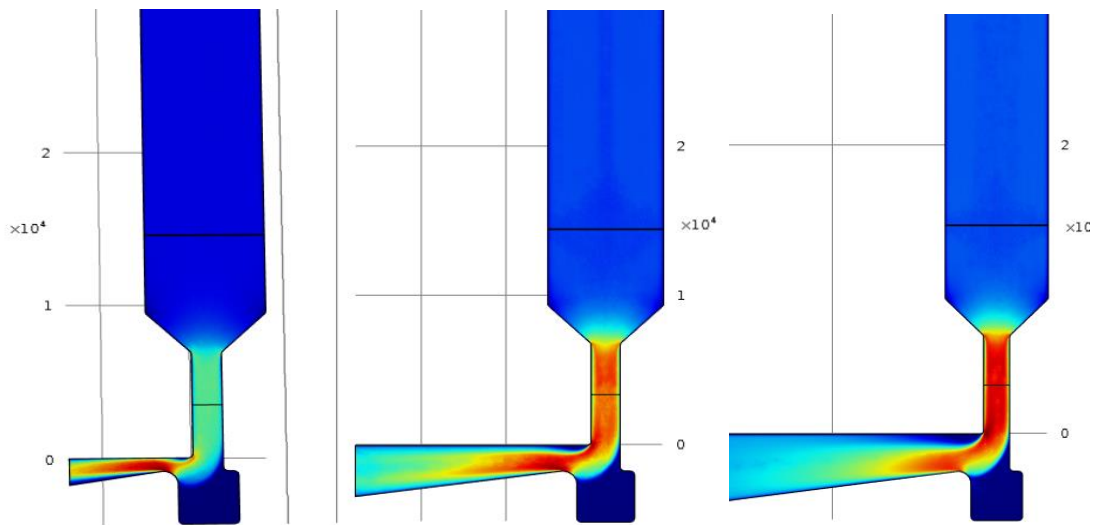


Figure 23 - Flow velocity field for Distance to Impactor $S_0 = 0.5 W_0, W_0$ and $1.5 W_0$. (Left to right) (Not to same colour scale)

For $S_0 = 0.5 W_0$, the slope of the penetration curve is very sensitive to the wall characteristics as shown in Figure 24. The slope is sharpest for the freeze wall condition indicating that a high percentage of particles colliding with the side wall of the particle trapping region. The 50% cut-off diameter increases for increasing percentage of particle bounce. This holds true for all sizes of S_0 as shown Figure 25 and Figure 26.

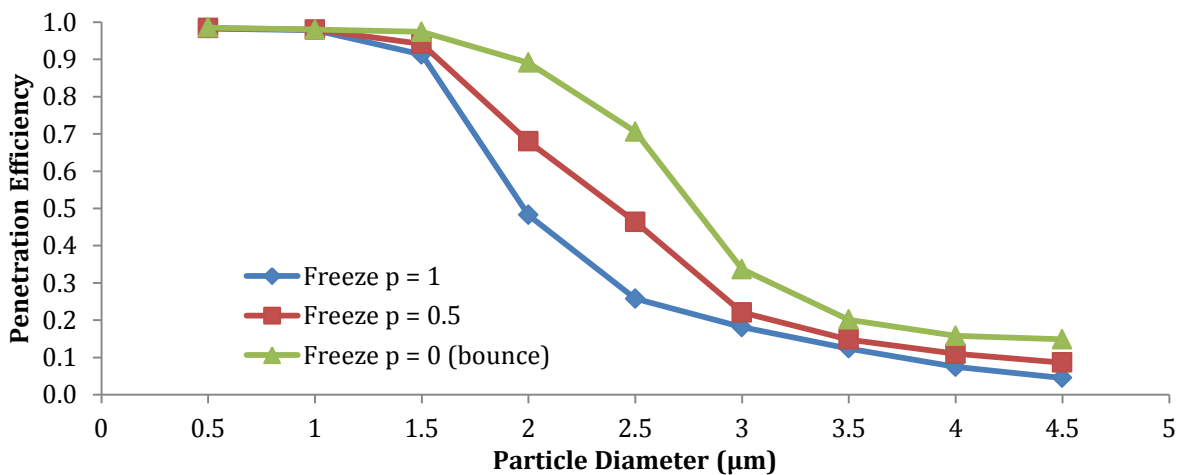


Figure 24 – Penetration efficiency for $S_0 = 0.5 W_0$ for freeze, 50% freeze and bounce wall condition

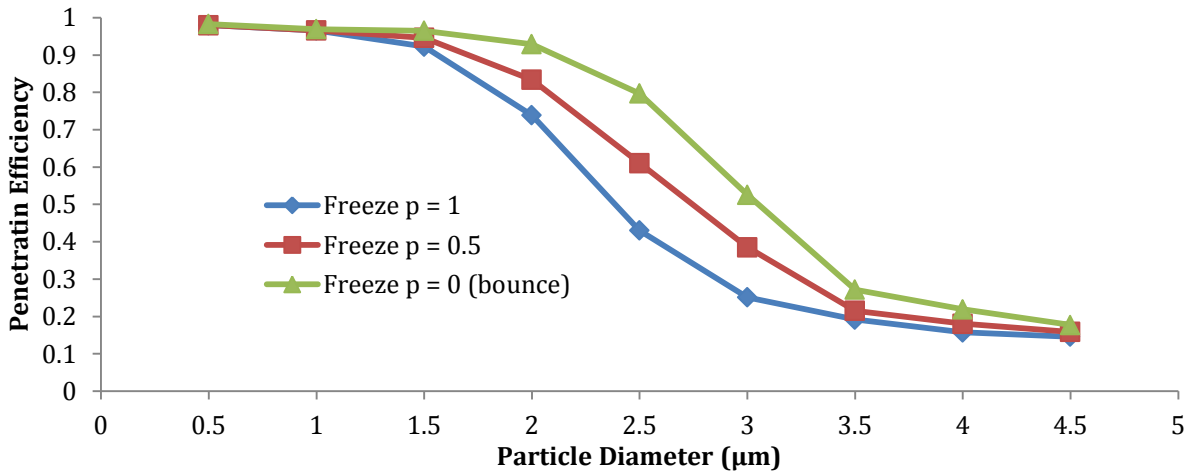


Figure 25- Penetration efficiency for $S_0 = W_0$ for freeze, 50% freeze and bounce wall condition

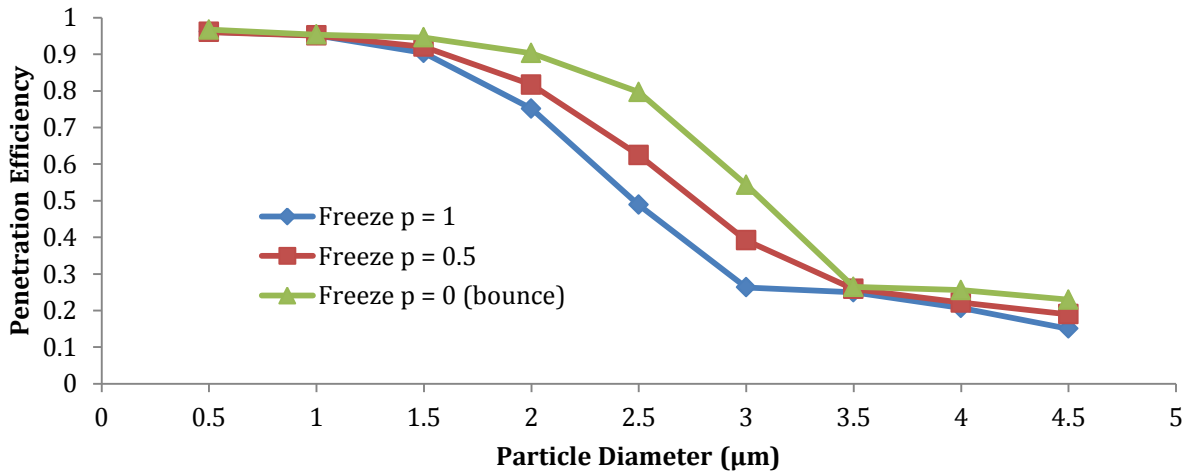


Figure 26 - Penetration efficiency for $S_0 = 1.5 W_0$ for freeze, 50% freeze and bounce wall condition

When the bounce condition is used, there is a chance for the particles to re-enter the sampling flow for particles impacting the wall. This is limited to particles impacting near the impactor entrance and bounce into the sample flow. Other impacted particles are carried into the particle trapping region by a low velocity flow recirculation shown by the flow streamlines in Figure 27. This has a tendency to transport the particles towards the opening of the impactor (Figure 27 right). However, the flow velocity within the trapping region is not high enough to reaccelerate the large particles back into the sample flow.

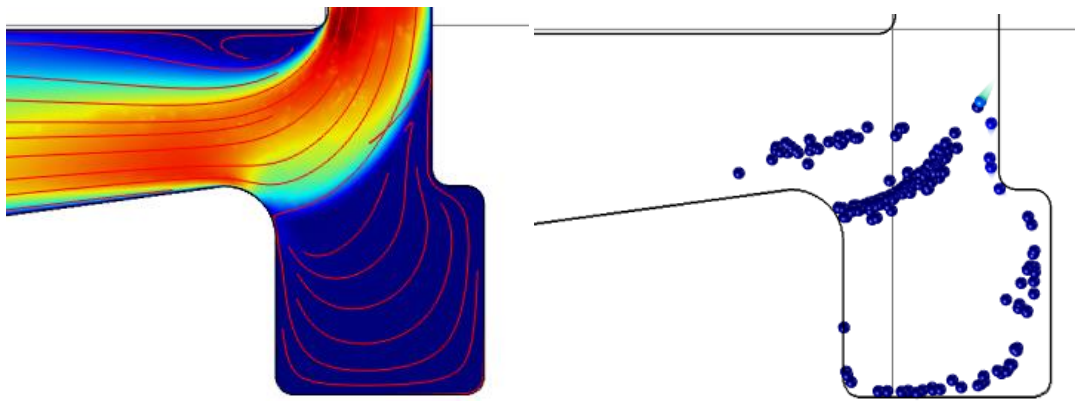


Figure 27 – Flow velocity field, streamline (left) and position of deposited particles for bounce wall condition (right) in the particle trapping region.

Increasing S_0 effectively increases the allowable stopping distance for the particles so the 50% cut-off diameter increases for larger S_0 . The 50% cut-off diameter and the slope are presented in Table 3. Δd_{p50} and ΔSlope are the calculated difference between the maximum and minimum 50% cut-off and slope for 3 wall settings. The slope of the penetration efficiency curve is calculated between 30% to 70% transmission. A higher absolute value of the slope represents a more effective impactor with a sharper cutoff. The slopes of the penetration curve for $S_0 = W_0$ and $S_0 = 1.5 W_0$ are very similar. Since the 30% and 70% transmission value are extrapolated, minor variation in the slope could be caused by random error in the calculation.

Table 3 - 50% cut-off diameter and slope of S_0 simulation results.

3D Model $W_i = 2 W_0$									
	$S_0 = 0.5$			$S_0 = 1$			$S_0 = 1.5$		
	Freeze	p = 0.5	Bounce	Freeze	p = 0.5	Bounce	Freeze	p = 0.5	Bounce
d_{p50} [μm]	1.98	2.42	2.78	2.39	2.75	3.05	2.48	2.77	3.08
Δd_{p50} [μm]	0.8			0.66			0.6		
Slope [$1/\mu\text{m}$]	-0.61	-0.46	-0.64	-0.50	-0.42	-0.52	-0.49	-0.38	-0.54
ΔSlope [$1/\mu\text{m}$]	0.18			0.1			0.15		

2.2.1.2 Impactor Width W_i

The simulation is repeated for impactor width W_i equal to nozzle width W_0 , $1.5 W_0$ and $2 W_0$ (refer to APPENDIX A – Impactor Width W_i Simulation Data for example). The penetration efficiency curve is very sensitive to the wall conditions for a small impactor width. This is similar to the results with a small distance to impactor S_0 for which the particles collide with the channel walls. The 50% cut-off diameter decreases for larger values of impactor width. Because the particles along the same streamline position experience the same magnitude of radial displacement, a larger impactor width allows more particles to enter the particle trapping region. The penetration efficiency curves are also least dependent on wall conditions for impactor width W_i . However, the 50% cut-off diameter is smaller than $2.5 \mu\text{m}$ for the case of $W_i = 2W_0$. Table 4 provides a summary of the impactor width simulation results.

Table 4 -50% cut-off diameter and slope of W_n simulation results.

3D Model $S_0 = W_0$									
	$W_i = W_0$			$W_i = 1.5 W_0$			$W_i = 2 W_0$		
	Freeze	$p = 0.5$	Bounce	Freeze	$p = 0.5$	Bounce	Freeze	$p = 0.5$	Bounce
$d_{p50} [\mu\text{m}]$	2.02	2.44	2.94	2.39	2.75	3.05	2.08	2.28	2.47
$\Delta d_{p50} [\mu\text{m}]$	0.92			0.66			0.39		
Slope [$1/\mu\text{m}$]	-0.54	-0.37	-0.46	-0.50	-0.42	-0.52	-0.57	-0.46	-0.54
Δ Slope [$1/\mu\text{m}$]	0.17			0.10			0.078		

2.2.1.3 Parameter Selection

From the simulation results, the performance of the impactor is observed to be somewhat insensitive to the geometry of the impactor. Changing the geometry has a minor effect on the sharpness of the slope of the penetration efficiency curve and only shifts the cut-off diameters of the curve. As long as the flow rate is within practical ranges, the exact 50% cut-off diameter can be tuned by adjusting the flow rate. Having an acceleration inlet in all the simulations partly reduced the device performance sensitivity to the geometry. By focusing the particles to the

highest velocity streamlines in the center of the channel, the difference in impaction characteristics is less distinct. However, some designs are more dependent on the wall conditions. Small features should be avoided, i.e. $S_0 = 0.5W_0$ and $W_i = W_0$ because the penetration efficiency is very sensitive to the wall condition. The impactor width is also limited by the flow rate. If the impactor width is larger ($W_i = 2W_0$), a lower flow rate is required to achieve the same 50% cut-off diameter which may not produce sufficient counts. The distance to impactor S_0 and impactor width W_i are set to W_0 and $1.5 W_0$, respectively, for the fabricated device. Table 5 is a summary of the impactor geometry and the design process.

Table 5 –Summary of impactor geometry design

Parameter	Value	Design process
Flow rate Q	0.5 L/min	Stochastic model
Channel height h_0	200 μm	Stokes and Reynolds number
Nozzle width W_0	1700 μm	Stokes and Reynolds number
Nozzle length L	4x W_0	Stopping distance
Outlet angle ϕ_{out}	90°	Radial displacement
Acceleration inlet angle ϕ_{acc}	45°	COMSOL simulation
Inlet reduction ratio	4 to 1	COMSOL simulation
Distance to Impactor S_0	W_0	COMSOL Simulation
Impactor width W_i	1.5 W_0	COMSOL Simulation

3 Design of Detection System

3.1 Particle Detection

Light scattering is commonly used in commercial instruments to detect particles. For the design of a miniaturized detection system, the light scattering intensity and the expected optical power from the scattered light of particles are calculated. Based on the results, the geometry of the detection system is determined. The optical components for the detector are selected and the expected signal from the signal conditioning circuit is evaluated.

3.1.1 Light Scattering Theory

The light scattering intensity from a particle is highly dependent on the size parameter $\alpha_p = \frac{\pi d_p}{\lambda}$ which is a scaled ratio of the particle diameter to the wavelength of incident light in the medium λ . For the simplest case in which the particles are small compared to the wavelength ($\alpha_p \ll 1$), the electromagnetic wave in the particle can be assumed to be uniform. The light scattering intensity I is isotropic as a result and can be described by an exact analytical expression from the Rayleigh scattering theory

$$I = \frac{k^4 r_p^6}{d^2} \left| \frac{m^2 - 1}{m^2 + 2} \right|^2 I_o \quad (21)$$

where $k = \frac{2\pi}{\lambda}$ is the wave number, $r_p = \frac{d_p}{2}$ is the radius of the particle, d is the distance from the particle, $m = \frac{n_{particle}}{n_{medium}}$ is the relative index of refraction of the particle and I_o is the incident light intensity. The blue colour of the sky is attributed to Rayleigh scattering since the intensity is inversely proportional to the 4th power of the incident light wavelength.

When the particle size is greater than the wavelength of incident light ($\alpha_p \gg 1$), the particles diffract, refract or reflect light depending on the location of the electromagnetic wave

within the particles. The intensity is strongly angular dependent for this type of scattering and is a superposition of all the contributing scattering modes. The direction of the scattering angle θ is defined in Figure 28.

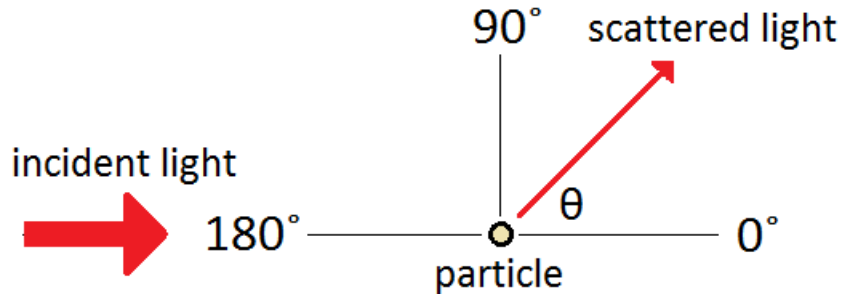


Figure 28 - Light scattering angle θ

Determining the scattering intensity from a particle requires solving the Maxwell's equation for an electromagnetic wave from air through a dielectric medium of different refractive index. For simplicity, the particles are often assumed to be spherical such that the scattering intensity is axisymmetrical. This type of scattering is referred to MIE scattering, named after Gustav Mie who developed an analytical solution for this problem based on infinite series. The solution has been adapted into computation code, notably by Bohren and Huffman [71], to calculate the scattering intensity. In simplified form, the scattering intensity is given by

$$I(\theta) = \frac{I_o S_n(\theta)^2}{k^2 d^2} \quad (22)$$

where $S_n(\theta)$ is the amplitude scattering function [53]. The amplitude scattering function $S_n(\theta)$ describes the angular dependent characteristic of the MIE scattering intensity and is a function of particle size, incident light wavelength and refractive indices of medium and particle.

The MIEPlot software (v4.3, Philip Laven) is used to compute the amplitude scattering function $S_n(\theta)$ to evaluate the optimal design of the optical system. The effects of scattering angle, particle size, and incident light wavelength are also examined.

3.1.2 Amplitude Scattering Function

The refractive index of air and polystyrene are used for the medium and the particles for the amplitude scattering function $S_n(\theta)$ calculations. The refractive index of polystyrene ($n=1.5$) also closely resembles the refractive index of dust ($n = 1.525$) [72]. Polystyrene test particles will also be used for the experiments.

Following conventions in light scattering publications, the square of the amplitude scattering function $S_n(\theta)^2$ is computed to express the scattering angle dependent term in equation 22. Figure 29 is the amplitude scattering function shown in log scale of $2.5 \mu\text{m}$ diameter particles with red laser light $\lambda = 650 \text{ nm}$ for three polarizations. The ripples represent the interference of light due to diffraction. The intensity is highest in the forward direction and drops significant after 15° degrees. The polarization shifts the local minimum and maximum points of the intensity ripple but does not have a significant influence on the overall intensity. In the forward scattering region, the intensity is independent of polarization.

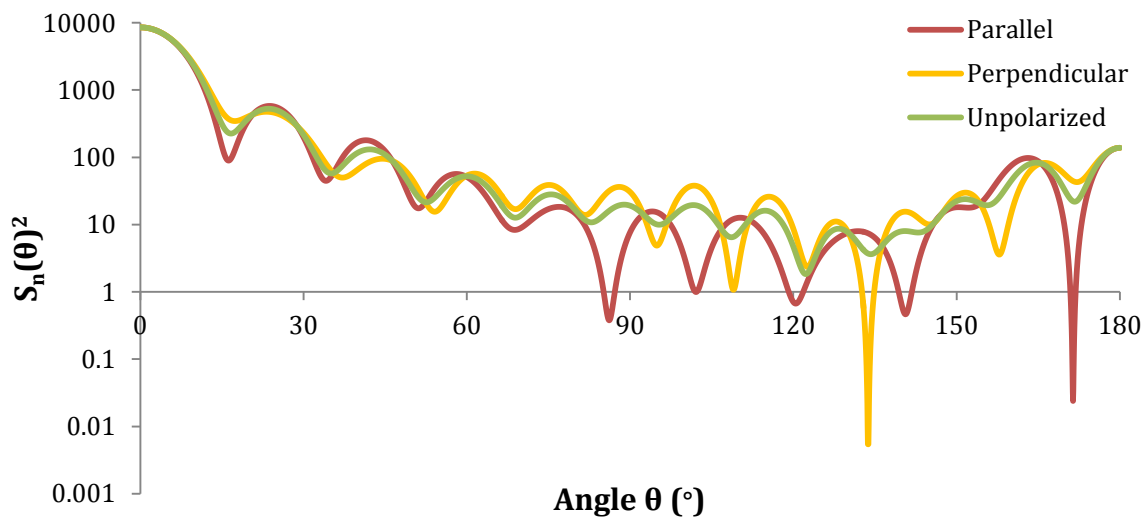


Figure 29 – Amplitude scattering function $[S_n(\theta)]^2$ for $2.5 \mu\text{m}$ diameter particles , $n_{\text{medium}} = 1.00027$, $n_{\text{particle}} = 1.5$, $\lambda = 650 \text{ nm}$.

The diffraction effect is reduced for 1 μm particles as shown in Figure 30. However, the intensity is still highest in the forward direction. The overall intensity drops significantly as the particle size decreases to 0.5 μm (Figure 31).

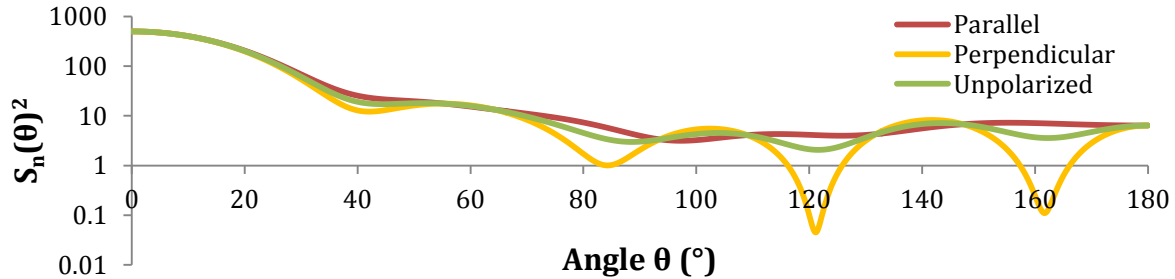


Figure 30 - Amplitude scattering function $[S_n(\theta)]^2$ for 1 μm diameter particles, $n_{\text{medium}} = 1.00027$, $n_{\text{particle}} = 1.5$, $\lambda = 650 \text{ nm}$.

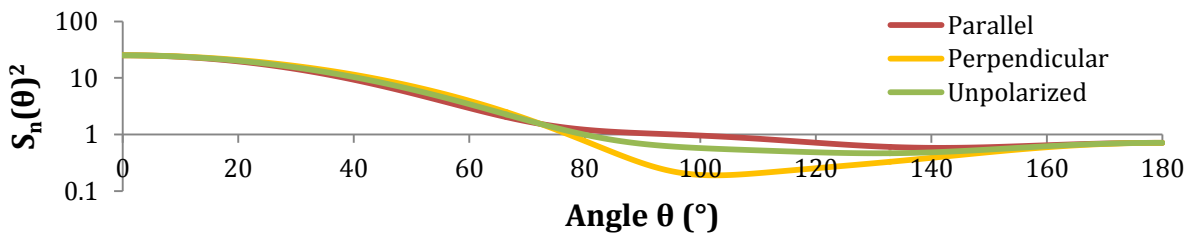


Figure 31 - Amplitude scattering function $[S_n(\theta)]^2$ for 0.5 μm diameter particles, $n_{\text{medium}} = 1.00027$, $n_{\text{particle}} = 1.5$, $\lambda = 650 \text{ nm}$.

The amplitude scattering function of particle of size 1.5 μm for wavelengths of common laser light sources is shown in Figure 32. Changing the wavelength of the incident light only affects the diffraction region of scattering. The intensity is almost 10 times larger in the first 20° for 450 nm blue laser light compared to 650 nm red light.

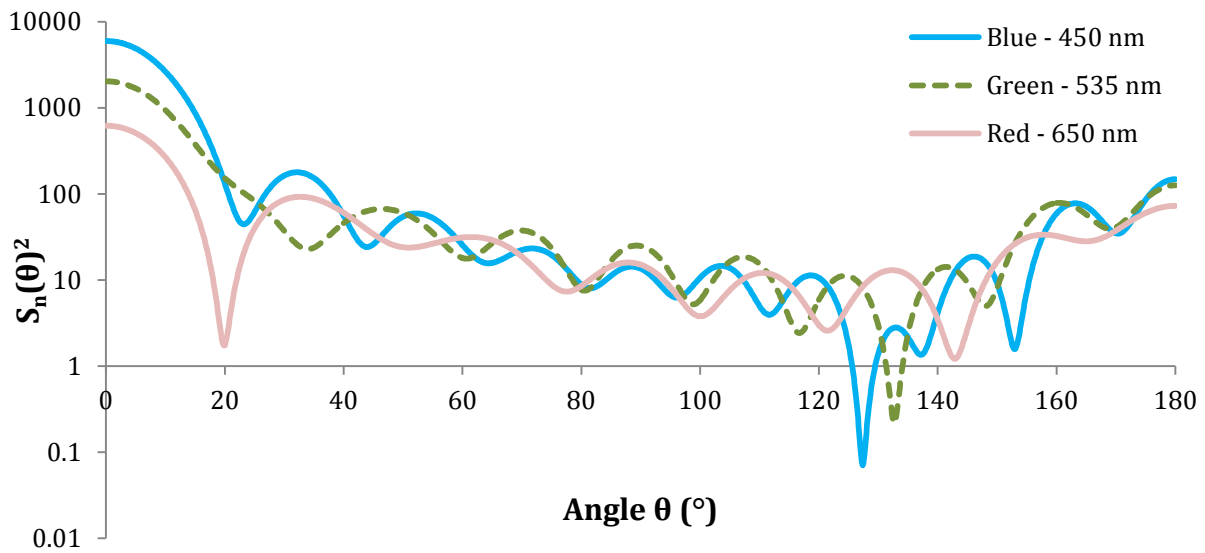


Figure 32 - Amplitude scattering function $[S_n(\theta)]^2$ for 1.5 μm diameter particles - Red, green and blue incident light source

3.1.3 Optical System Design

3.1.3.1 Flow Channel Dimension

The particles are transported to the sensing region of the detector from the outlet of the impactor. The first step in designing the optical detector is defining the dimensions of the flow channel and the sensing region. The overall size of the optical system should be in the same order of magnitude as the microchannel. Having a small flow channel allows a better interface with the microchannel of the impactor. Confining the particles to a small region is also advantageous for detection because the sensing system can be constrained within a small, target region. However, a smaller flow channel results in a higher particle velocity so the particles spend less time in the sensing region. This imposes two design requirements on the hardware of the system; the maximum sampling rate of the digital data acquisition system must be fast enough to capture the light pulse of the passing particle, and the noise-equivalent power of the detector must be low enough such that the short light pulse from the particle produces a

sufficient signal to noise ratio. Assuming the detector will register a signal when the particle is in the sensing region, the expected time of particle in the sensing region can be computed by the sensing region length l_s (Figure 33) divided by the particle velocity V_p .

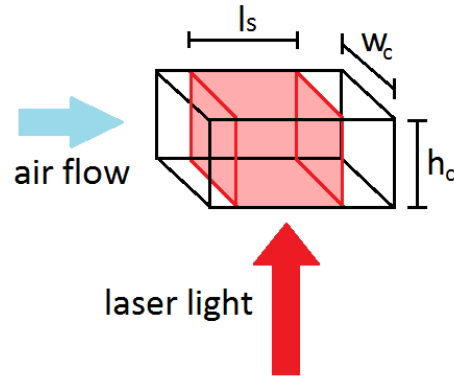


Figure 33 – Sensing region within the flow channel

Table 6 shows the calculated pulse width of the a particle for a channel height $h_c = 0.5$ mm, a sensing length $l_s = 1$ mm and a flow rate $Q = 0.5$ L/min. Because the optical intensity from the laser light can vary along the channel height h_c depending on laser beam divergence or focusing characteristics, the channel height h_c should be minimized to ensure the particles are in the same plane and reduce the signal dependency on the vertical position of the particles. The sensing length l_s of 1 mm is used as a minimum case for the size of commercial available optical components.

Table 6 - Signal pulse width of particles for varying channel widths with 0.5 L/min flow rate and 0.5 mm channel height h_c

Channel Width W_c (mm)	Time (ms)
0.5	0.03
1	0.06
2	0.12
3	0.18
4	0.24
5	0.3

For 0.5 mm channel width, the pulse width is found to be 0.03 ms. Assuming a parabolic profile of the flow, the pulse width could be half the calculated value from the average velocity, which is in a reasonable range for the sampling rate of data acquisition systems (DAQ) of around 5MHz [73]. To determine if the length of the signal is feasible for detection, the optical power of the scattered light is calculated and compared with the specifications of commercially available components.

3.1.3.2 Light Scattering Optical Power Calculation

The forward scattering and 90° scattering detection systems are most commonly used in commercial instruments. Forward scattering systems take advantage of the high intensity scattering in the forward angles due to diffraction (Figure 34). However, a light trap is required to be precisely aligned to prevent the laser source from directly illuminating the detector while capturing the scattering light. The total amount of detected scattered light is represented by the sum of the scattering light between start angle θ_0 and end angle θ_1 . Although the scattering intensity is lower for right angle scattering, a wide range of scattering angles can be captured with additional optical components (Figure 35). It is also relatively simple to set up. The optical power is calculated from both systems to evaluate the designs for a miniaturized detection system.

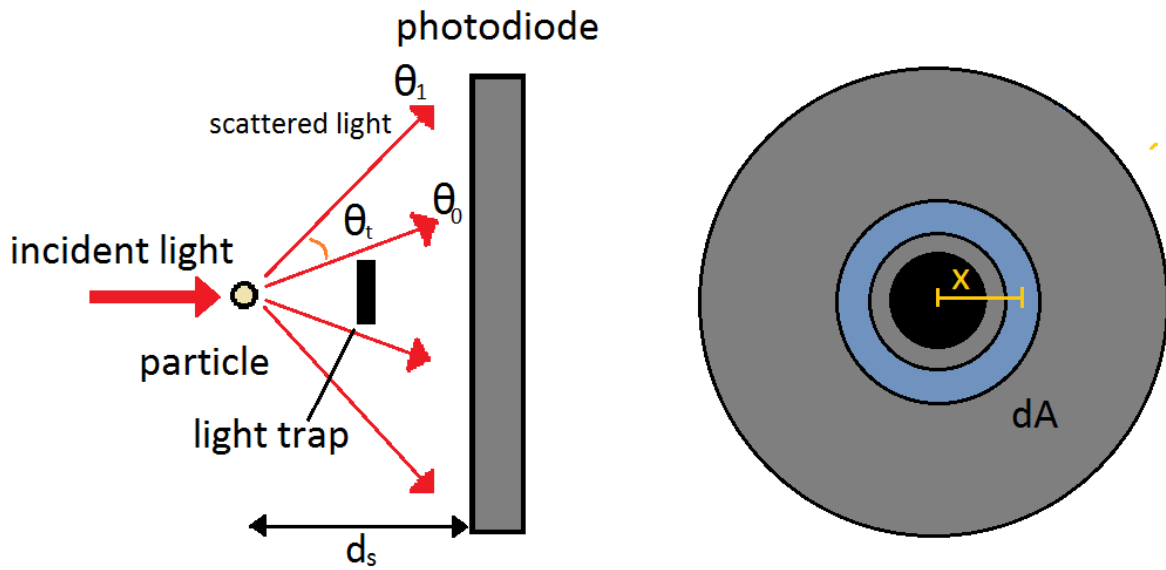


Figure 34 - Forward light scattering system, exaggerated light trap

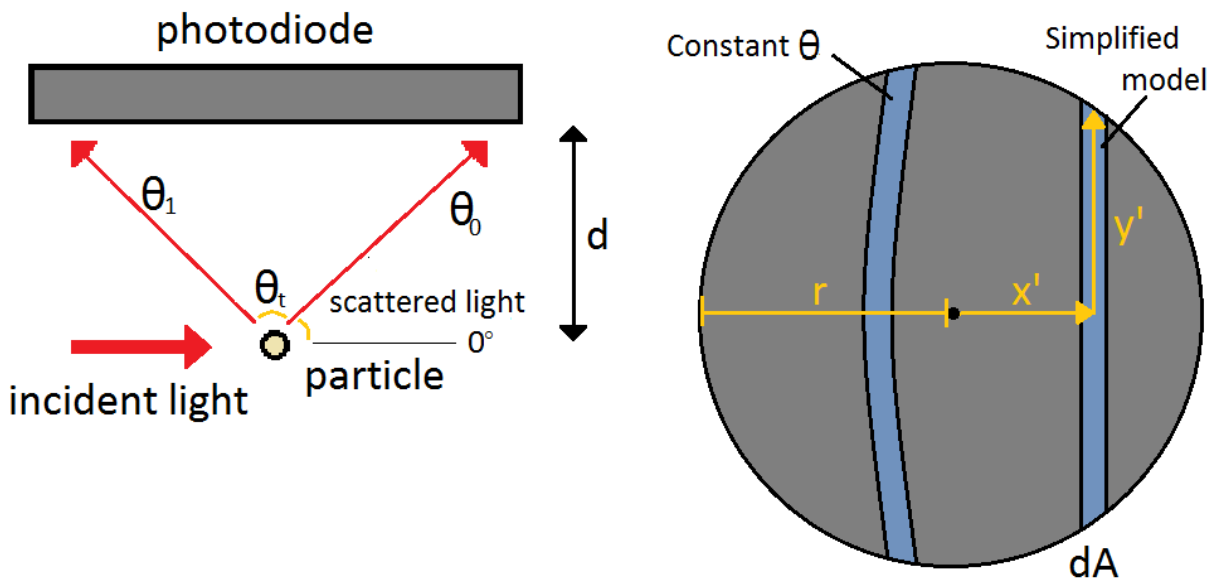


Figure 35 - 90° scattering system

Assuming a Gaussian shaped beam from the incident light source, the maximum optical power is likely when the particle is at the center of the channel. The optical power of the scattered light by the particle at this position is obtained by integrating the light scattering intensity from the particle over the exposed surface area of the detector given by

$$P = \int I(\theta, d_s) dA \quad (23)$$

where $I(\theta)$ is the scattering light intensity given by Mie scattering for the particular wavelength, the incident light source and the particle size and dA represents a infinitesimal area on the detector. The light scattering angle is constant over a parabolic path on the detector as shown in Figure 35. For simplicity, the light scattering angle is assumed to be similar at each horizontal distance x from the centre of the circular detector. As a result, dA is expressed as $dA = y(x) dx$ for a 90° scattering system. Typically the surface area of the detector is a circular shape which gives $y(x) = 2\sqrt{r_d^2 - x^2}$ and r_d is the radius of the detector. To further simplify the model, the distance from the detector d_s is also assumed to be constant so equation 23 becomes

$$P = \int 2\sqrt{r_d^2 - x^2} I(\theta) dx \quad (24)$$

Equation 24 can be further expressed as a function of scattering angle to numerically compute the integral. By trigonometry, the radius and the horizontal distance are given by:

$$r_d = d_s \tan\left(\frac{\theta_1 - \theta_0}{2}\right) \quad (25)$$

$$x = d_s \tan\left(\frac{\theta_1 + \theta_0}{2} - \theta\right) \quad (26)$$

where d_s is the distance between the particle and the detector. dx in equation 24 is given by differentiating equation 26,

$$dx = d_s \left(1 + \tan^2\left(\frac{\theta_1 + \theta_0}{2} - \theta\right)\right) d\theta. \quad (27)$$

The integral to calculate optical power becomes

$$P = \int_{\theta_0}^{\theta_1} 2d_s \sqrt{\tan^2\left(\frac{\theta_1 - \theta_0}{2}\right) - \tan^2\left(\frac{\theta_1 + \theta_0}{2} - \theta\right)} \left(d_s \left(1 + \tan^2\left(\frac{\theta_1 + \theta_0}{2} - \theta\right)\right) I(\theta)\right) d\theta \quad (28)$$

The same analysis can be applied for the forward scattering case. The integral is simplified by considering a circular strip of area $dA = 2\pi x dx$ where the scattering angle θ is the same at each value of x due to the axisymmetry of light scattering. The integral for the optical power becomes

$$P = \int 2\pi x I(\theta) dx. \quad (29)$$

Similarly, the x to θ transformation is given by:

$$x = d_s \tan(\theta) \quad (30)$$

$$dx = d_s(1 + \tan^2(\theta)) d\theta \quad (31)$$

The total power for the forward scattering system is defined as

$$P = \left(\int_{\theta_0}^{\theta_1} 2\pi d_s \tan(\theta) I(\theta) d_s(1 + \tan^2(\theta)) d\theta \right). \quad (32)$$

The integrals from equation 28 and 32 are calculated numerically in MATLAB (r2013b, Mathworks, Natick, MA, U.S.A.) using the trapezoidal rule. With known design parameters such as the distance from the detector d_s , the optical power of the incident light I_0 , the incident light wavelength λ and the optical intensity $I(\theta)$ obtained from MIEplot, the optical power for forward and 90° scattering systems can be calculated.

3.1.3.3 Component Selection

In order to design a low-cost, personal exposure monitor, the two most important factors in component selection are cost and size. Because the particles are inertially sized with the impactor, the detection system aims to provide a reliable count of PM 2.5 without the expensive optical components used in commercial particle counters to characterize the particles. A red laser diode light source is desired because they are compact in size and are readily available commercially. For the same reason, photodiodes are preferred over more sensitive but also more expensive options such as avalanche photodiodes and photomultipliers. A lens can be used to

focus on the path of the particle to achieve sufficient incident light optical power on the detector. While glass lenses are typically expensive, small, mass producible polymer lenses can be eventually used to reduce the cost. The optical system is designed through an iterative process with these considerations.

3.1.3.1 Optical Alignment

Using commercially available parts, the optical alignment of the components is simulated using the ray tracing software OSLO (Lambda Research, Littleton, MA, U.S.A.) to produce a feasible design. For the forward scattering system, the light from the laser diode is focused onto a light trap on a second lens as shown in Figure 36. The second lens directs the scattered light onto the photodiode. Designing such a system is relatively complex with many parameters to optimize. The distance between particle and the lens d_s is minimized to increase signal strength. However, a large portion of the light will be blocked by the light trap if d_s is too small. Consequently, the width of the light trap is minimized while ensuring all the direct light is captured from the laser diode. The sensing length l_s must also be minimized to increase optical power from focusing but sufficiently wide to produce a detectable signal width.

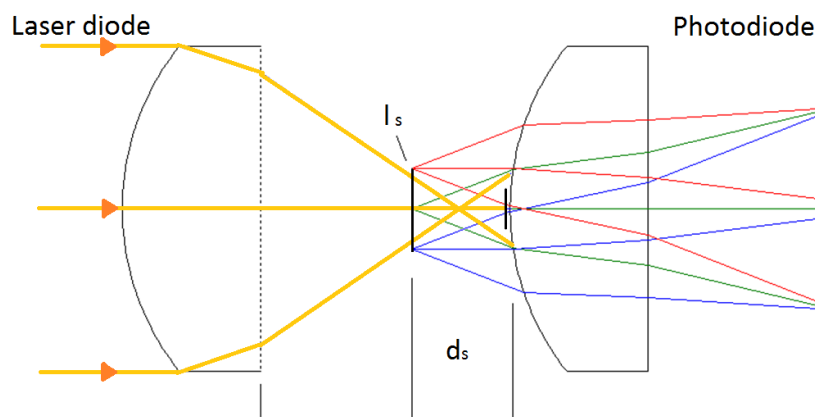


Figure 36 - OSLO ray tracing simulation for forward scattering

For 90° scattering, only 1 lens is required to focus the laser light. The alignment is much simpler with the photodiode placed as close to the sensing region as possible without seeing the direct light. The placements are restricted by the size of the components rather than the optics. A Solidwork model is designed to help determine the possible position of the components (Figure 37).

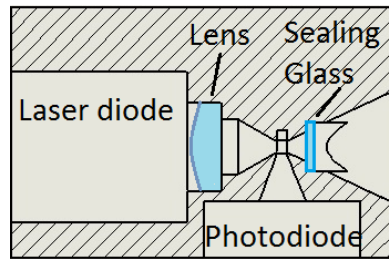


Figure 37 - Solidworks model of the 90° system

3.1.3.2 Optical Power Calculation

With the placement of the optical components determined for selected components, the optical power is calculated for both systems for 0.5 μm to 2.5 μm particle diameters. Table 7 gives a summary of the optical power calculation results. The forward scattering assumes a light trap diameter of 0.5 mm which limits the scattering angle from 2° to 13°.

Table 7- Optical power calculation for forward and 90° scattering

	Forward scattering	90° scattering
Detector Parameters		
Start Angle θ_0 (°)	2	76
End Angle θ_1 (°)	13	104
Wavelength λ (nm)	650	
Distance d_s (mm)	6.44	5.09
Sensing length l_s (mm)	1	0.75
Particle Diameter (μm)	Optical Power (W)	
0.5	1.05e-08	9.88e-10
1	1.16e-07	4.05e-09
1.5	1.63e-07	1.09e-08
2	7.91e-07	9.16e-09
2.5	4.17e-07	1.09e-08

For the selected components, the light scattering intensity is 10 to 80 times higher for forward scattering compared to 90° scattering. It is difficult to achieve the same order of magnitude of optical power even if an additional mirror is placed opposite of the detector to double the amount of captured light. For a 90° design to be feasible, the detector needs to capture a much wider angle than the calculated system. However, this is difficult to achieve due to the size restrictions of the components relative to the microchannel. Based on these calculation results, the forward scattering mode is selected for the detector.

3.1.3.1 Signal-to-Noise Ratio Calculation

To determine the required sensitivity of the photodetector, the order of magnitude of signal-to-noise ratio SNR of the system is estimated using the calculated pulse width and optical power. The pulse width is calculated to be between 0.03 to 0.05 ms for a sensing length l_s of 1 mm and a flow rate of 500 mL/min with channel dimensions of 0.5 mm by 0.5 mm and 0.5 mm by 1 mm respectively. The noise equivalent power NEP is typically specified for optical detectors as the minimum root mean square of power that will produce a signal-to noise ratio of 1 for a bandwidth of 1 Hz. The noise equivalent power for optical detectors is wavelength dependent and is measured in W/\sqrt{Hz} . Consequently, a higher power is required to produce the same signal to noise ratio at a higher bandwidth. The minimum required power for bandwidth B is expressed as $P_{min} = NEP * \sqrt{B}$. Using the sampling rate of a typical DAQ as the worst case bandwidth at 500 kHz, P_{min} for a photodiode with NEP of $8e-14 W/\sqrt{Hz}$ is calculated to be $5.66E-11 W$. Comparing P_{min} with the lowest optical power for 0.5 μm particle gives a SNR of approximately 190. The optical power from forward scattering should be detectable. The signal voltage depends on the amplification stages in the signal conditioning circuit design.

3.1.3.2 Signal Conditioning Circuit

The laser diode is driven by a simple, current-limiting resistor. The main focus of the circuitry design is on the amplification and the filtering of the photodetector signal. Typical optical sensors have a responsivity of 0.5 A/W. A gain of 200,000 is required to amplify the 0.1 nano-watts optical signal to the milliamp range. Figure 38 is the schematic of the signal conditioning circuit which consists of 3 major parts: the transimpedance amplifier, the high pass filter and a final amplifier stage.

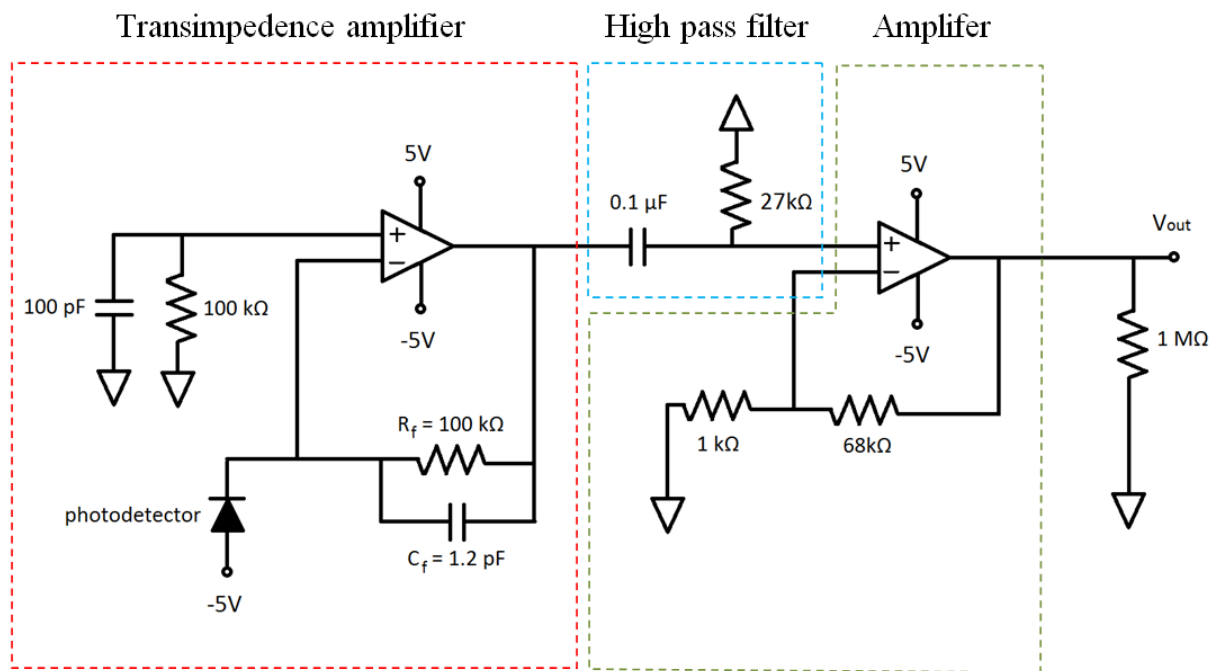


Figure 38 - Schematic of the signal conditioning circuit

In the transimpedance amplifier circuit, the photodiode is connected in reverse bias to reduce noise by lowering the diode capacitance C_{de} . The signal is converted into a voltage and amplified with a 100 kΩ feedback resistor R_f and a high bandwidth operational amplifier (OPA846, Texas Instrument, Dallas, Texas, U.S.A.). The feedback capacitor C_f is selected according to the relationship provided by the data sheet [74]

$$\frac{1}{2\pi R_f C_f} = \sqrt{\frac{GBP}{4\pi R_f C_{de}}} \quad (33)$$

where GBP is the gain-bandwidth product to produce a flat frequency response. The -3dB bandwidth

$$f_{-3dB} = \sqrt{\frac{GBP}{2\pi R_f C_{de}}} \quad (34)$$

is calculated to be 8 MHz. The voltage then passes through a high pass filter with 58 Hz corner frequency to remove the DC bias from stray light and 50 Hz ambient noise. A low pass filter is initially considered to remove high frequency noises. However, digital filtering is preferred due to the uncertainty in the actual output signal from the particles and to preserve the high frequency information. The last amplifier stage has a gain of 68, resulting in a total gain of 680000. The output signal is connected to the DAQ across an impedance matching resistor. The expected output voltage for particles diameter 0.5 to 2.5 μm are listed in Table 8.

Table 8 - Optical power of the forward scattering system and the expected output voltage after signal conditioning circuit

Particle diameter (μm)	Optical Power (W)	Output voltage (mV)
0.5	1.05e-08	7
1	1.16e-07	79
1.5	1.63e-07	111
2	7.91e-07	538
2.5	4.17e-07	283

3.1.4 Coincidence Error

When multiple particles are in the sensing region at the same time, the signal from each particle is indistinguishable from each other so the detector is only able to see 1 single continuous pulse. This is commonly referred to as coincidence error in particle counting. With a

recommended limit of 10% coincidence error [75], the maximum allowable concentration is calculated for the detection system. Assuming particle counting as a Poisson process where each particle entering the detection system is an independent event, the probability of the time between events T is greater than time interval t is given by

$$P(T > t) = e^{-cQt}. \quad (35)$$

The limiting time for the system is the pulse width of the particle, which is conservatively estimated to be 0.06 ms. The maximum concentration is found by solving equation 35 such that the probability for the time between events T being greater than 0.06 ms is 90%, i.e. $P(T > 0.06 \text{ ms}) = 0.9$. Figure 39 is the calculated maximum concentration with 10% coincidence error for different flow rate values. At 500 mL/min, the maximum concentration is $1767 \mu\text{g}/\text{m}^3$. At an extreme concentration $500 \mu\text{g}/\text{m}^3$, the coincidence error is 2.93%, confirming that the coincidence error is not an issue for this detector for environmental sensing applications.

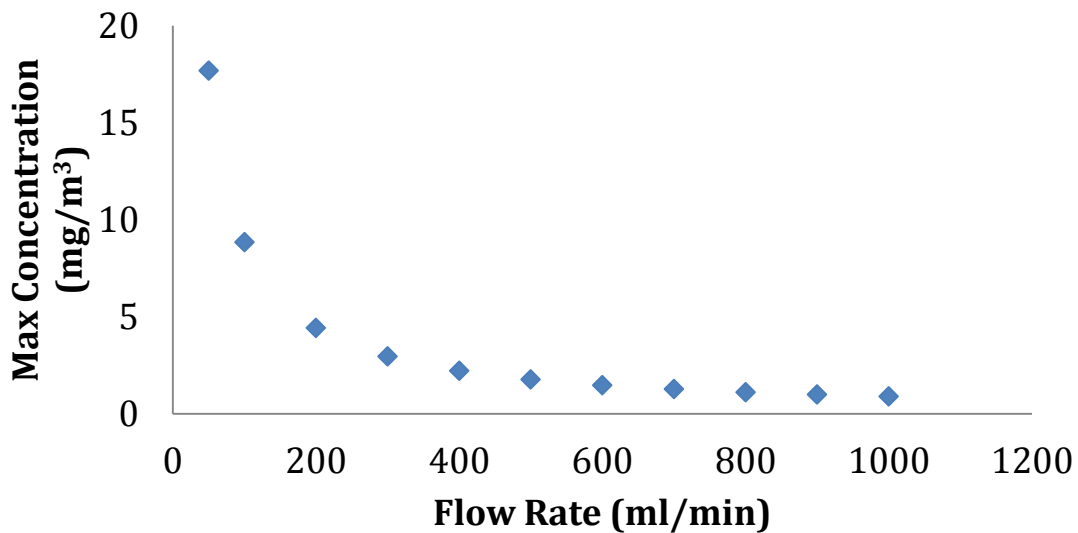


Figure 39 - Maximum allowable concentration for 10% coincidence error at different flow rates

3.1.5 Design Optimization

Figure 40 is a solid model of the forward scattering system based on the original calculations. However, counting efficiency of the fabricated design is very poor. To investigate this problem, the air flow is simulated through the optical detection chamber. The streamlines from the sampling air expands into the chamber as shown in Figure 41 (Left). To reduce the magnitude of flow expansion, a flow restricting aperture is added to the system by extending the rectangular flow channel into the chamber (Figure 41 Right). However, the counting efficiency is further reduced with the aperture in placed. This indicates that the intensity of scattering light is too low to be sensed at this distance. The particles travelling deeper into the detection chamber could be sensed in the original forward scattering design. As a result, the flow channel was moved closer towards the second light capturing lens.

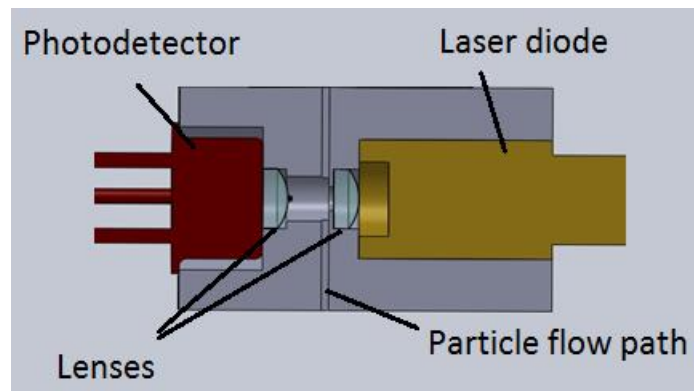


Figure 40 - Solid model of the original forward scattering system

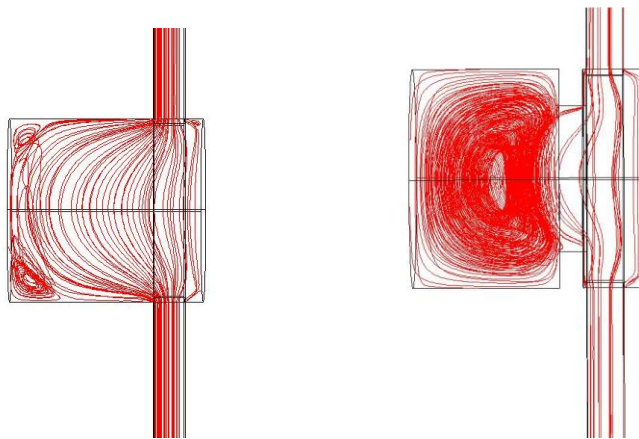


Figure 41 - Flow streamline of the original forward scattering detection chamber (Left) and detection chamber with flow restricting aperture.

Figure 42 (Left) is the cross section drawing of the modified enclosure design. By placing the flow closer to the detector, the sensing length of the system is reduced. Hence, the flow expansion effect is less significant (Figure 42 Right). The optical power of the system increases due to a smaller distance to sensor and a higher optical power density closer to the focal point. The new design parameters and calculated optical power are listed in Table 9 . The optical scattering increases from 58% for $0.5 \mu\text{m}$ particles to 7% for $2.5 \mu\text{m}$ particles compared to the original design. The expected voltage peak also increases accordingly as shown in Table 10. This design is used for all characterization experiments.

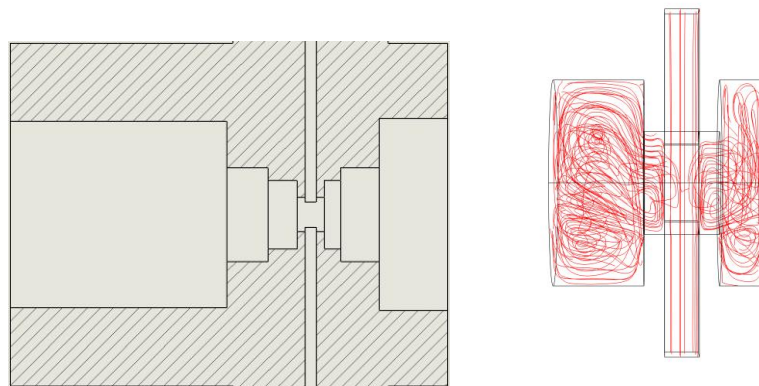


Figure 42 - Modified forward scattering detector enclosure: cross section drawing (left) and flow simulation (right)

Table 9 - Comparison of original forward scattering system and modified scattering system

	Original	Modified	
Detector Parameter			
Start Angle (°)	2	3	
End Angle (°)	13	17	
Wavelength λ (nm)	650		
Distance d_s (mm)	6.44	5.08	
Sensing length l_s (mm)	1	0.75	
Particle Diameter (μm)	Optical Power (W)		Increase (%)
0.5	1.05e-8	1.66e-8	58
1	1.16e-7	1.65e-7	42
1.5	1.63e-7	2.2e-7	34
2	7.91e-7	8.97e-7	13
2.5	4.17e-7	4.45e-7	7

Table 10 - Optical power of the forward scattering system and the expected output voltage after signal conditioning circuit

Particle diameter (μm)	Optical Power (W)	Output voltage (mV)
0.5	1.66e-8	11
1	1.65e-7	112
1.5	2.2e-7	149
2	8.97e-7	610
2.5	4.45e-7	302

4 Device Fabrication

4.1 Microfluidic Impactor

Following conventional soft polymer microfluidic channel fabrication process, the microfluidic impactor is formed with polydimethylsiloxane (PDMS) from a silicon wafer mold. The SU-8 polymer negative photoresist is patterned onto the silicon wafer through a photolithography process. The PDMS piece molded from the silicon wafer is then bonded onto another flat piece of PDMS to complete the channel. Figure 43 shows the fabrication process.

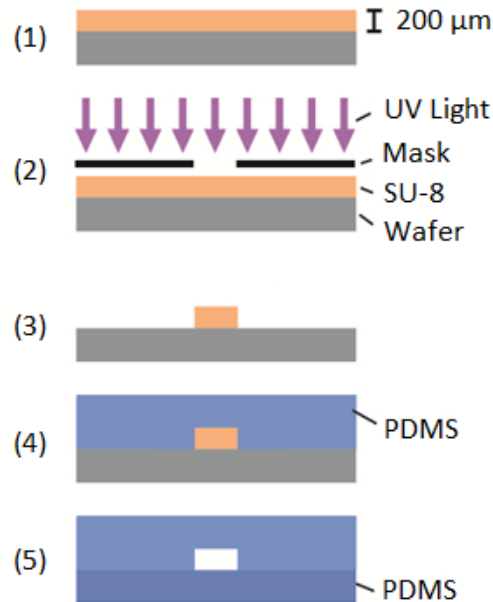


Figure 43 - Fabrication process of the PDMS microchannel

4.1.1 SU-8 Mold

The microchannel mold is fabricated with a photolithography process with negative photoresist SU-8 2075 polymer (Microchem, Westborough, MA, USA) on a silicon wafer. The fabrication recipe is tuned based on the SU-8 2075 datasheet [76] in order to achieve the desired 200 μm thickness with the equipment at UBC. The fabrication process is illustrated in steps 1 – 3 in Figure 43. The SU-8 photoresist is first spin-coated on a 100 mm mechanical grade silicon

wafer at 1000 rpm using a spin-coater (WS-400-6NPPB, Laurell Technologies, North Wales, PA, USA). The spin velocity profile follows the recommended program of an acceleration ramp step to 500 rpm over 10 seconds, a step to 1000 rpm over 30 seconds and a deceleration ramp step back to 500 rpm over 10 seconds. The spin acceleration profile for each step is set at 100, 300, and -100 rpm/s respectively. The wafer then undergoes a soft bake process on a leveled hot plate at 65°C for 7 minutes and at 95°C for 45 minutes. The temperature is gradually ramped down to room temperature from 95°C in order to minimize the stress induced on the SU-8 by a thermal gradient within the layer that could cause the SU-8 to delaminate. The SU-8 layer is exposed with UV light for 2.5 minutes at an intensity of approximately 6.7 mW/cm² through the transparency mask (CAD/Art Services, Bandon, OR, U.S.A.) to pattern the channel design. The wafer then undergoes a post-exposure bake on the hotplate at 65 °C for 5 minutes and at 95 °C for 20 minutes. The photoresist is developed with SU-8 developer with gentle agitation until the unexposed SU-8 on the wafer is completely removed.

The microchannel mold is shown in Figure 44. Typically multiple molds of the same design are created on the same wafer to produce more devices from the same molding process. Before fabricating the PDMS channels, each channel mold on the wafer is measured with a profilometer to ensure the height is 200 μm. Height variation along the length of the channel mold is a common problem caused by a non-uniform spin-coating process. By having multiple molds evenly distributed around the wafer, certain molds can still be used even if parts of the wafer do not meet height requirements.

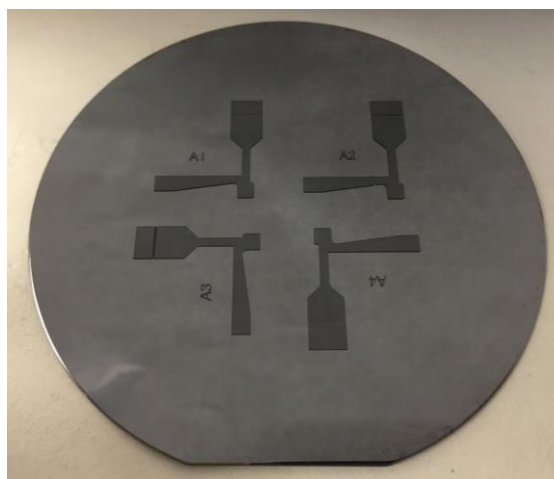


Figure 44 - SU-8 wafer of the microchannel

4.1.2 PDMS Channel

Step 4-5 in Figure 43 show the fabrication steps of the PDMS device. The microchannel is made of a two part polymer PDMS (Sylgard 184, Dow Corning). Approximately 70 grams of the polymer base is mixed with the hardener at 10:1 ratio. The combined solution is placed in a planetary centrifugal mixer (ARE-250, Thinky USA) for 2.5 minutes in the “mix” setting and 1.5 minutes in the “degas” setting. The PDMS is then poured onto the SU-8 mold with aluminum foil enclosing the edge of wafer to contain the liquid polymer. The PDMS on the wafer is degassed under vacuum for 30 minutes to remove air bubbles within the polymer. The wafer is then placed in an oven to cure at 80°C for 3 hours. The same molding procedure is repeated with a blank wafer to produce a flat PDMS piece, which forms the bottom wall of the microfluidic channel. The two pieces of PDMS are bonded together with oxygen plasma. After the two cured PDMS pieces are peeled off the wafer and cut to the desired size of the device, they are placed in a plasma cleaner (Harrick Plasma, Ithaca, NY, USA) for 1.5 minutes to activate the surface. The bonding surfaces are pressed together forming a seal. The device is then left in the oven at 80°C to improve adhesion.

To reduce particle loss caused by conventional vertical connections in microchannels, the inlet and outlet ports are placed in line with the channel. A hole puncher (Harris Uni-core) is used to make a 6 mm circular cut from the side wall of the PDMS device (Figure 45, a). A cut is made from the bottom of the device to release the core from the hole (Figure 45, b). A thin piece of PDMS is bonded to the bottom of the device to seal the cut. The inlet and outlet ports allow the microfluidic chip to be directly connected to the detector and the other tubing adapters in the experiment setup. An image of the fabricated PDMS microfluidic impactor is shown in Figure 46.

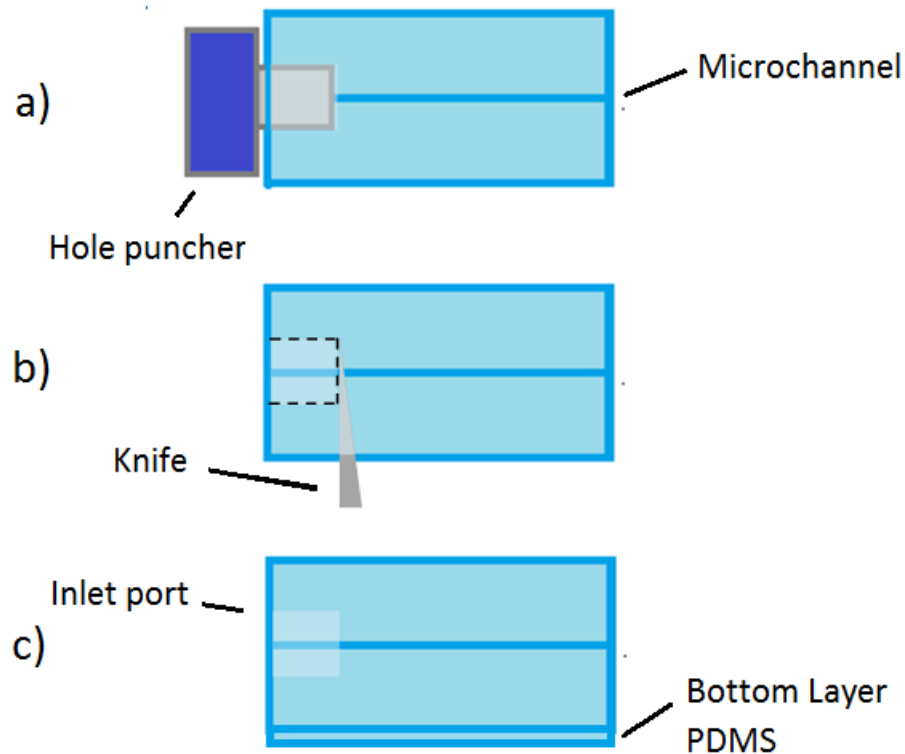


Figure 45 - Fabrication of inlet port - side view of PDMS device

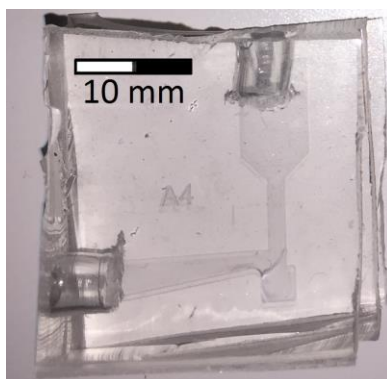


Figure 46 - Microfluidic particle trapping impactor

4.2 Optical Detector

The optical detector consists of a laser diode to illuminate the particles, a photodiode to sense the scattered light, two lenses to focus the laser light and direct scattered light to the detector, and a 3D printed enclosure to mount and align all the optical components. The enclosure is designed with a CAD model and printed locally. All the other parts are purchased commercially.

4.2.1 Optical Enclosure

The enclosure is a 15 mm x 15 mm x 20 mm rectangular block which consists of a 0.5 mm by 1 mm rectangular flow channel. The flow channel intersects with an optical chamber in which all the optical components in the detector are mounted. The inlet and outlet flow channel extends outwards in a 6.8 mm in length cylinder which acts as a tubing adapter with the microfluidic channel and the test tubings. A solid model of the enclosure is constructed in Solidworks (v 2013) based on the design requirements, matching the dimensions of the optical components. The generated STL file from Solidworks is used by a 3D printer (24, Objet) to produce the part accurate to 0.1 mm [77]. Since the 3D printer stacks layers of polymer materials to build the 3D part, supporting material must be used to produce empty voids within the part such as the optical chamber in the enclosure. The water-dissolvable supporting material in the enclosure is cleaned

out using a test tube brush. A 28 AWG wire is used to clear the flow channels. The enclosure is placed in a sonicator water bath to dissolve the remaining supporting material.

The default printing material offered by the printer manufacturer is a white, glossy plastic. The opacity of the plastic is not sufficient to absorb the light from the laser, causing the chamber to glow when the laser is turned on. To reduce the stray light intensity in the optical chamber, a thin layer of flat black chalkboard paint (206540, Rustoem) is applied on the enclosure surfaces where the optical components are mounted. The stray light is reduced but the enclosure still glows softly when the laser diode is on.

4.2.2 Light Trap

The light trap is located on the collection lens to absorb the focused laser light. It is formed by multiple layers of flat black acrylic spray paint (1602, Krylon). To apply the paint, a mask is first created by cutting out a 1 mm hole from a small, folded piece of aluminum foil using a 1 mm hole puncher (Harris Uni-core). The 4 mm glass lens (47-861, Edmund Optics) is taped to the aluminum foil with the hole centered on the convex surface. A thin layer of paint is sprayed onto the lens and allowed to dry. This process is repeated 6 times. When the aluminum foil is removed, a black 1 mm spot of paint remains on the lens. Multiple layers of aluminum foil are required to provide a sufficient height difference from the lens, allowing the aluminum foil to be lifted off without removing the paint on the lens. In addition, each layer of paint cannot be too thick as the paint will peel off if it connects the lens to the aluminum foil. For this reason, the punched hole is larger than the desired 0.5 mm of the light trap. Holding the lens in place with a pair of tweezers, the excess paint is carefully removed off the lens with a folded piece of lint-free wipe wet in acetone until the light trap is approximately 0.5 mm in size.

4.2.3 Optical Component Assembly

Figure 47 is an assembly drawing of the detector. The mounting holes in the enclosure are designed such that all the optical components are aligned once they are press fitted in. Both lenses are fitted into the enclosure first. When looking straight from the laser end of the enclosure, the light trap should obstruct the optical path, indicating the first lens is properly focused onto the light trap. The red 650 nm laser diode (AH-650-5-801, Aixiz) is inserted into the mounting hole. As a secondary inspection, when the laser light is powered, most of the laser light should be absorbed by the light trap and does not exit from the other end of the enclosure. The photodiode (SD100-14-21-021, Advanced Photonix) fits in the opposite end of the enclosure to complete the detection system. Due to the flat shape of the photodiode house which is 8 mm in diameter and 4 mm in height, the photodiode tends to wobble after it is pressed into the optical enclosure. A two part gel epoxy (Lepage) is used to fix the photodetector to the enclosure. Silicone sealant (SE1122 3TG, GE) is applied to both the laser diode and the photodetector around the edges to the enclosure to prevent flow leakage into the sample flow. Sealant is also applied to all the wires to ensure air is not drawn into the components.

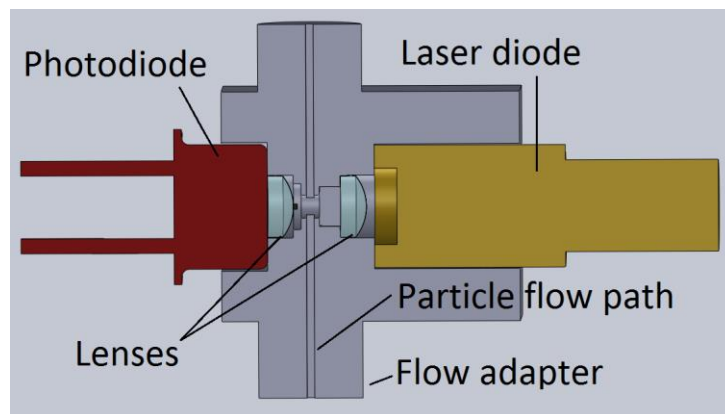


Figure 47 - Assembly of the detector

4.3 Integrated Device

To connect the impactor with the detector, the detector inlet flow adapter can be press-fitted into the outlet port of the microfluidic device. The soft PDMS of the microfluidic device makes a good seal with the harder plastics of the detector adapter which is sized slightly larger than the diameter of the inlet port. Figure 48 shows of the integrated device.

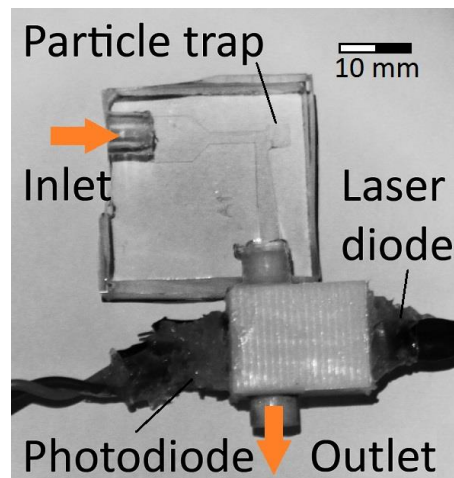


Figure 48 - Integrated device: microfluidic impactor attached to detector enclosure

5 Experimental Setup and Design

5.1 Particle Generation System

The airborne test particles are generated from suspensions of plain polystyrene microspheres (C-PS, Microsphere – Nanosphere, Cold Spring, NY, USA). Nitrogen is supplied to a 1-jet Collision nebulizer (CN241, BGI) set at 20 psi to produce a mist from the suspension. The mist then passes through a custom-built vertical diffusion drying column with brass mesh tubing surrounded by silica gel desiccant (Silica Gel Tel-Tale Desiccant, Indicating, Fisher Scientific Inc.) to remove the moisture. The flow rate of the nebulizer is fixed at 2 L/min of which 0.5 L/min of air transporting the particles is diverted to the test devices and the remainder is exhausted inside the fume hood. An aerodynamic particle sizer (APS) spectrometer is used as a reference instrument to count the number of particles at the test device outlet. Because the flow rate of the APS is set at 1 L/min, a precision needle valve is required on a parallel line to tune the flow to 0.5 L/min. Pure nitrogen gas from storage cylinders (Ni 4.8T, Praxair) is used for both lines to ensure the air supply is repeatable and contaminant-free. Figure 49 is a schematic of the experiment setup showing the balance of flow through the different sampling lines.

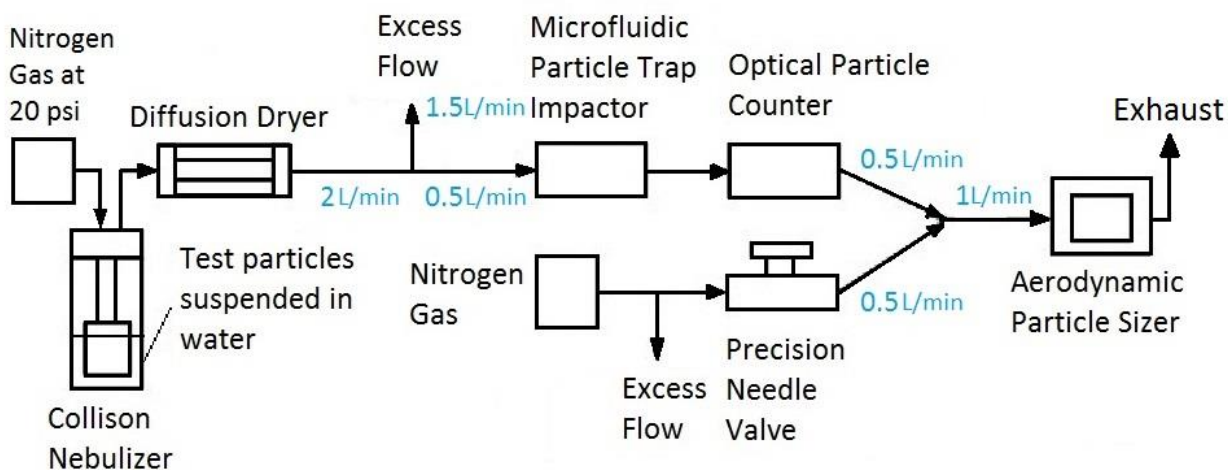


Figure 49- Schematic of experiment setup

5.1.1 Collison Nebulizer

The output characteristics of the nebulizer depend on the particle size. The manufacturer specifies a mass median diameter of droplets generated by the nebulizer to be 2.5 μm with a geometric standard deviation of 1.8 μm . As such, 68% of the particle diameter distribution will be between 1.4 to 4.5 μm and 95% of the particle diameter to be distributed between 0.78 and 9 μm [78]. Consequently, the efficiency of nebulizer particle generation decreases as the particle size of the test suspension increases because the liquid droplets are not large enough to transport the particles in suspension before the drying process. Approximately 1.5 ml of test suspension is used by the Collison Nebulizer in an hour at a back pressure of 20 psi. As the test suspension is consumed, the concentration will change over the duration of long experiments, causing the number of particles at the output to increase or decrease. Figure 50 shows output count variation for 1.5 μm test suspension measured by the APS in an hour which increases linearly by 25% over a 1 hour period. The particle counts at the nebulizer output typically increase for large particles. Because particle generation rate is limited by the nebulizer droplet size distribution for large particles, the particle concentration of the suspension increases as the fluid is consumed, increasing particle count. Conversely, because a single liquid droplet can contain multiple small particles, the output count is observed to decrease linearly for particles 1 μm or smaller as the particles in the suspension are consumed.

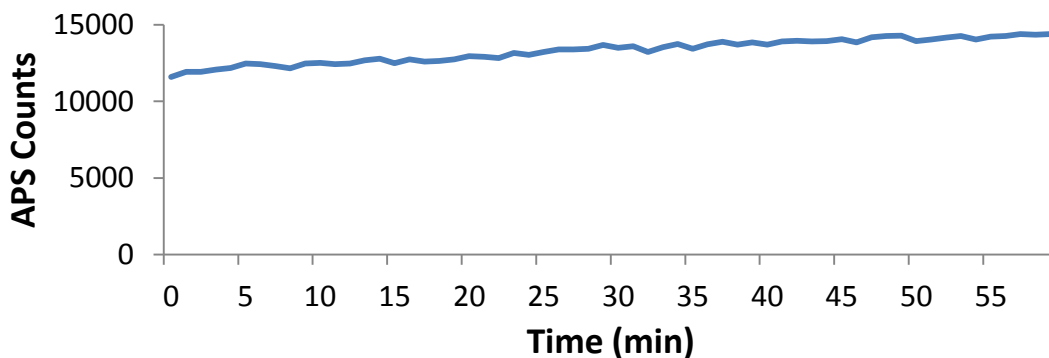


Figure 50 - 1.5 μm particle count over 1 hour

5.1.2 Particle Suspension

Fluorescent particles are typically used in microfluidics experiments for the particles to be imaged with a microscope. Plain, polystyrene microspheres are mainly used for this project because the particles are counted with a reference instrument. The test suspensions are diluted from the stock suspensions with distilled water. The concentration of the suspensions is set at 0.01 weight percent (wt%) for 0.5 to 1.5 μm particles. To compensate for the decrease in particle generation efficiency for larger particles, the concentration is increased to 0.025 wt% for the larger particle sizes. Table 11 provides a summary of the particle concentration used for each particle diameter. The particle diameter given by the supplier is measured using an optical technique called photon correlation spectroscopy. Since the APS measures the aerodynamic particle size, the two numbers are not expected to match. The diameter provided by the supplier is used to refer to the test particle size unless otherwise specified.

Table 11 - Summary of polystyrene suspension concentration

Particle diameter (μm)	Concentration (wt %)
0.5	0.01
1	0.01
1.5	0.01
2.0	0.025
2.5	0.025
3.0	0.025

5.2 Impactor Test Setup

Two experiments are designed to characterize the performance of the microfluidic particle trap impactor. The main experiment is the penetration efficiency test to determine the impaction characteristics of the microfluidic impactor and compare the experimental data with simulation results. The particle loss at the microfluidic device interface is also tested. Particle loss is a common issue in particle sampling instruments. Abrupt changes in cross sectional area of the

flow channel can cause particles to suddenly accelerate or decelerate, potentially impacting or depositing the particles onto the side wall of the tubing during transport. This is especially important for the microfluidic impactor as the flow undergoes roughly a 13:1 flow reduction between the tubing and microchannel inlet. The availability of only 1 APS and the linear change of particle output from the nebulizer are important considerations in the experimental design.

5.2.1 Penetration Efficiency Test Setup

To obtain the penetration efficiency curve for the microfluidic impactor, particles with diameters ranging from 0.5 to 3 μm at 0.5 μm increments are generated and passed through an impactor microchannel and a straight microchannel sequentially. The straight microchannel consist of inlet and outlet ports identical to the impactor which are connected by a straight channel with the same channel width and total flow path length as the impactor. The straight channel is used as a reference device to offset the effects of the inlet and outlet particle loss through the microchannel interface. The straight channel device is shown in Figure 51.

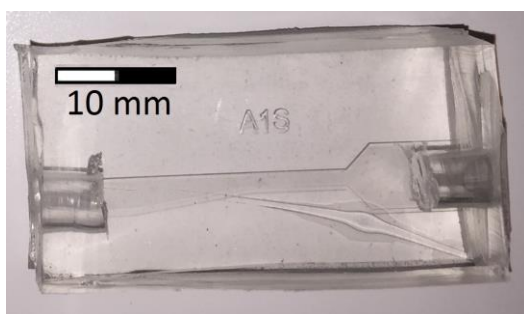


Figure 51 - Straight channel device

The number of particles exiting the outlet of the impactor and the straight channel are counted with the APS over a 6 minutes sampling interval. The measurements are taken in alternate order described in Table 12 to compensate for the effects of the linear variation in particle outputs when the nebulizer is operated for an extended period of time. The flow rate through the test devices is set at 0.5 L/min, designed for the 50% cut-off diameter to be 2.5 μm for the impactor.

The penetration efficiency is computed by the ratio of the particle counts at the impactor outlet to the particle counts at the straight channel outlet.

Table 12 - Penetration efficiency test measurement order

Test Number	Channel tested
1	Straight
2	Impactor
3	Impactor
4	Straight

5.2.2 Particle Loss Characterization Test Setup

To characterize the particle loss at the interface of the microfluidic device and the detector, 1 μm diameter particles are generated and passed through 3 test cases: the straight channel, the detector and a combined device. The combinations of the test cases are listed in

Table 13. 1 μm particles are used because the smaller Stokes number should theoretically allow them to closely trace the flow streamlines and it is the smallest size available for the APS to reliably detect. The straight channel test case is used to replicate the inlet and outlet loss at the impactor. The APS counts the number of particles at the output at each case. Keeping the same number of tubing adapters for all cases, the counts with test devices are compared with the counts with only the connection tubing to obtain the particle percentage loss. Similar to the penetration efficiency test, the measurements are taken in alternate 6 minutes sampling intervals to compensate for the effect of the linear decrease of particle output from the nebulizer. The flow rate is set at 500 mL/min to produce the same flow behaviour as the characterization test.

Table 13 - Particle loss test order for 3 test cases: detector, straight channel and combined

Sample Number	Test 1 - Detector	Test 2 - Microfluidic	Test 3 - Combined
1	Detector	Straight channel	Straight channel + Detector
2	No device	No device	No device
3	No device	No device	No device
4	Detector	Straight channel	Straight channel + Detector

5.3 Real-time Detector and Integrated Device Test Setup

5.3.1 Data Acquisition and Analysis

To obtain a count value from the detector for each experiment, the current output from the photodetector is first processed through the signal conditioning circuit. The output is then connected to a USB DAQ (USB-204, Measurement Computing) sampling at 500 kS/s to log the data. The saved data is processed in MATLAB (R2013b) with a custom script which allows the user to define the voltage threshold and pulse width requirements in which the voltage pulse is considered as a particle. The voltage threshold requirement is characterized by passing nitrogen through the detector and setting the threshold just above the background noise level. Typically the same voltage threshold can be used for all experiments as long as the optical component alignment in the detector is not modified.

5.3.2 Experiment Test Setup

The real-time performance of the detector is characterized through a 65 minutes continuous test in which the particle output concentration is changed and the detector count and the reference count are compared. The test begins with the nebulizer off to record a zero reference point. The reference measurement is to ensure the detector threshold voltage is set above the

background noise level such that the only counted pulses from the detector are particles in the ambient air. After 5 minutes, the nebulizer is switched on for the first particle count measurement at the highest concentration of particle suspension. After 15 minutes of particle measurements, the nebulizer is switched off for 5 minutes to obtain another zero reading. During this time, the particle suspension is diluted at 1:1 ratio with distilled water. The test continues at half of the particle suspension concentration for another 15 minutes. Changing concentration using this dilution method minimizes the disturbance on the test setup, reducing the chance of introducing noise to the system. The same process is repeated and the particle suspension is diluted 1:2 with distilled water. The test ends with the nebulizer off for 5 minutes as another zero reference. The ideal particle output from the nebulizer is illustrated in Figure 52. Data is recorded for the entire 65 minutes test period to verify how well the detector is able to track the concentration changes compared to the reference instrument. The transient effects in switching concentration can be observed by normalizing the data over the entire test period to the highest average concentration. The zero reference point throughout the test can be compared to ensure the result is not affected by background noise. The detector is tested with for 2, 1.5 and 1 μm particle suspension at 0.02%, 0.02% and 0.01% weight concentration respectively.

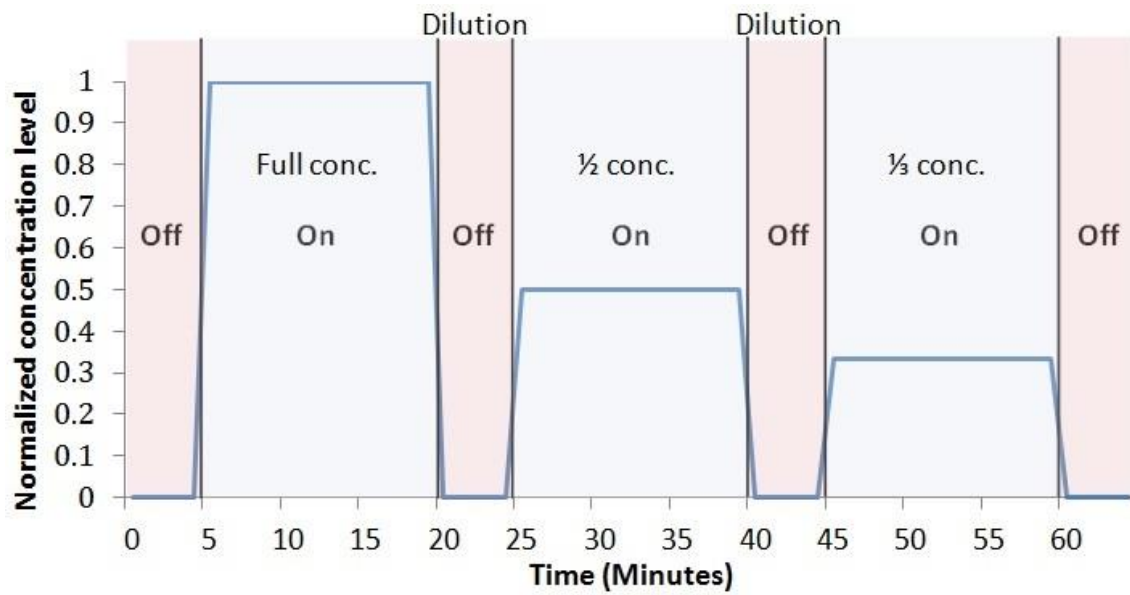


Figure 52- Ideal particle output from nebulizer for real-time continuous test

6 Results and Discussion

6.1 Impactor Characterization

The penetration efficiency of the microfluidic particle trap impactor is obtained by passing particles with diameters 0.5 to 3 μm in 0.5 μm increments through the device and comparing the output counts with the output counts of an equivalent straight microchannel. Microscope images of the particle trap are taken during 1 and 2.5 μm fluorescent particle tests to observe the particle deposition behaviour. Effects of particle humidity and prolonged use of the impactor on the penetration efficiency curve are also examined.

6.1.1 Penetration Efficiency

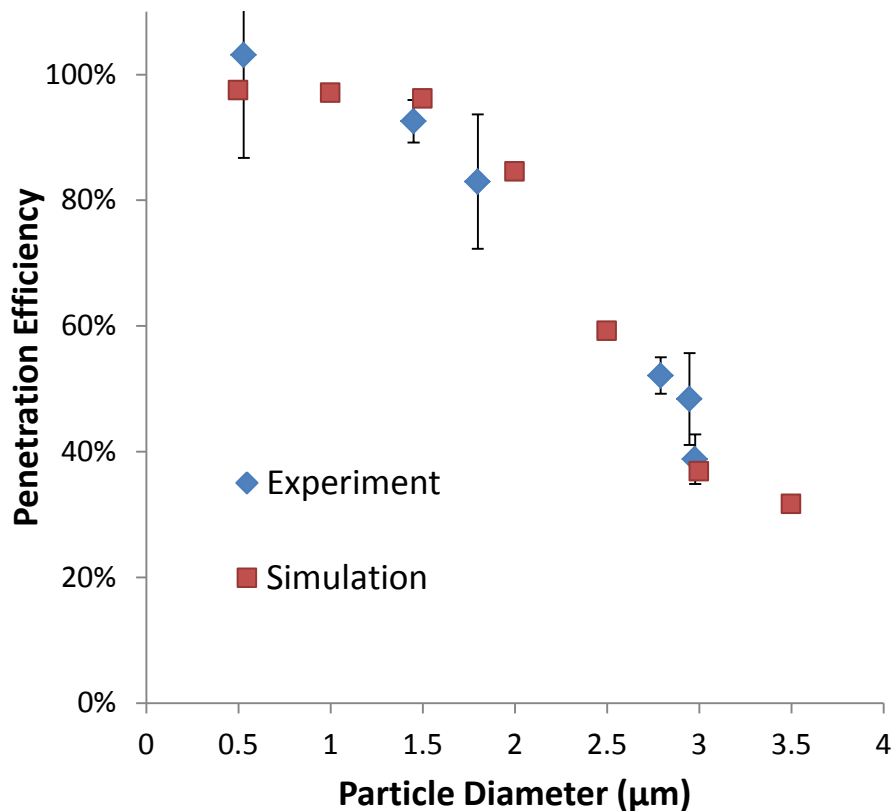


Figure 53 - Penetration efficiency curve of particle trap impactor: experiment vs COMSOL simulation

The experiment and simulated penetration efficiency curves of the impactor are shown in Figure 53. Each experimental data point is the average penetration efficiency value of two 24 minutes test samples. The error bars indicate 1 standard deviation. The experimental penetration efficiency curve agrees with simulation results. The 50% cut-off diameter is approximately 3 μm .

The particle diameter measured by the APS is typically normally distributed. The sum of all the particles in the distribution is used to calculate the penetration efficiency. The experimental and simulation aerodynamic diameter is compared as it is more relevant to the impaction characteristics of the particles for all penetration efficiency experiments. The aerodynamic particle diameter is calculated for each test sample by taking the mean particle diameter of the distribution and correcting for higher density of polystyrene particles. The aerodynamic particle diameter measured by the APS is typically larger than the diameter specified by the manufacturer, likely because the specified diameter value is measured optically. The moisture of the particles due to the nebulizing process can also cause weight gain of the particle, increasing the aerodynamic size of the particle. Table 14 provides a summary of the measured APS particle diameter.

Table 14 - Summary of APS measured diameter

Particle diameter in suspension (μm)	APS measured peak diameter (μm)	APS diameter after density correction (μm)
0.5	0.54	0.53
1	1.47	1.45
1.5	1.84	1.80
2	2.86	2.79
2.5	3.02	2.95
3	3.05	2.98

6.1.2 Particle Deposition

To examine the particle deposition characteristics at the particle trap region, 1 and 2.5 μm fluorescent particles are passed through two different impactor device at the same flow rate and concentration as the penetration efficiency test and microscope images are taken at the particle trap region at 1, 5, 10 and 20 minutes. Similar to previous test results, the diameter measured by the APS is approximately 0.5 μm larger than the specified value. The microscope images of the particle trap region for 1 μm particles are shown in Figure 54. After 1 minute (Figure 54 a), some particles have impacted the side walls near the entrance of the trap. Most particles are being carried deeper into the trap due to the flow recirculation inside the trap region similar to the simulation results. Some particles are also impacted at the outlet wall. These are likely the particles with a smaller mass or the particles travelling on a slower streamline. After 20 minutes (Figure 54 d), a large amount of particle buildup can be seen at the side wall. The significant particle accumulation at the side wall will likely influence the post-impaction behaviour of the particle.

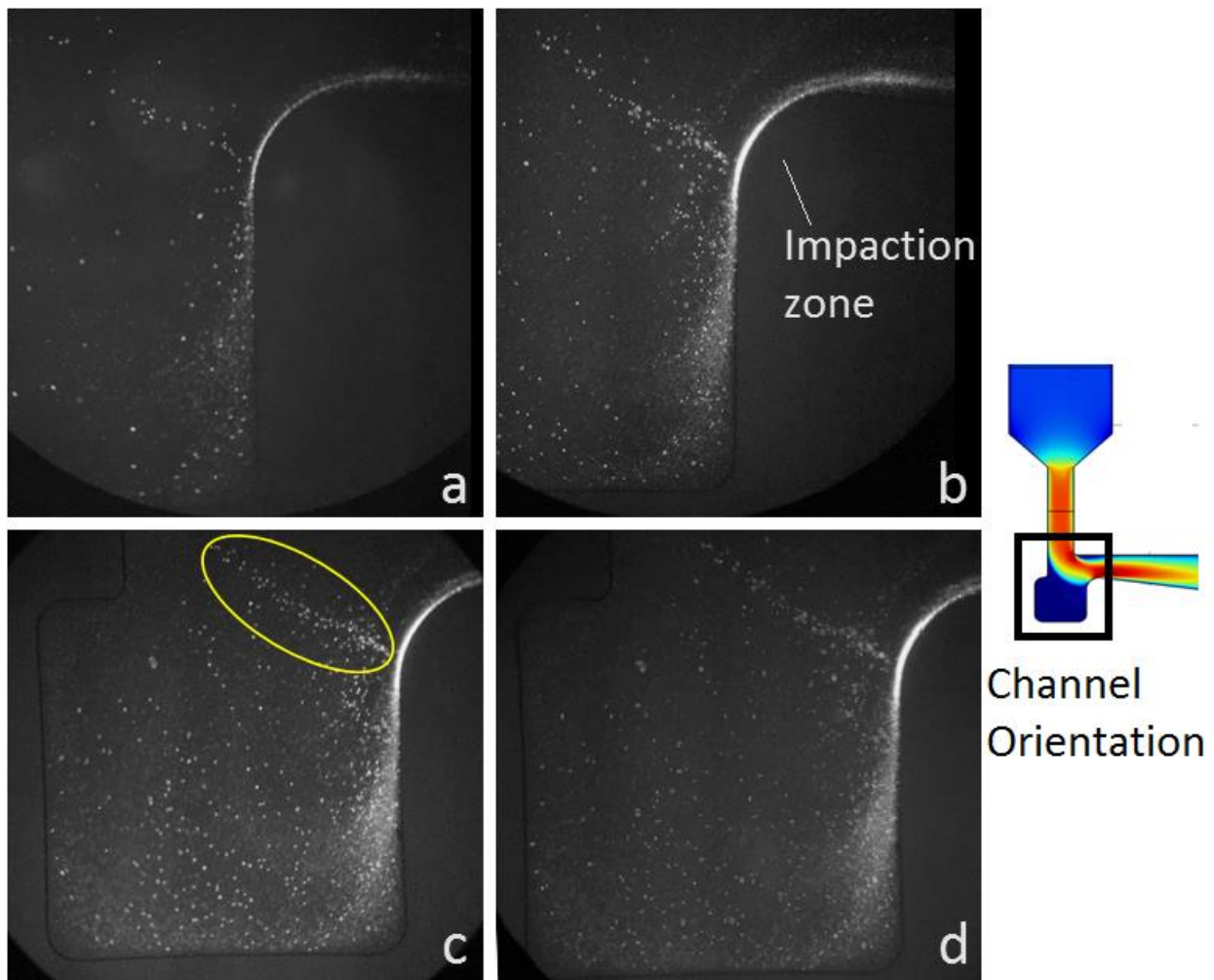


Figure 54 - Microscope image of florescent 1 μm particles after a) 1 minute, b) 5 minutes, c) 10 minutes and d) 20 minutes.

Figure 55 shows the microscope images of the particle trap region with 2.5 μm florescent particles. As expected, the number of impacted particles is higher due to the larger particle size despite the lower number of particles typically generated by the nebulizer for larger sizes. For 2.5 μm , more particles can be seen carried deep into the trap by the flow recirculation in the trap region compared to 1 μm particles, with some particles at the far top left corner of the trap away from the impaction side wall. Similar to the 1 μm case, the particle buildup at the impaction wall is significant. Particles also tend to accumulate on the top and bottom wall of the channels near the impaction zone. These particles likely impacted the side wall and deposited. Depending on the electrostatic characteristics of the particles, this accumulation could affect the particle

deposition process over time, either attracting the particles to increase deposition or repelling the particles so they are able to return to the faster streamlines towards the outlet.

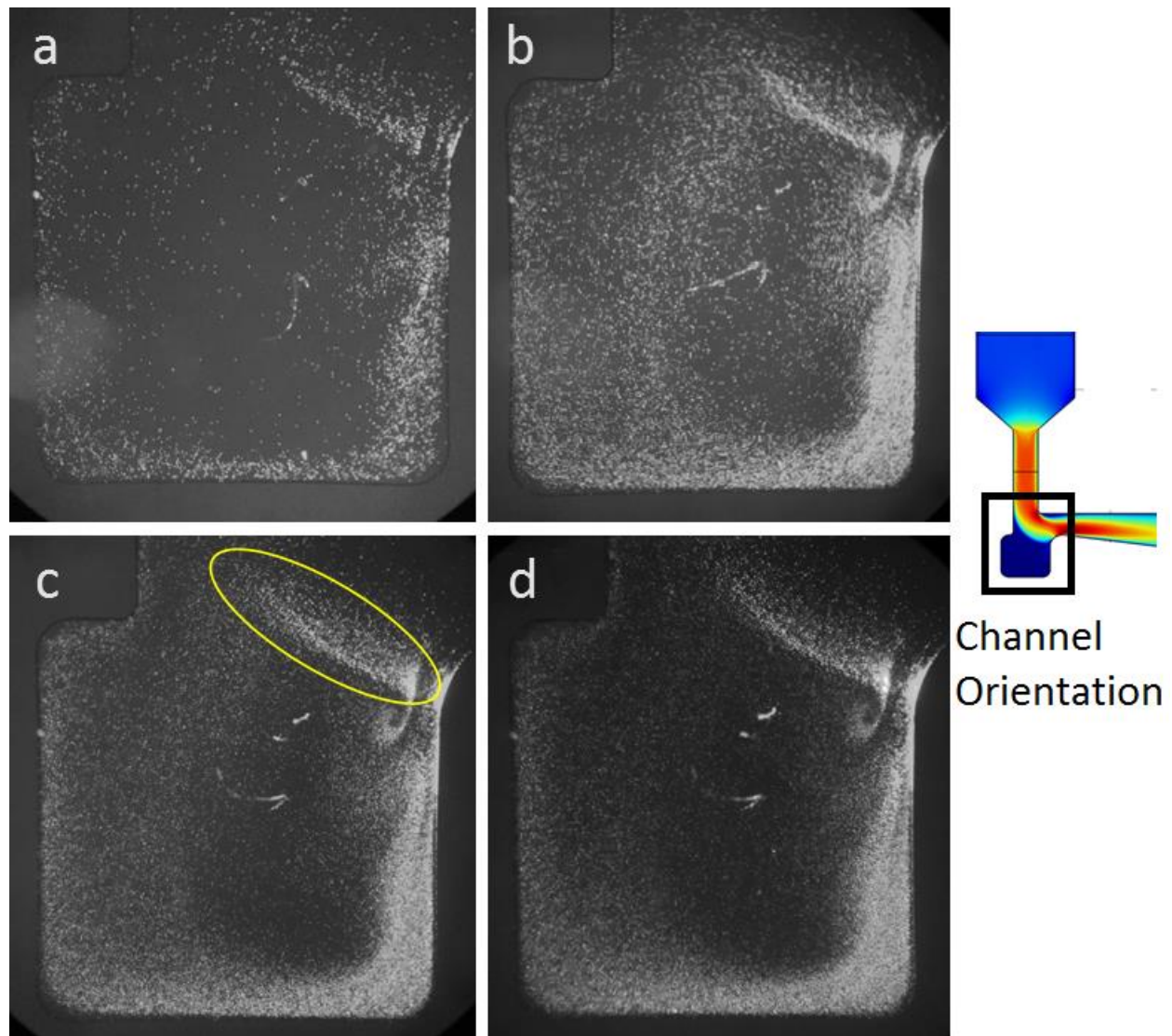


Figure 55 - Microscope image of florescent 2.5 μm particles after a) 1 minute, b) 5 minutes, c) 10 minutes and d) 20 minutes.

A line of particles deposited at the top and bottom wall leading towards the impaction zone can be observed for both 1 and 2.5 μm particles (circled in yellow in Figure 54 and Figure 55).

As observed in the simulation results, this is caused by a combination of particle recirculation and interactions with the slow flow velocity regions in the trap.

6.1.3 Effect of Humidity

The penetration efficiency curve is highly dependent on the humidity of the particles. This effect is shown in Figure 56 when the experiment is repeated with old desiccant gel with reduced drying effectiveness. For particles which are not completely dried, the number of small particles impacted increases while more large particles are transmitted.

The mechanism causing this difference is not fully understood. Moisture can cause weight gain of the particles [79] and also modifies the surface electroconductivity of the particles [80]. One hypothesis is the combined effect would increase the impaction of all particles due to weight gain. However, the surface effects play a larger role for small particles, causing the particle to stick since PDMS is an electric insulator. Since the inertial effect is dominant for larger particles, the surface effect does not significantly impact the penetration efficiency. The increased impaction also increased particle re-entrainment by particle bounce.

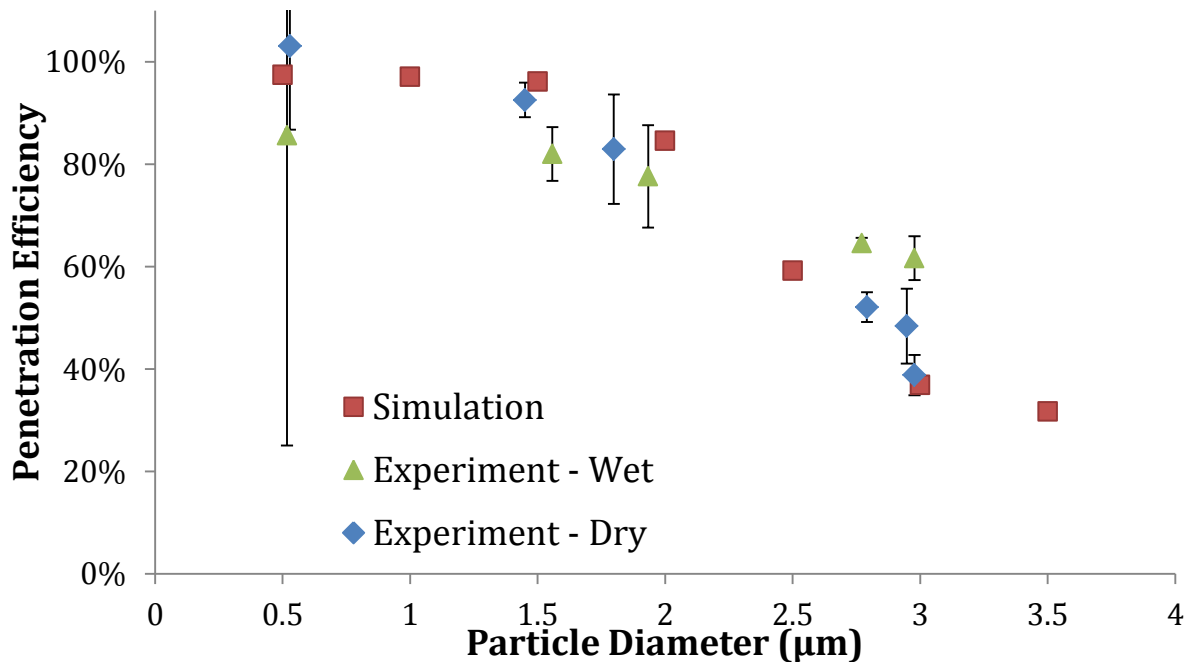


Figure 56 - Penetration efficiency curve of particle trap impactor: Simulation vs experiment for wet and dry particles

6.1.4 Particle Re-entrainment

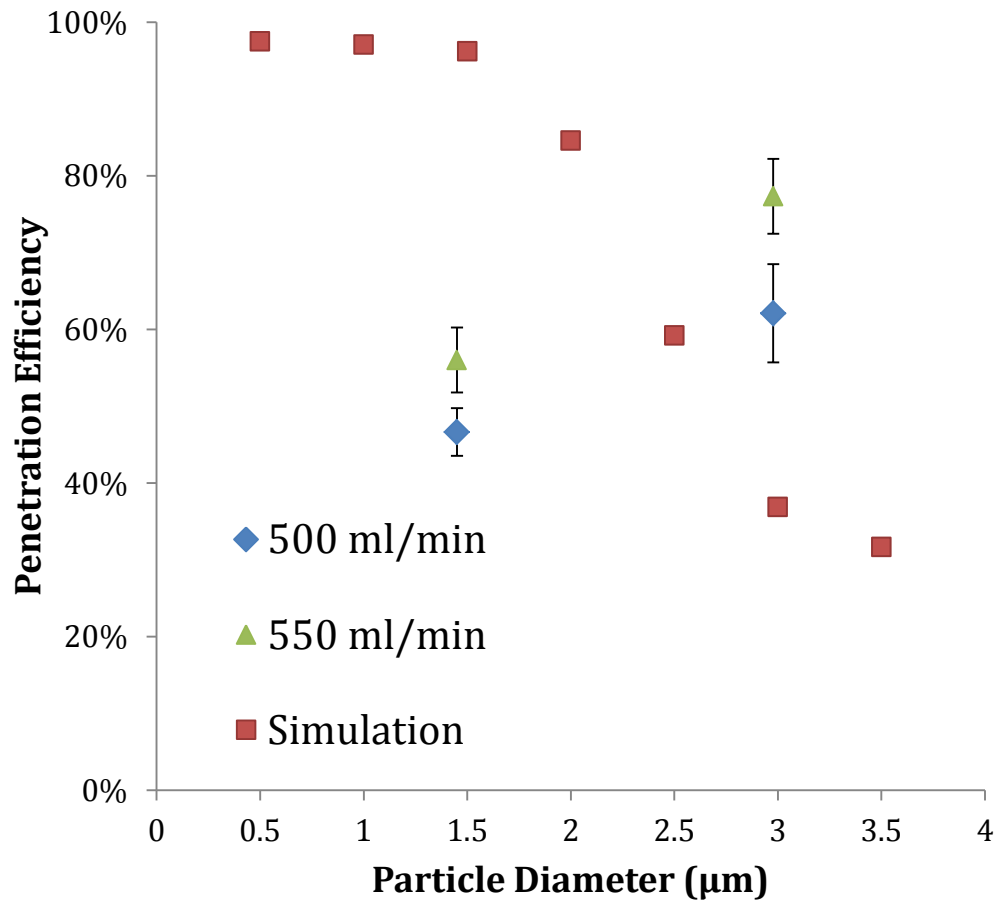


Figure 57 - Penetration efficiency data from failed microfluidic impactor

After prolonged use of the impactor in experiments, the penetration efficiency curve of the device changes significantly. For large particles, the penetration efficiency increases as shown in Figure 57. Based on the particle deposition images, this is likely caused by the particle accumulation reaching saturation near the particle trap region, increasing the chance of particle re-entrainment after impaction. The impacted particles typically deposit at the channel wall or bounce off it and deposit in the nearby region. However, when the nearby region is saturated with particles over time, the impacted particles cannot adhere well to the agglomeration of particles, promoting particle re-entrainment to the flow stream. This is verified by repeating the test at a 10% increased flow rate. According to simulation, increasing the flow rate increases the

particle velocity so more particles are able to enter the particle trap region, lowering the transmission. However, the higher flow rate in the experiment by 10% resulted in 20% and 25% increase of particle penetration for 1 and 2.5 μm respectively. Hence, the particles entering the particle trap region cannot be captured.

The penetration efficiency tends to decrease for smaller particles. One explanation is that the large number of particles in the trap creates more particle interaction, in which the smaller particles tend to be attracted. However, more data on the charge and the humidity of the particles would be needed in order to conclusively determine the deposition mechanism of the smaller particles.

Since the amount of particles passing through the microfluidic device is recorded by the APS for all the tests, the lifetime of the device can be estimated. The device failed after 29 μg of particles was sampled through it. At the regulatory standard of 12 $\mu\text{g}/\text{m}^3$ and flow rate of 500 mL/min, this corresponds to 80 hours of run-time. For most environmental applications at lower concentrations, the lifetime of the device would be longer.

6.2 Particle Loss Characterization at Device Interface

The particle loss for the detector, the microfluidic inlet and outlet and the combined device is tested. The average particle loss through the detector is 30%. This number appears to be high for 1 μm because the small size should theoretically allow the particles to quickly match the flow velocity changes. However, the result could be exaggerated as the APS typically measures 1 μm test particles as 1.8 μm . 51% of the particles are lost through the inlet and the outlet of the straight channel. Particles can be observed to deposit at the corners of the PDMS wall by visual inspection. The theoretical loss of the combined device is computed to be 65%, assuming the 70% of particles exiting the detector experience 51% loss. However, the particle loss through the combined device was measured to be 77%. The direct connection between the microfluidic

device and the detector introduces 12% of the particle loss. A summary of the particle loss results is shown in Table 15.

Table 15 – Average particle loss percentage for 3 test cases: detector, straight channel and combined

Particle Loss (%)	Detector	Straight Channel	Combined	
			Theoretical	Experiment
	30	51	65	77

6.3 Particle Pulse Characteristics of Detector

Figure 58 shows sample voltage pulses from 1.5 μm test particle (Left) and ambient air particle (Right) measured by the detector after the signal conditioning circuit. The pulse width of the signals is around 30 μs which agrees with theoretical design calculations. The pulse width is limited by time of the particles in the sensing region. The effect is shown in the ambient air particle which has a much larger scattering intensity compared to the test particles. The sharp rising and falling edges of the pulse indicates the boundaries when the particle enters the sensing region. In comparison, the test particle pulse has a smoother Gaussian shape. This is likely caused by the Gaussian distribution of the light intensity as the laser light is focused into a cone shape by the lens.

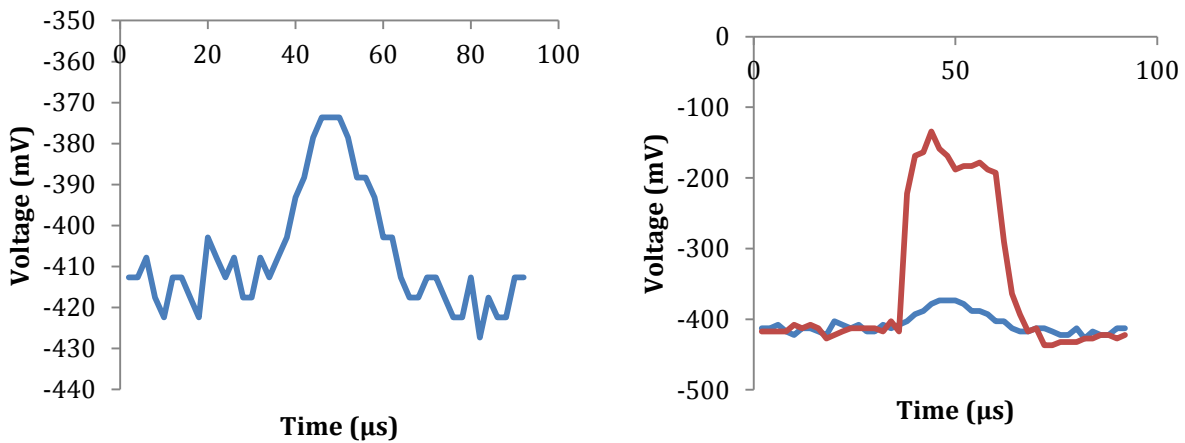


Figure 58 - Sample pulse from the detector - 1.5 μm (Left) vs ambient air particle (Right)

The poor signal-to-noise ratio of the detector can be seen in Figure 58. The threshold voltage must be set close the background noise level to detect the particles. Due to the high bandwidth of the circuit and the lack of noise isolation, the high frequency noise received by the detector is amplified. In addition, the fluctuation in laser intensity can also be amplified as the detectors sense stray light from the laser source. The experimental peak voltage is calculated by the difference of the peak voltage and the average background voltage. The experimental peak voltage is in the same order of magnitude compared to the theoretical calculation shown in Table 16.

Table 16 - Peak voltage signal of particle pulses - Theoretical vs Experimental Average

Particle diameter (μm)	Peak voltage signal (mV)	
	Theoretical	Experiment
1	79	35
1.5	111	108
2	538	48

Figure 59, Figure 60 and Figure 61 are histograms of peak voltage for 1, 1.5 and 2 μm test particles. There is no correlation between intensity and particle size. Although the correlation exists in theory, it is difficult to observe due to the arrangement of the detector. The scattered light intensity is likely more sensitive to the combined effect of incident light intensity and the distance from the detector. As a result, the intensity distribution is likely attributed to the particle position along the width for the channel.

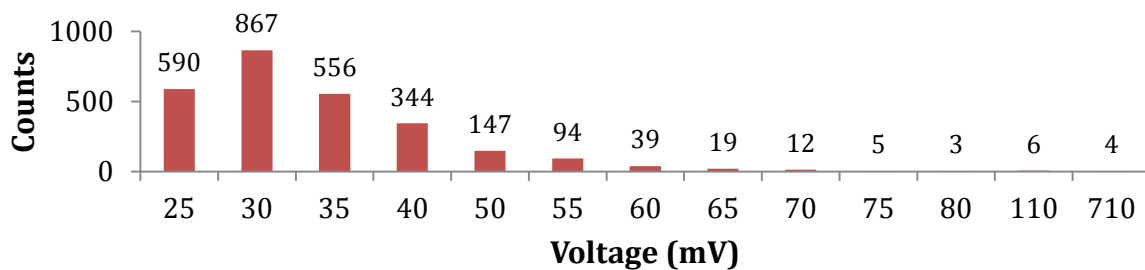


Figure 59 - Pulse voltage histogram for 1 μm test particles

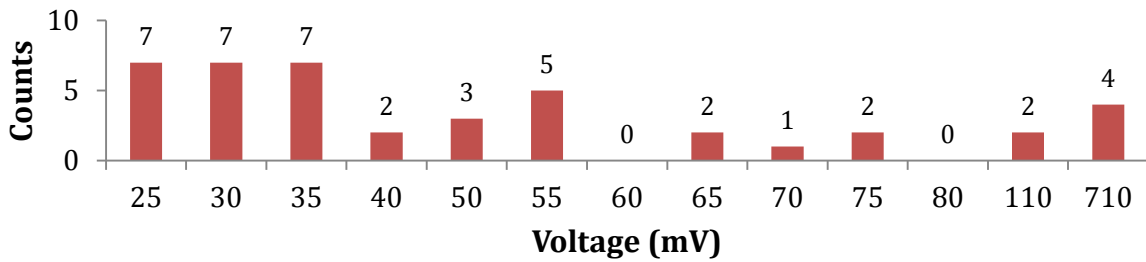


Figure 60 - Pulse voltage histogram for 1.5 μm test particles

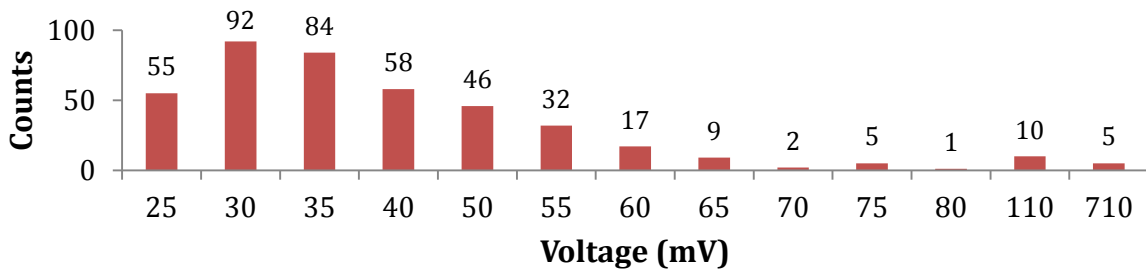


Figure 61 - Pulse voltage histogram for 2 μm test particles

6.4 Real-time Detector Characterization

The real-time performance of the detector is evaluated with a 65 minutes continuous test for 3 particle sizes: 1, 1.5 and 2 μm . The particle size distribution from the nebulizer is examined. The detector counts are plotted against the APS counts for each 1 minute sampling interval to assess the data correlation. The average counts at each test concentration for the detector and the APS are also computed and plotted. With the 1 minute sampling interval count normalized to the highest average count, the continuous data for the entire duration of the test is shown to evaluate the responsiveness of the detector counts to concentration changes compared to the APS counts.

A threshold voltage of -0.39 V is fixed for all the real-time detector characterization tests. Voltage signals from the photodetector which exceeds this threshold value are counted as a

particle. For optical detector test, the particle size is referenced to the supplier specified optically measured diameter instead of the aerodynamic particle diameter.

6.4.1 2 μm Test Particles

For 2 μm particle suspension, two distinct peaks for the particles counts can be observed by the APS at 1.843 and 2.839 μm as shown in Figure 62. The source of the smaller peak is caused by residual particle suspensions of another particle size not completely rinsed out in the cleaning process. The peak diameter for 2.0 μm is slightly larger 2.839 μm . The 2.0 μm provided by the manufacturer is from optical measurements which differs for the aerodynamic diameter measured by the APS.

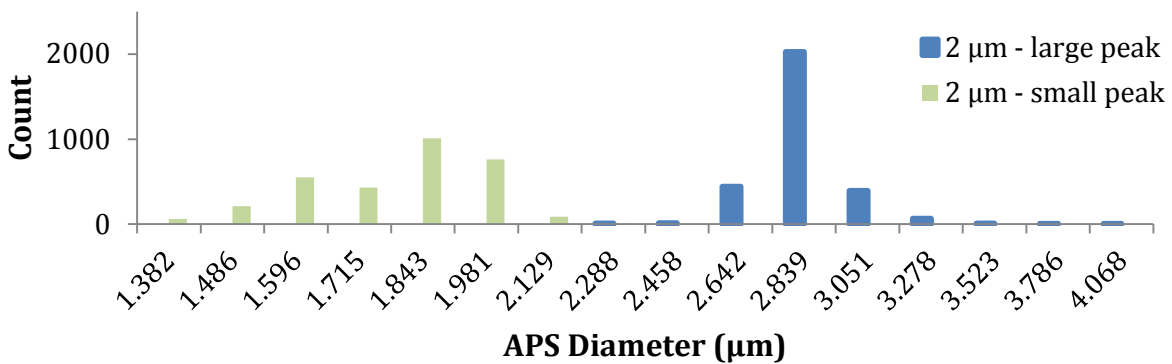


Figure 62- APS size distribution of test particles from 2 μm polystyrene suspension, two peaks at 1.843 and 2.839 μm .

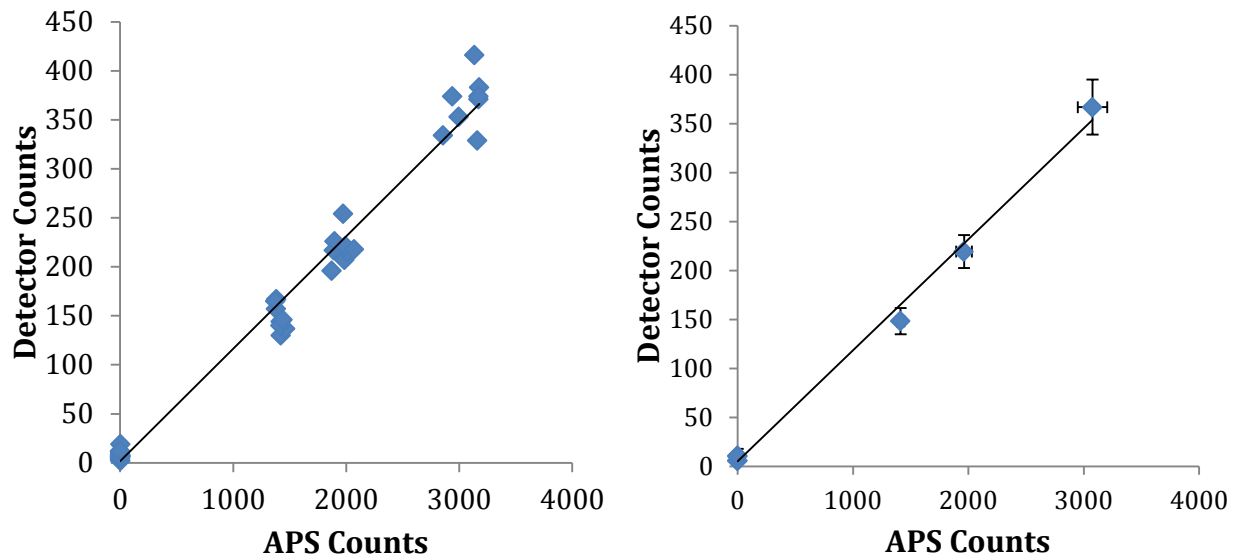


Figure 63 - Detector count vs APS reference count of larger peak centered at 2.839 μm for 2 μm particle suspension- Left: 1 minute sampling interval, Right: Average count at each particle concentration, error bars represents ± 1 standard deviation.

The detector counts show an excellent linear correlation with the APS counts when only the larger particle diameter centered at 2.839 μm in the distribution is considered as shown in Figure 63. However, the correlation is poor when the detector counts are compared with the smaller diameter APS counts in Figure 64. This result is reasonable because larger particles are expected to have a higher light scattering intensity, increasing the counting efficiency. The continuous data in Figure 65 demonstrate that the detector is capable of tracking concentration changes similar to the APS.

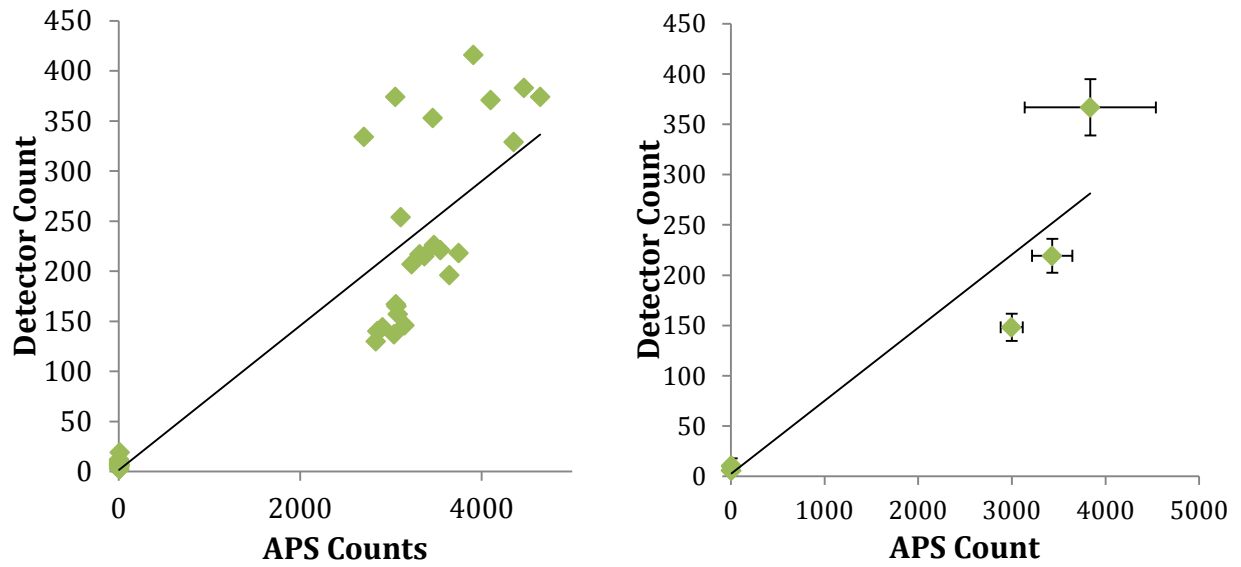


Figure 64 - Detector count vs APS reference count of smaller peak centered at 1.843 μm for 2 μm particle suspension- Left: 1 minute sampling interval, Right: Average count at each particle concentration, error bars represents ± 1 standard deviation.

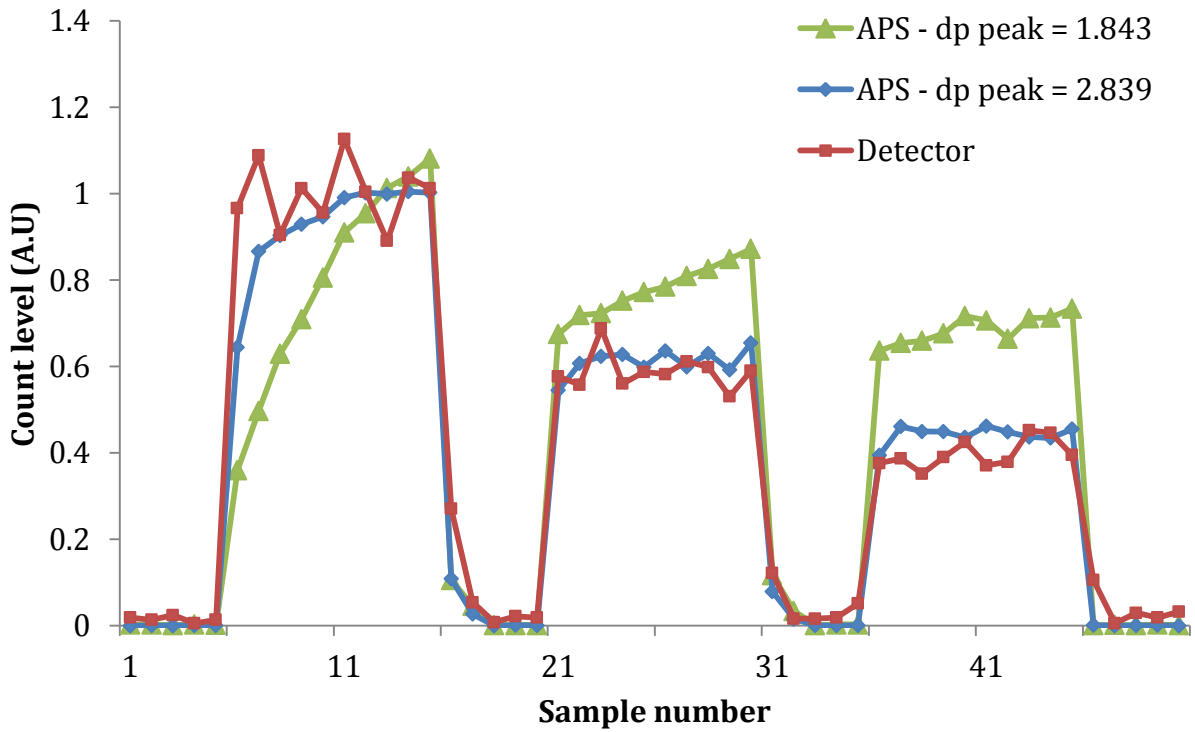


Figure 65 - Count levels of detector and APS measurement of 1.843 and 2.839 μm diameter peaks for 2 μm particle suspension over entire test period normalized to the average concentration of the highest particle concentration

6.4.2 1.5 μm Test Particles

The aerodynamic diameter measured by the APS for 1.5 μm is also larger, centered at 1.981 μm shown in Figure 66. From the detector and APS plots for 1 minute sampling interval, (Figure 67, Left), the counting efficiency is much lower for 1.5 μm , resulting in a high measurement error. The linear correlation can be observed from the average counts of each particle concentration.

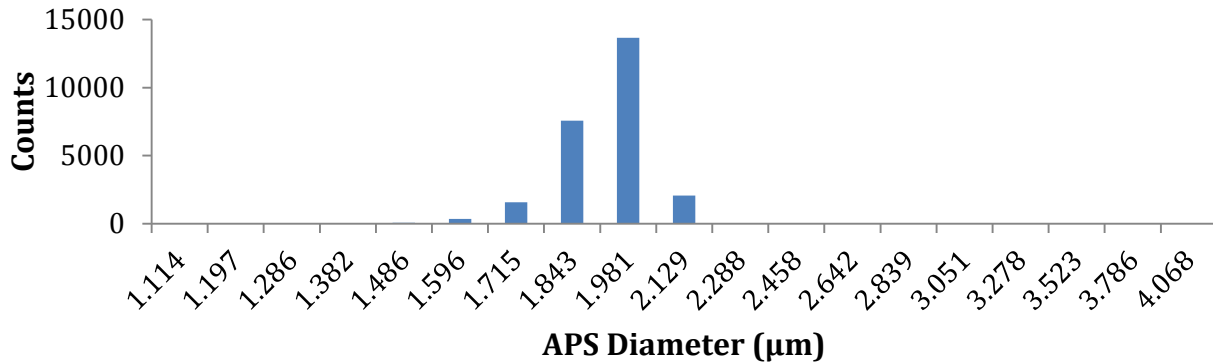


Figure 66 - APS size distribution of test particles from 1.5 μm polystyrene suspension

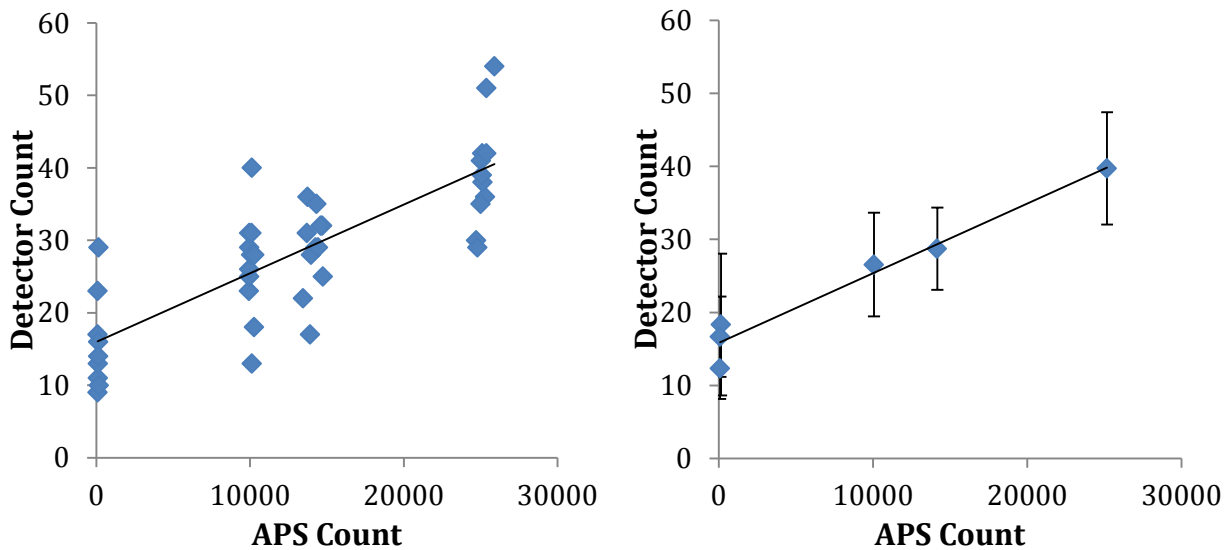


Figure 67 - Detector count vs APS reference count for 1.5 μm particle suspension- Left: 1 minute sampling interval, Right: Average count at each particle concentration, error bars represents ± 1 standard deviation.

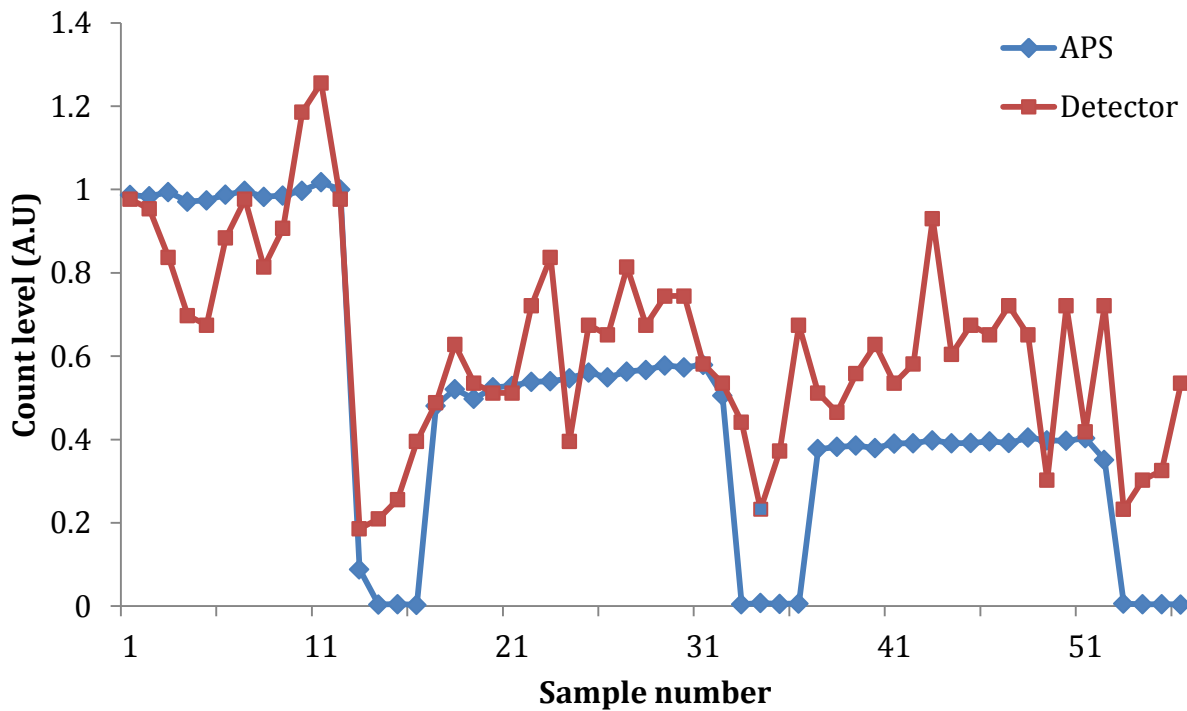


Figure 68 - Count levels of detector and APS measurement 1.5 μm particle suspension over entire test period normalized to the average concentration of the highest particle concentration

The random error in the measurement is expected to be high when the number of counts is low. This is shown in the continuous plot in Figure 68. The detector counts fluctuate significantly but roughly follow the trend of the APS counts.

6.4.3 1 μm Test Particles

Figure 69 shows the APS size distribution from 1.0 μm particle suspension. Because of the improved nebulisation efficiency for smaller particles, the number of counts is very high. There's also an increased in aerodynamic diameter compared to the particle specification provided by the manufacturer.

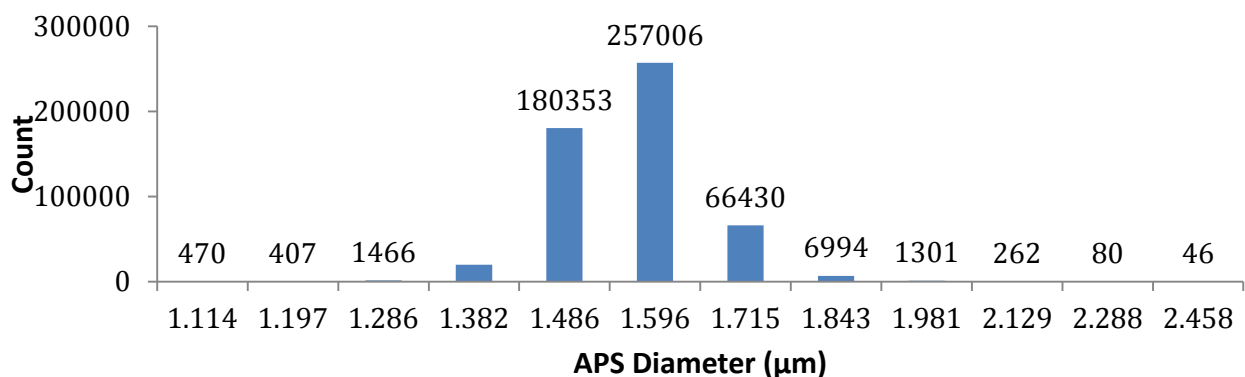


Figure 69 - APS size distribution of test particles from 1.0 μm polystyrene suspension

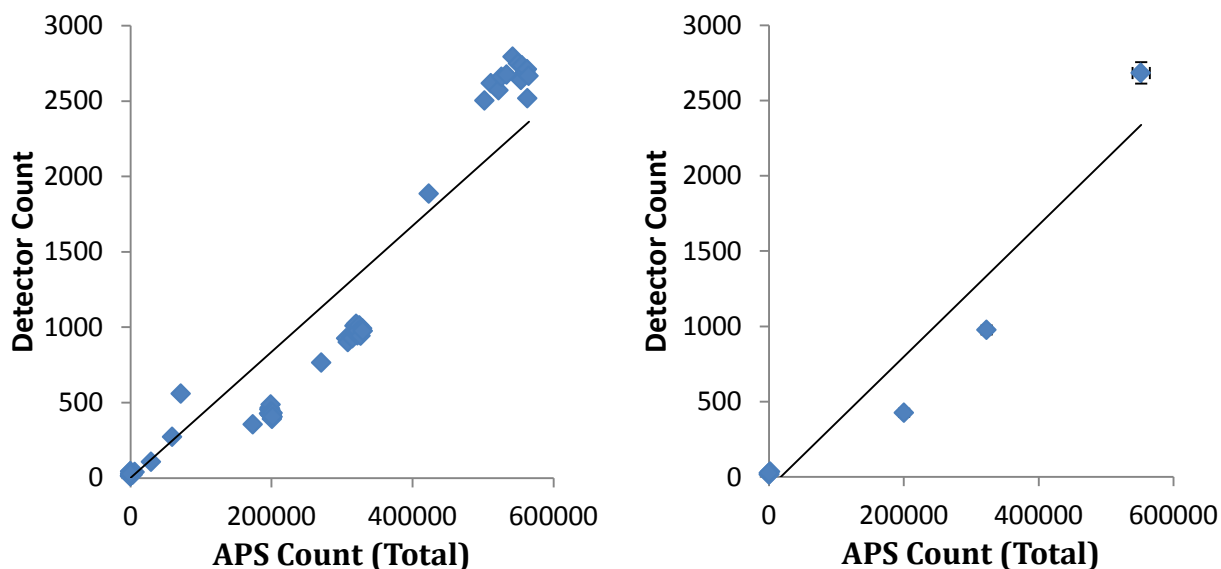


Figure 70 - Detector count vs total APS reference count for 1 μm particle suspension- Left: 1 minute sampling interval, Right: Average count for each particle concentration, error bars represents ± 1 standard deviation.

As expected, the counting efficiency is poor for 1 μm particles. However, a linear correlation can still be observed from the 1 minute sampling intervals data in Figure 70. The detector counts are plotted with the APS counts larger than 2.129 μm for 1 μm test particles in Figure 71. The correlation further improves in this case when only the large particle sizes are considered from the APS. However, the detector counts are greater than the APS counts in the specific size range, indicating the detector must be counting a combination of sizes over the entire range with higher efficiency for large particles. These particles larger than 2.129 μm could

be caused by particle agglomeration in the nebulisation process when multiple particles are within a single droplet before the mist is dried by the drying column. Likewise, the detector counts trace the larger diameter particle counts given by the APS much more closely in the continuous data shown in Figure 72 compared to the total particle counts.

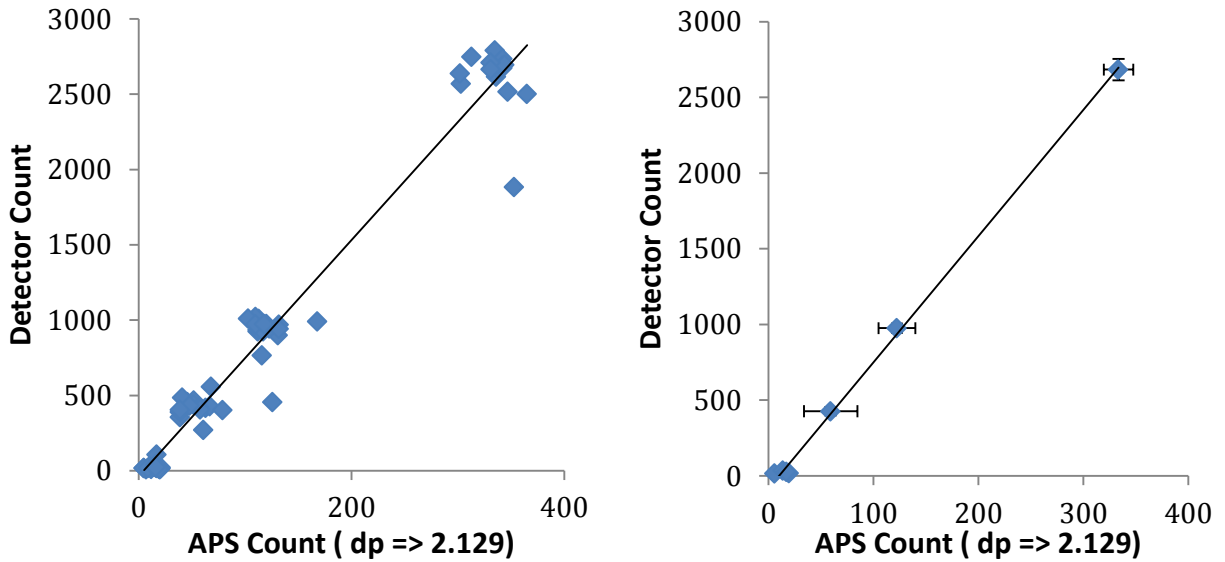


Figure 71 - Detector count vs APS reference count larger than 2.129 μm diameter for 1 μm particle suspension- Left: 1 minute sampling interval, Right: Average count at each particle concentration, error bars represents ± 1 standard deviation.

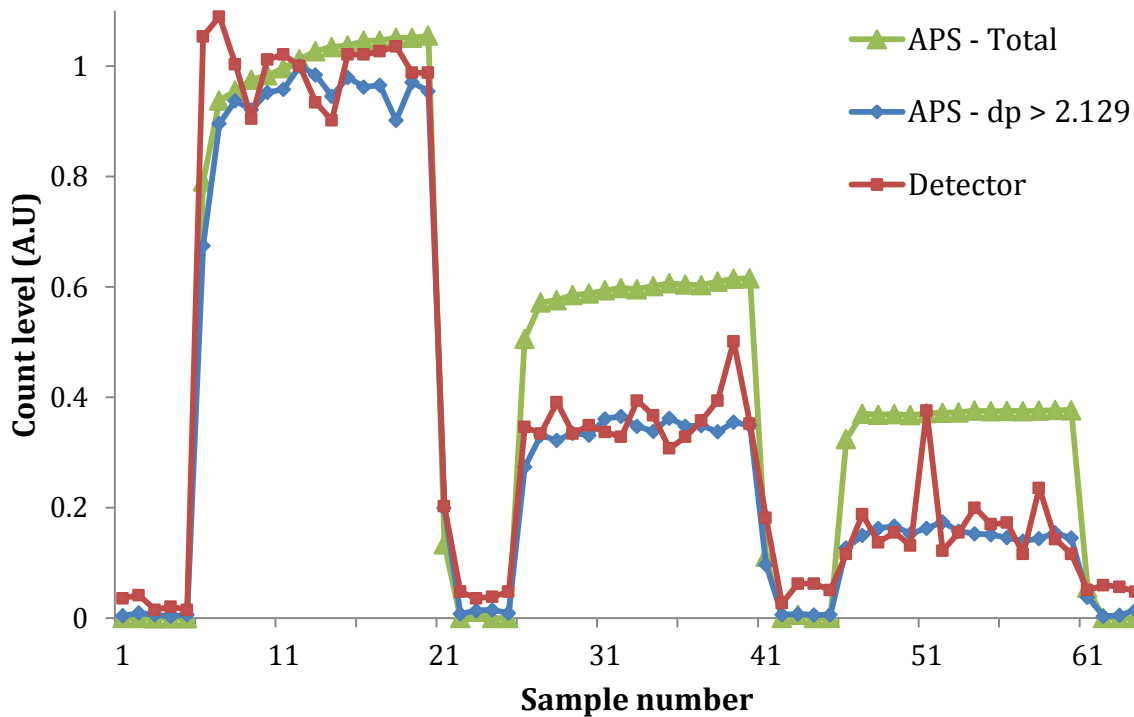


Figure 72 – Count levels of detector and APS measurement for 1 μm particle suspension over entire test period normalized to the average concentration of the highest particle concentration

6.4.4 Counting Efficiency

Table 17 provides a summary of the detector test results and the respective counting efficiencies. The counting efficiency is computed by taking the ratio of the average detector count and the average APS count for each particle concentration. For 2 μm particles, the counting efficiency is around 10%. The efficiency drops significantly to 0.2% for 1.5 μm particles due to the reduced scattering intensity for smaller particles. The efficiency also decreases as the suspensions are diluted for 1 and 2 μm particles. This is likely caused by a higher relative error at low counts. Conversely, the efficiency increases for 1.5 μm as the suspension concentration decreases. The number of counts for 1.5 μm for each sample is not statistically significant for an accurate measurement, i.e. the number of count is prone to random noise and not sensitive to particle concentration changes. By diluting the suspension, the APS

counts is effectively reduced without changing the detector counts, hence, resulting in a higher perceived, count efficiency value.

Table 17 - Summary of detector test parameters and counting efficiency for 1, 1.5 and 2.0 μm diameter

Particle size (μm)	APS peak diameter (μm)	Starting conc. (wt%)	Max count for 1 min		Counting Efficiency (%)		
			APS	Detector	Full conc.	Half conc.	1/3 conc.
1	1.6	0.01	564994	2792	0.49	0.30	0.21
1.5	2.0	0.01	25901	54	0.16	0.20	0.26
2	2.8	0.02	3178	416	12.0	11.2	10.5

6.5 Integrated Device

To demonstrate the functionality of the integrated particulate matter monitor, the same real-time continuous test is repeated with the impactor connected upstream of the detector. However, in the experiment process, the laser diode from the original detector setup failed. The laser diode was replaced and the optics within the detector was reconfigured for the integrated test. As a result, the linear correlation between detector counts and APS counts is not the same between the two sets of results.

6.5.1 2 μm Test Particles

For the same suspension concentration, the detector counts and the APS counts are much lower as shown in Figure 73 due to the effect of the impactor. The linear correlation can be observed again once the average counts are computed for each concentration. The random error for both counts is observably higher as the number of counts is too low for a statistically significant measurement over a 1 minute sampling interval. This effect is shown in Figure 74 in which the detector counts are able to trace the APS counts with high variability.

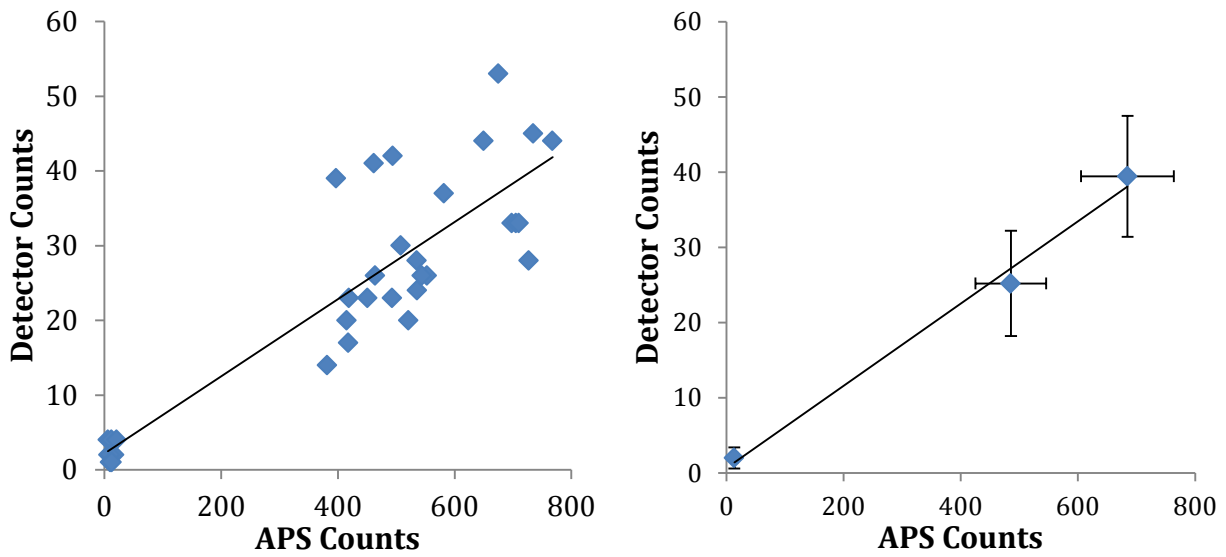


Figure 73 – Integrated device count (impactor and detector) vs total APS reference count for 2 μm particle suspension - Left: 1 minute sampling interval, Right: Average count for each particle concentration, error bars represents ± 1 standard deviation.

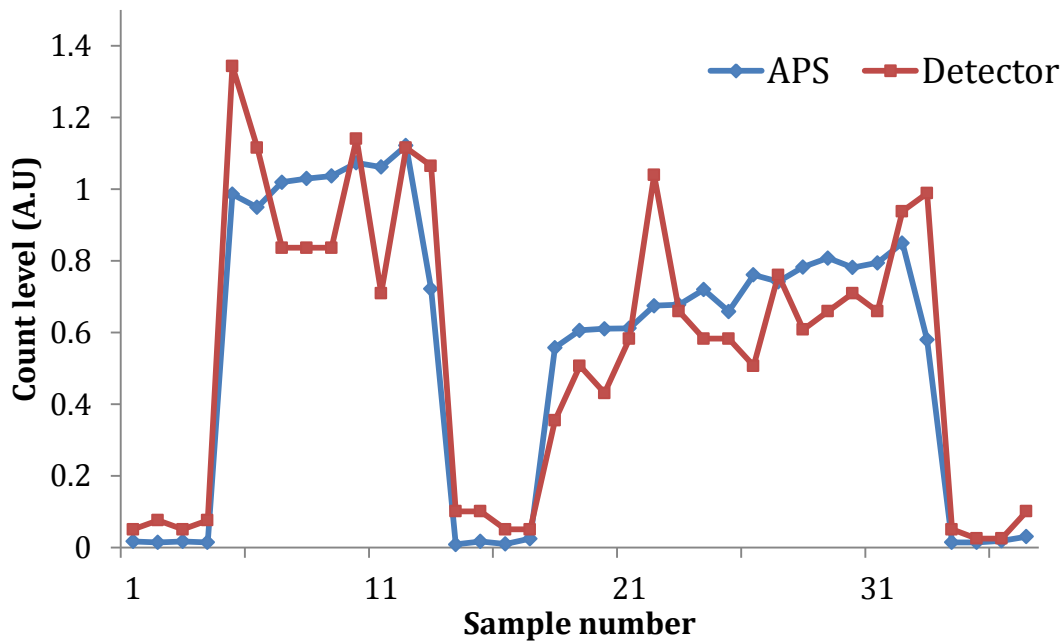


Figure 74 - Count levels of integrated device and APS measurement for 2 μm particle suspension over entire test period normalized to the average concentration of the highest particle concentration

6.5.2 1 μm Test Particles

The detector counts for 1 μm test particles demonstrate a similar trend with a number of counts too low for a statistically significant measurement for 1 minute sampling interval (Figure 75). When the average count is computed for each concentration, the linear correlation can be observed again. When the detector is compared with large particles generated in 1 μm solution shown in Figure 76, the detector counts does not appear to be better correlated to the larger particles. The result is ambiguous as the number of large particles is low due to the effect of the impactor. Similar to the 2 μm results, the continuous data in Figure 77 shows the detector is able to react to concentration changes with high variability due to the low number of counts.

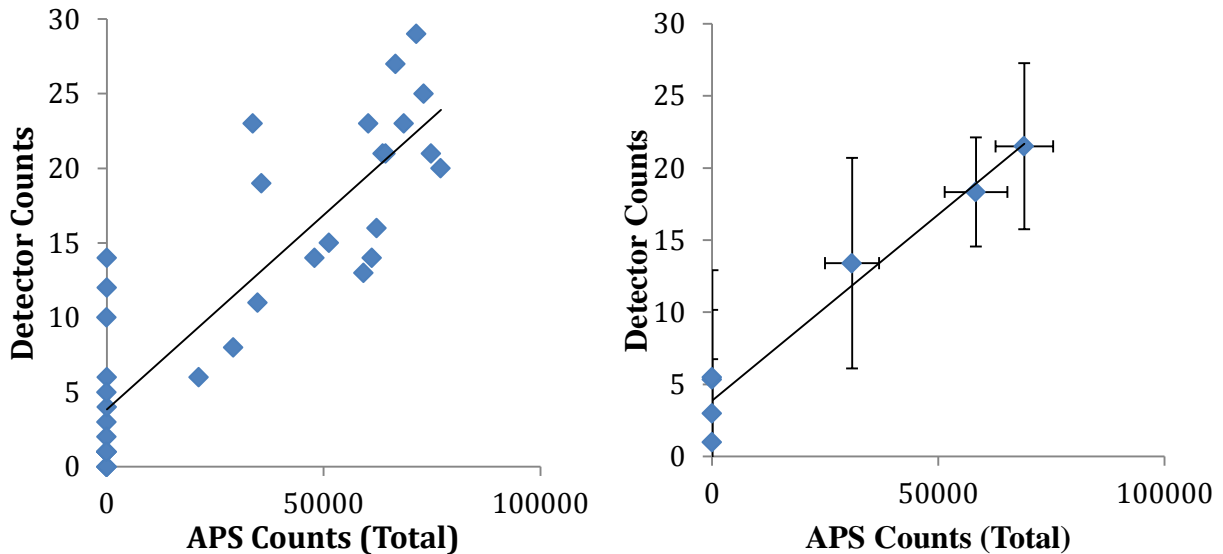


Figure 75 - Integrated device count (impactor and detector) vs total APS reference count for 1 μm particle suspension - Left: 1 minute sampling interval, Right: Average count for each particle concentration, error bars represents ± 1 standard deviation.

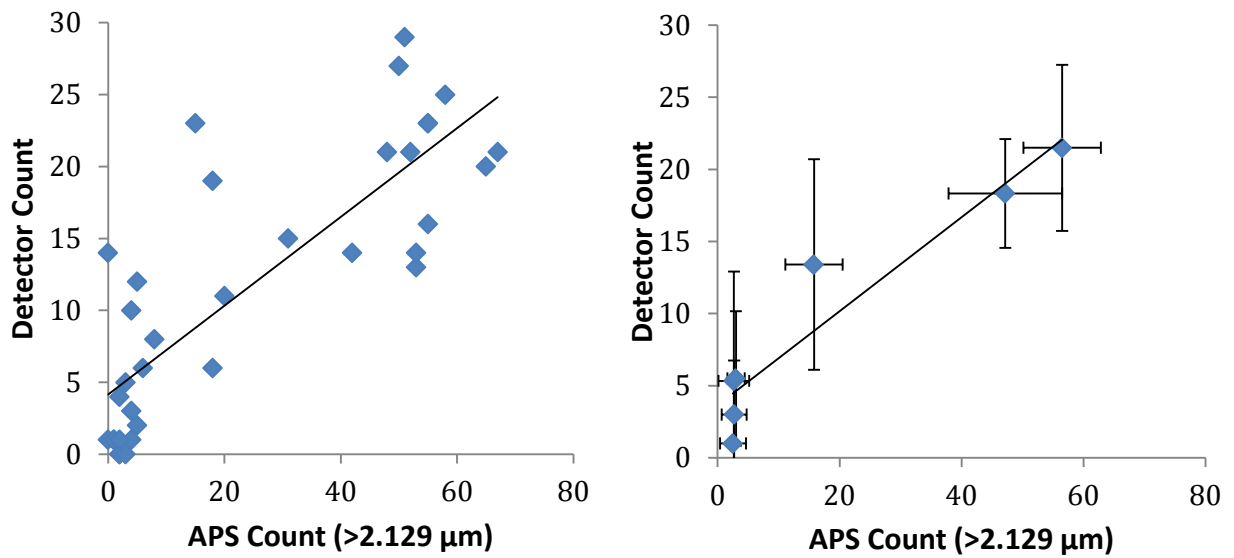


Figure 76 - Integrated device count (impactor and detector) vs APS reference count greater than 2.129 μm for 1 μm particle suspension - Left: 1 minute sampling interval, Right: Average count for each particle concentration, error bars represents ± 1 standard deviation.

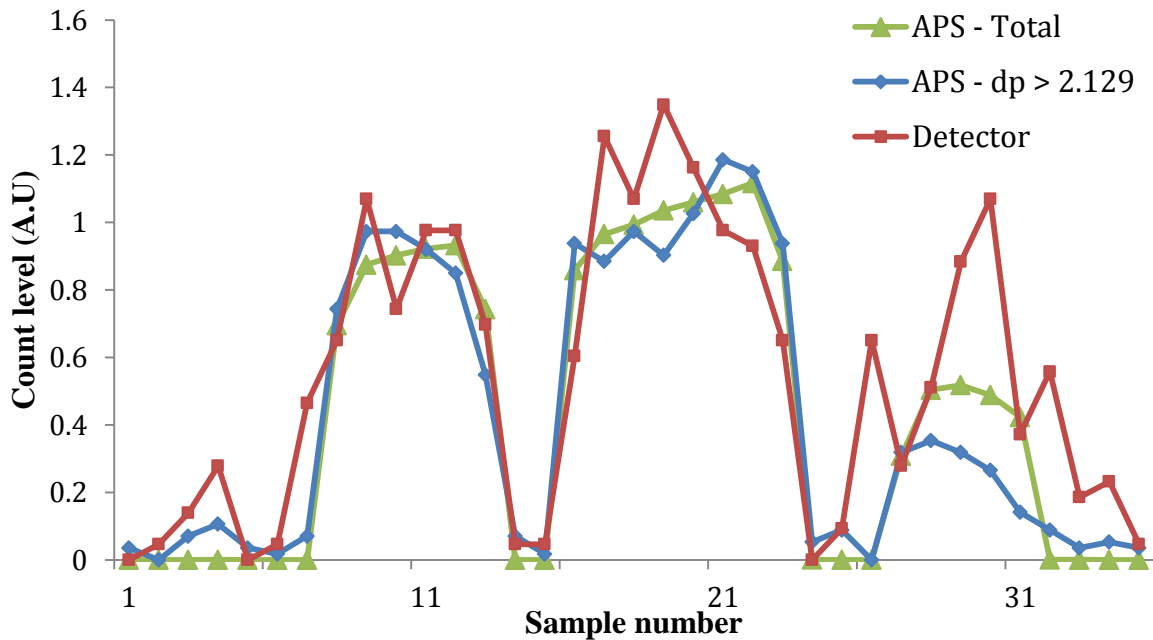


Figure 77 - Count levels of integrated device and APS measurement for 1 μm particle suspension over entire test period normalized to the average concentration of the highest particle concentration

7 Conclusions and Future Work

7.1 Conclusions

7.1.1 Particle Separation

A simple microfluidic-based particle separator based on the macroscopic particle trapping impactor concept is designed and demonstrated to capture airborne particles larger than $2.5 \mu\text{m}$. A stochastic model of particle counting is developed to determine the sufficient flow rate for a statistically significant measurement. The channel height h_0 and nozzle width W_0 are designed based on the Stokes and Reynolds numbers defined in literature. Analytical models describing the radial displacement and the stopping distance of particles are used to set the outlet angle ϕ_{out} and nozzle length L . The flow and particle behavior are simulated using COMSOL software to obtain the penetration efficiency curve. The geometry of the device such as the distance to impactor S_0 and the impactor entrance W_i is optimized through an iterative process. The shape of the acceleration inlet is also designed using COMSOL simulations by evaluating particle loss and the focusing effectiveness.

The fabricated impactor channel is tested by transmitting particles from 0.5 to $3 \mu\text{m}$ through the device and counting the number of particles at the outlet using an aerodynamic particle sizer. The experiment penetration efficiency curve is obtained by comparing the impactor outlet counts to the outlet count at an equivalent straight microchannel. The experimental penetration efficiency curve agrees with simulation results. The experimental 50% cut-off diameter is around $3 \mu\text{m}$, suitable for sizing PM 2.5. The $\sqrt{\text{Stk}_{50}}$ of the particle trapping impactor is found to be 0.67, comparable with impactor literature. The same methods can be used to design microfluidic-based impactors with a different 50% cut-off diameter.

With the inertial focusing inlet centering the particles from the side walls, the slope of the penetration curve is limited by particles travelling on the slower streamlines near the top and bottom wall. Microscope images of the particle trapping region indicate the impacted particles collide with the side wall of the particle trap and deposit in the nearby regions. Some impacted particles are carried deeper into the trap by a low velocity flow recirculation. Particle re-entrainment is a problem which persists in this design. As the deposition region near the impaction wall saturates after prolonged use of the device, the particles have a higher chance of re-entering the flow path. The impaction characteristics of the particles also appear to be sensitive to the humidity of the air.

7.1.2 Particle Detection

A low cost, real-time optical system capable of sensing individual particles has been demonstrated. The light scattering intensity is investigated by calculating the Mie scattering intensity using MIEPlot software for different particle sizes and illumination wavelengths. The best orientation of the components is determined by modeling the optical power of the scattered light on the photodetector surface. Based on these calculations, the requirements of the system to produce a sufficient signal to noise ratio is defined and the low cost, commercially available components are selected. The width of the expected signal pulse is calculated in designing the optical enclosure. Both the theoretical optical power and signal pulse are used in the design of the signal conditioning circuit to ensure the amplified signal is detectable. Finally, a solid model of the enclosure is created for the 3D printing of the enclosure. The 3D printed enclosure allows for easy alignment of optical components and quick design modifications, critical in optimizing the performance of the detector.

The detector is tested experimentally with 1, 1.5 and 2 μm particles. The pulse peak voltage from a single particle, which is a function of the particle size and the signal conditioning

and amplification, is comparable to the theoretical calculations. The pulse width, determined by the particle velocity and the sensing width, also agrees with the calculation. The signal to noise ratio is poor for the device ranging from 2 to 10, attributed to the high bandwidth of the device, the lack of noise isolation and the difficulty in stray light control for a forward scattering system.

The real-time characteristic of the detector is validated experimentally by comparing the detector counts and the APS reference counts. Without the microchannel, the detector counts show good correlation with the APS counts for 2 μm particles and are able to trace the concentration changes at 1 minute sampling interval. The count efficiency is reduced from 10 – 12 % to 0.2 – 0.5% for 1-1.5 μm particles. A longer sampling time is required to observe the correlation at low counting efficiency. Assuming the counting efficiency is consistent such that the lower detector count can be calibrated with the APS count, the estimated relative error for 1 μm , 1.5 μm and 2 μm measurements is 47%, 39% and 10% respectively. The detector only meets the initial design specifications for 2 μm . A summary of the current detector specification is shown in Table 18.

Table 18 - Current specification of the optical detector

Particle Diameter (μm)	Sampling Time (Minutes)	Counting Efficiency	Lowest Particle Concentration ($\mu\text{g}/\text{m}^3$)	Relative Error (%)	Mass Concentration Error ($\mu\text{g}/\text{m}^3$)
1	15	0.49	14.33	47	6.7
1.5	15	0.16	2.43	39	0.948
2	10	12	1.21	10	0.12

The integrated device is tested by attaching the microchannel to the detector as a replaceable cartridge. Including the microchannel does not affect the performance of the detector but the overall count is reduced due to particle loss at the connection interface. The correlation between count and concentration change is observed over a 10 minutes sampling interval. Due to the relatively low sampling rate in a micro-scale device, improving the counting efficiency is

especially important to achieve a statistically significant measurement. Stray light, particle loss at the device interface and lack of precise particle positioning are the main issues to be addressed in the future. Nonetheless, the experimental results demonstrate the feasibility of sizing particles with a microchannel and using low-cost optical components in a forward light scattering system to detect individual particles.

7.2 Future Work

7.2.1 Experimental Setup

The validation for particle trapping impactor is limited by the current experimental setup. Larger particles cannot be tested because of the limited size of the nebulizer droplets. Due to the limited availability of reference instruments, the straight and impactor microchannels are tested sequentially. Experimental error is likely introduced when the test device is switched between straight and impactor channels. A commercial particle generator (8108, TSI) is desirable to reliably generate particles at a fixed concentration. To minimize experimental error and obtain an instantaneous penetration efficiency value, both the straight and impactor microchannel should be tested in parallel by either using 2 reference instruments or another method of particle detection such as gravimetric analysis.

In order to further improve the design of the impactor, the particle deposition mechanism must be fully understood. In the current experimental setup, many variables which can potentially influence the impaction characteristics of the particle are not controlled during the experiment such as the particle charge, the air temperature and humidity. The electric charge on the particles can be eliminated with a charge neutralizer. Even if precise control of all the variables is not feasible, monitoring them with simple sensors such as thermocouples or humidity

sensors can improve the repeatability of the experiments and allow failure modes to be correlated to experiment conditions.

Another useful experiment in understanding particle deposition is to repeat the impactor test with fluorescent particles while imaging the particle trapping region in real-time. Higher time resolution images of the particle trapping region can be obtained, providing insights into where and how particles deposit around the impaction wall. The images can also be referenced to the APS counts to determine the failure conditions of the device.

7.2.2 Impactor Design

About 30% of larger particles are transmitted on the slow streamlines near the top and bottom walls of the impactor channel according to simulations. To improve the slope of the penetration efficiency curve, a vertical focusing mechanism should be implemented. This can be achieved using a sloped top and bottom walls similar to the sidewall. Alternatively, sheath air inlets can be added to the top and bottom of the channel by tuning the flow resistances to balance the flow rate of the channel. To address the issue of flow re-entrainment, the next step is to investigate methods of reducing the flow recirculation in the particle trapping region. Small features can be added within the trap to take advantage of the flow recirculation to capture the circulating particles. Finally, to maximize the number of particles entering the detector after separation, the particle loss at the microchannel to detector interface should be addressed. One possible method is to combine the impactor channel with the detector flow channel such that optical components are mounted on the PDMS chip to count particles. The eventual goal is to fabricate both subsystem with a monolithic process.

7.2.3 Detector Design

While forward scattering produces highest scattering intensity, implementing such a system is challenging. Because the detector and laser are in line, preventing stray light from entering into the detector is crucial in improving the signal to noise ratio. Focused light from the laser should be collimated to minimize the effect of spherical aberration on stray light and allow uniform beam intensity in the sensing region. A robust physical barrier is a preferred alternative for the light trap. Furthermore, minor fluctuations in the laser power can be amplified by the signal conditioning circuit. If the stray light cannot be blocked completely, maintaining a constant power for the emitting source is critical to reducing noise.

The signal to noise ratio can be further improved by addressing key design issues in the signal conditioning circuit. The design bandwidth in the transimpedance operational amplifier is set at 8 MHz which is not required to detect 0.03 ms pulses from the particles. An analog low-pass filter with a reasonably high corner frequency can be used to remove the high-frequency noise without distorting the signal. Because noise isolation is poor in the current prototype circuitry, the circuit is prone to high frequency noise and instability. The noise observed in the circuit can be reduced dramatically by implementing proper shielding and transferring the circuit onto a PCBA, replacing through-hole components with surface mount components.

BILIOGRAPHY

- [1] D. R. Gossett, W. M. Weaver, A. J. Mach, S. C. Hur, H. T. K. Tse, W. Lee, H. Amini, and D. D. Carlo, "Label-free cell separation and sorting in microfluidic systems," *Anal. Bioanal. Chem.*, vol. 397, no. 8, pp. 3249–3267, Apr. 2010.
- [2] B. Kuswandi, Nuriman, J. Huskens, and W. Verboom, "Optical sensing systems for microfluidic devices: A review," *Anal. Chim. Acta*, vol. 601, no. 2, pp. 141–155, Oct. 2007.
- [3] H. Zhang, C. H. Chon, X. Pan, and D. Li, "Methods for counting particles in microfluidic applications," *Microfluid. Nanofluidics*, vol. 7, no. 6, pp. 739–749, Aug. 2009.
- [4] K.-H. Kim, E. Kabir, and S. Kabir, "A review on the human health impact of airborne particulate matter," *Environ. Int.*, vol. 74, pp. 136–143, Jan. 2015.
- [5] M. Fu, F. Zheng, X. Xu, and L. Niu, "Advances of Study on Monitoring and Evaluation of PM2.5 Pollution," *Meteorol. Disaster Reduct. Res.*, no. 34, pp. 1–6, 2011.
- [6] D. W. Dockery, C. A. Pope, X. Xu, J. D. Spengler, J. H. Ware, M. E. Fay, B. G. Ferris, and F. E. Speizer, "An Association between Air Pollution and Mortality in Six U.S. Cities," *N. Engl. J. Med.*, vol. 329, no. 24, pp. 1753–1759, Dec. 1993.
- [7] D. G. Karottki, G. Bekö, G. Clausen, A. M. Madsen, Z. J. Andersen, A. Massling, M. Ketznel, T. Ellermann, R. Lund, T. Sigsgaard, P. Møller, and S. Loft, "Cardiovascular and lung function in relation to outdoor and indoor exposure to fine and ultrafine particulate matter in middle-aged subjects," *Environ. Int.*, vol. 73, pp. 372–381, Dec. 2014.
- [8] Y. Olsen, D. G. Karottki, D. M. Jensen, G. Bekö, B. U. Kjeldsen, G. Clausen, L.-G. Hersoug, G. J. Holst, A. Wierzbicka, T. Sigsgaard, A. Linneberg, P. Møller, and S. Loft, "Vascular and lung function related to ultrafine and fine particles exposure assessed by personal and indoor monitoring: a cross-sectional study," *Environ. Health*, vol. 13, no. 1, p. 112, Dec. 2014.

- [9] World Health Organization, “Review of evidence on health aspects of air pollution - REVIHAAP Project. Technical Report,” 2013.
- [10] World Health Organization, “Air Pollution and Cancer,” *IARC Sci. Publ.*, no. 161, 2013.
- [11] US Environmental Protection Agency, “Particulate Matter (PM 2.5) Speciation Guidance Document.” 22-Jul-1998.
- [12] World Health Organization, “WHO Air quality guidelines for particulate matter, ozone, nitrogen dioxide and sulfur dioxide: Global update 2005.” 2005.
- [13] U.S. Environmental Protection Agency, “National Ambient Air Quality Standards for Particulate Matter: Final Rule,” *Fed. Regist.*, vol. 78, no. 10, 2013.
- [14] US Environmental Protection Agency, “List of Designated Reference And Equivalent Methods.” 24-Aug-2010.
- [15] L. Han, W. Zhou, W. Li, and L. Li, “Impact of urbanization level on urban air quality: A case of fine particles (PM_{2.5}) in Chinese cities,” *Environ. Pollut.*, vol. 194, pp. 163–170, Nov. 2014.
- [16] R. Lagravinese, F. Moscone, E. Tosetti, and H. Lee, “The impact of air pollution on hospital admissions: Evidence from Italy,” *Reg. Sci. Urban Econ.*, vol. 49, pp. 278–285, Nov. 2014.
- [17] M. Zhou, G. He, M. Fan, Z. Wang, Y. Liu, J. Ma, Z. Ma, J. Liu, Y. Liu, L. Wang, and Y. Liu, “Smog episodes, fine particulate pollution and mortality in China,” *Environ. Res.*, vol. 136, pp. 396–404, Jan. 2015.
- [18] F. Lu, D. Xu, Y. Cheng, S. Dong, C. Guo, X. Jiang, and X. Zheng, “Systematic review and meta-analysis of the adverse health effects of ambient PM_{2.5} and PM₁₀ pollution in the Chinese population,” *Environ. Res.*, vol. 136, pp. 196–204, Jan. 2015.

- [19] M. Gao, S. K. Guttikunda, G. R. Carmichael, Y. Wang, Z. Liu, C. O. Stanier, P. E. Saide, and M. Yu, "Health impacts and economic losses assessment of the 2013 severe haze event in Beijing area," *Sci. Total Environ.*, vol. 511, pp. 553–561, Apr. 2015.
- [20] C. K. Chan and X. Yao, "Air pollution in mega cities in China," *Atmos. Environ.*, vol. 42, no. 1, pp. 1–42, Jan. 2008.
- [21] S. C. Fang, A. Cassidy, and D. C. Christiani, "A Systematic Review of Occupational Exposure to Particulate Matter and Cardiovascular Disease," *Int. J. Environ. Res. Public Health*, vol. 7, no. 4, pp. 1773–1806, Apr. 2010.
- [22] M. L. Kile, S. Fang, A. A. Baccarelli, L. Tarantini, J. Cavallari, and D. C. Christiani, "A panel study of occupational exposure to fine particulate matter and changes in DNA methylation over a single workday and years worked in boilermaker welders," *Environ. Health*, vol. 12, no. 1, p. 47, Jun. 2013.
- [23] R. E. Moran, D. H. Bennett, J. Garcia, and M. B. Schenker, "Occupational exposure to particulate matter from three agricultural crops in California," *Int. J. Hyg. Environ. Health*, vol. 217, no. 2–3, pp. 226–230, Mar. 2014.
- [24] J. D. Spengler and Q. Chen, "Indoor Air Quality Factors in Designing a Healthy Building," *Annu. Rev. Energy Environ.*, vol. 25, no. 1, pp. 567–600, 2000.
- [25] V. S. Chithra and S. M. Shiva Nagendra, "Impact of outdoor meteorology on indoor PM10, PM2.5 and PM1 concentrations in a naturally ventilated classroom," *Urban Clim.*, vol. 10, Part 1, pp. 77–91, Dec. 2014.
- [26] N. H. Wong and B. Huang, "Comparative study of the indoor air quality of naturally ventilated and air-conditioned bedrooms of residential buildings in Singapore," *Build. Environ.*, vol. 39, no. 9, pp. 1115–1123, Sep. 2004.

- [27] ASHRAE, “ANSI/ASHRAE Standard 62.1-2010. Ventilation for acceptable indoor air quality.” American Society of Heating, Refrigerating, and Air-Conditioning Engineers, Inc., 2010.
- [28] A. I. Dounis, M. Bruant, G. Guarracino, P. Michel, and M. Santamouris, “Indoor air-quality control by a fuzzy-reasoning machine in naturally ventilated buildings,” *Appl. Energy*, vol. 54, no. 1, pp. 11–28, May 1996.
- [29] V. A. Marple and B. A. Olson, “Sampling and Measurement Using Inertial, Gravitational, Centrifugal, and Thermal Techniques,” in *Aerosol Measurement*, P. Kulkarni, P. A. Baron, and K. Willeke, Eds. John Wiley & Sons, Inc., 2011, pp. 129–151.
- [30] V. A. Marple, K. L. Rubow, and S. M. Behm, “A microorifice uniform deposit impactor (MOUDI): Description, calibration, and use,” *Aerosol Sci. Technol.*, vol. 14, no. 4, pp. 434–446, 1991.
- [31] R. C. Flagan, “Electrical Mobility Methods for Submicrometer Particle Characterization,” in *Aerosol Measurement*, P. Kulkarni, P. A. Baron, and K. Willeke, Eds. John Wiley & Sons, Inc., 2011, pp. 339–364.
- [32] Y.-S. Cheng, “Instruments and Samplers Based on Diffusional Separation,” in *Aerosol Measurement*, P. Kulkarni, P. A. Baron, and K. Willeke, Eds. John Wiley & Sons, Inc., 2011, pp. 365–379.
- [33] D. J. Rader and V. A. Marple, “Effect of ultra-Stokesian drag and particle interception on impaction characteristics,” *Aerosol Sci. Technol.*, vol. 4, no. 2, pp. 141–156, 1985.
- [34] S. V. Hering, R. C. Flagan, and S. K. Friedlander, “Design and evaluation of new low-pressure impactor. I,” *Environ. Sci. Technol.*, vol. 12, no. 6, pp. 667–673, Jun. 1978.

- [35] S. V. Hering, S. K. Friedlander, J. J. Collins, and L. W. Richards, "Design and evaluation of a new low-pressure impactor. 2," *Environ. Sci. Technol.*, vol. 13, no. 2, pp. 184–188, Feb. 1979.
- [36] V. A. Marple, B. Y. H. Liu, and R. M. Burton, "High-volume Impactor for Sampling Fine and Coarse Particles," *J. Air Waste Manag. Assoc.*, vol. 40, no. 5, pp. 762–767, May 1990.
- [37] V. A. Marple and J. E. McCormack, "Personal Sampling Impactor with Respirable Aerosol Penetration Characteristics," *Am. Ind. Hyg. Assoc. J.*, vol. 44, no. 12, pp. 916–922, Dec. 1983.
- [38] V. A. Marple and B. Y. Liu, "Characteristics of laminar jet impactors," *Environ. Sci. Technol.*, vol. 8, no. 7, pp. 648–654, 1974.
- [39] V. A. Marple and K. Willeke, "Impactor design," *Atmospheric Environ. 1967*, vol. 10, no. 10, pp. 891–896, 1976.
- [40] C.-J. Tsai and T.-Y. Lin, "Particle collection efficiency of different impactor designs," *Sep. Sci. Technol.*, vol. 35, no. 16, pp. 2639–2650, 2000.
- [41] C.-J. Tsai and Y.-H. Cheng, "Solid particle collection characteristics on impaction surfaces of different designs," *Aerosol Sci. Technol.*, vol. 23, no. 1, pp. 96–106, 1995.
- [42] V. A. Marple and C. M. Chien, "Virtual impactors: a theoretical study," *Environ. Sci. Technol.*, vol. 14, no. 8, pp. 976–985, 1980.
- [43] P. Biswas and R. C. Flagan, "The particle trap impactor," *J. Aerosol Sci.*, vol. 19, no. 1, pp. 113–121, 1988.
- [44] D. S. Kim, K. W. Lee, and Y. J. Kim, "Characterization of a particle trap impactor," *J. Aerosol Sci.*, vol. 37, no. 8, pp. 1016–1023, 2006.
- [45] H. T. Kim, Y. T. Han, Y. J. Kim, K. W. Lee, and K. J. Chun, "Design and Test of 2.5 μ m Cutoff Size Inlet Based on a Particle Cup Impactor Configuration," *Aerosol Sci. Technol.*, vol. 36, no. 2, pp. 136–144, 2002.

- [46] E. R. Lennox, N. M. Kreisberg, and L. D. Montoya, "Design and Characterization of a New Coarse Particle Collector Based on Microtrap Impactor Technology," *Aerosol Sci. Technol.*, vol. 47, no. 6, pp. 626–633, 2013.
- [47] Y.-H. Kim, J.-Y. Maeng, D. Park, I.-H. Jung, J. Hwang, and Y.-J. Kim, "Micromachined cascade virtual impactor with a flow rate distributor for wide range airborne particle classification," *Appl. Phys. Lett.*, vol. 91, no. 4, p. 043512, 2007.
- [48] J. S. Kang, K. S. Lee, K. H. Lee, H. J. Sung, and S. S. Kim, "Characterization of a Microscale Cascade Impactor," *Aerosol Sci. Technol.*, vol. 46, no. 9, pp. 966–972, 2012.
- [49] C.-J. Tsai, C.-N. Liu, S.-M. Hung, S.-C. Chen, S.-N. Uang, Y.-S. Cheng, and Y. Zhou, "Novel active personal nanoparticle sampler for the exposure assessment of nanoparticles in workplaces," *Environ. Sci. Technol.*, vol. 46, no. 8, pp. 4546–4552, 2012.
- [50] D. Park, Y.-H. Kim, C. W. Park, J. Hwang, and Y.-J. Kim, "New bio-aerosol collector using a micromachined virtual impactor," *J. Aerosol Sci.*, vol. 40, no. 5, pp. 415–422, 2009.
- [51] A. Schaap, W. C. Chu, and B. Stoeber, "Continuous size-separation of airborne particles in a microchannel for aerosol monitoring," *IEEE Sens. J.*, vol. 11, no. 11, pp. 2790–2797, 2011.
- [52] E. Weingartner, H. Burtscher, C. Hüglin, and K. Ehara, "Semi-Continuous Mass Measurement," in *Aerosol Measurement*, P. Kulkarni, P. A. Baron, and K. Willeke, Eds. John Wiley & Sons, Inc., 2011, pp. 255–268.
- [53] C. M. Sorensen, J. Gebhart, T. J. O'Hern, and D. J. Rader, "Optical Measurement Techniques: Fundamentals and Applications," in *Aerosol Measurement*, P. Kulkarni, P. A. Baron, and K. Willeke, Eds. John Wiley & Sons, Inc., 2011, pp. 269–312.
- [54] X. Wang, G. Chancellor, J. Evenstad, J. Farnsworth, A. Hase, G. Olson, A. Sreenath, and J. Agarwal, "A Novel Optical Instrument for Estimating Size Segregated Aerosol Mass Concentration in Real Time," *Aerosol Sci. Technol.*, vol. 43, no. 9, pp. 939–950, Sep. 2009.

- [55] A. L. Northcross, R. J. Edwards, M. A. Johnson, Z.-M. Wang, K. Zhu, T. Allen, and K. R. Smith, "A low-cost particle counter as a realtime fine-particle mass monitor," *Environ. Sci. Process. Impacts*, vol. 15, no. 2, pp. 433–439, Feb. 2013.
- [56] T. I. Anderson, D. s. Covert, S. f. Marshall, M. I. Laucks, R. j. Charlson, A. p. Waggoner, J. a. Ogren, R. Caldow, R. I. Holm, F. r. Quant, G. j. Sem, A. Wiedensohler, N. a. Ahlquist, and T. s. Bates, "Performance Characteristics of a High-Sensitivity, Three-Wavelength, Total Scatter/Backscatter Nephelometer," *J. Atmospheric Ocean. Technol.*, vol. 13, no. 5, pp. 967–986, Oct. 1996.
- [57] Y.-S. Cheng, "Condensation Particle Counters," in *Aerosol Measurement*, P. Kulkarni, P. A. Baron, and K. Willeke, Eds. John Wiley & Sons, Inc., 2011, pp. 381–392.
- [58] S. Dhaniyala, M. Fierz, J. Keskinen, and M. Marjamäki, "Instruments Based on Electrical Detection of Aerosols," in *Aerosol Measurement*, P. Kulkarni, P. A. Baron, and K. Willeke, Eds. John Wiley & Sons, Inc., 2011, pp. 393–416.
- [59] S. M. Stanley, G. McHale, M. I. Newton, C. J. Percival, and C. R. Evans, "An EP-SAW for measurements of particulate matter in ambient air," *Nondestruct. Test. Eval.*, vol. 20, no. 1, pp. 3–7, Mar. 2005.
- [60] I. Paprotny, F. Doering, P. A. Solomon, R. M. White, and L. A. Gundel, "Microfabricated air-microfluidic sensor for personal monitoring of airborne particulate matter: Design, fabrication, and experimental results," *Sens. Actuators Phys.*, vol. 201, pp. 506–516, Oct. 2013.
- [61] A. Hajjam, J. C. Wilson, and S. Pourkamali, "Individual Air-Borne Particle Mass Measurement Using High-Frequency Micromechanical Resonators," *IEEE Sens. J.*, vol. 11, no. 11, pp. 2883–2890, Nov. 2011.
- [62] E. Mehdizadeh, J. C. Wilson, A. Hajjam, A. Rahafrooz, and S. Pourkamali, "Aerosol impactor with embedded MEMS resonant mass balance for real-time particulate mass

concentration monitoring,” in *2013 Transducers Eurosensors XXVII: The 17th International Conference on Solid-State Sensors, Actuators and Microsystems (TRANSDUCERS EUROSENSORS XXVII)*, 2013, pp. 661–664.

[63] D. Liang, W.-P. Shih, C.-S. Chen, and C.-A. Dai, “A Miniature System for Separating Aerosol Particles and Measuring Mass Concentrations,” *Sensors*, vol. 10, no. 4, pp. 3641–3654, Apr. 2010.

[64] M. Mauro, R. Battaglia, G. Ferrini, R. Puglisi, D. Balduzzi, and A. Galli, “Single microparticles mass measurement using an AFM cantilever resonator,” *ArXiv14101953 Phys.*, Oct. 2014.

[65] K. Chun, H. C. Kim, S. Kim, Y. Kim, S. Lee, K. Min, S. Lim, and J. Lee, “MEMS for TPMS and exhaust of automobiles,” in *2012 IEEE Sensors*, 2012, pp. 1–4.

[66] S.-G. Lee, J. Hyun, D. Park, J. Hwang, and Y.-J. Kim, “Application and performance test of a micro-machined unipolar charger for real-time measurements of exhaust particles from a diesel engine vehicle,” *J. Aerosol Sci.*, vol. 42, no. 11, pp. 747–758, Nov. 2011.

[67] H. H. Lim, D. Park, J. Y. Maeng, J. Hwang, and Y. J. Kim, “MEMS Based Integrated Particle Detection Chip for Real Time Environmental Monitoring,” in *19th IEEE International Conference on Micro Electro Mechanical Systems, 2006. MEMS 2006 Istanbul*, 2006, pp. 62–65.

[68] X. Li, E. Iervolino, F. Santagata, J. Wei, C. A. Yuan, P. M. Sarro, and G. Q. Zhang, “Miniaturized particulate matter sensor for portable air quality monitoring devices,” in *2014 IEEE SENSORS*, 2014, pp. 2151–2154.

[69] A. Stuart and K. Ord, *Kendall’s Advanced Theory of Statistics: Distribution Theory v. 1*, 6th Edition edition. London : New York: Wiley-Blackwell, 1994.

- [70] M. D. Allen and O. G. Raabe, "Slip Correction Measurements of Spherical Solid Aerosol Particles in an Improved Millikan Apparatus," *Aerosol Sci. Technol.*, vol. 4, no. 3, pp. 269–286, Jan. 1985.
- [71] C. F. Bohren and D. R. Huffman, *Absorption and Scattering of Light by Small Particles*. John Wiley & Sons, 2008.
- [72] I. Sokolik, A. Andronova, and T. C. Johnson, "Complex refractive index of atmospheric dust aerosols," *Atmospheric Environ. Part Gen. Top.*, vol. 27, no. 16, pp. 2495–2502, Nov. 1993.
- [73] National Instruments, "NI USB-6501 Low-Cost USB Digital I/O Device." .
- [74] Texas Instruments, "OPA846 - Wideband, Low-Noise, Voltage-Feedback OPERATIONAL AMPLIFIER." Dec-2008.
- [75] A. van der Meulen, A. Plomp, F. Oeseburg, E. Buringh, R. M. van Aalst, and W. Hoevers, "Intercomparison of optical particle counters under conditions of normal operation," *Atmospheric Environ. 1967*, vol. 14, no. 4, pp. 495–499, 1980.
- [76] MicroChem Corp., "SU-8 2000 Permanent Epoxy Negative Photoresist - Processing guidelines for SU-8 2025, SU-8 2035, SU-8 2050 and SU-8 2075." .
- [77] Stratasy, "Objet24 Product Specifications." 2014.
- [78] R. A. Gussman, *Note on the particle-size output of Collison nebulizer*, vol. 45. Amer Industiral Hygiene Assoc., 1984.
- [79] N. Sandler, K. Reiche, J. Heinämäki, and J. Yliruusi, "Effect of Moisture on Powder Flow Properties of Theophylline," *Pharmaceutics*, vol. 2, no. 3, pp. 275–290, Jul. 2010.
- [80] S. Karner and N. Anne Urbanetz, "The impact of electrostatic charge in pharmaceutical powders with specific focus on inhalation-powders," *J. Aerosol Sci.*, vol. 42, no. 6, pp. 428–445, Jun. 2011.

APPENDIX A – Impactor Width W_i Simulation Data

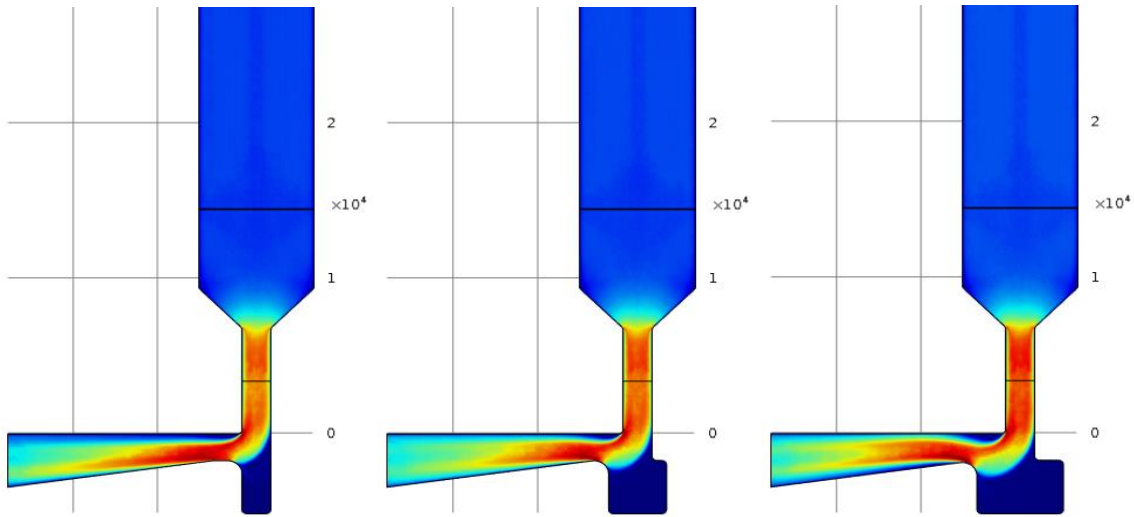


Figure 78 - Flow velocity field for Impactor width $W_i = W_0, 1.5 W_0$ and $2W_0$ (Not to same colour scale).

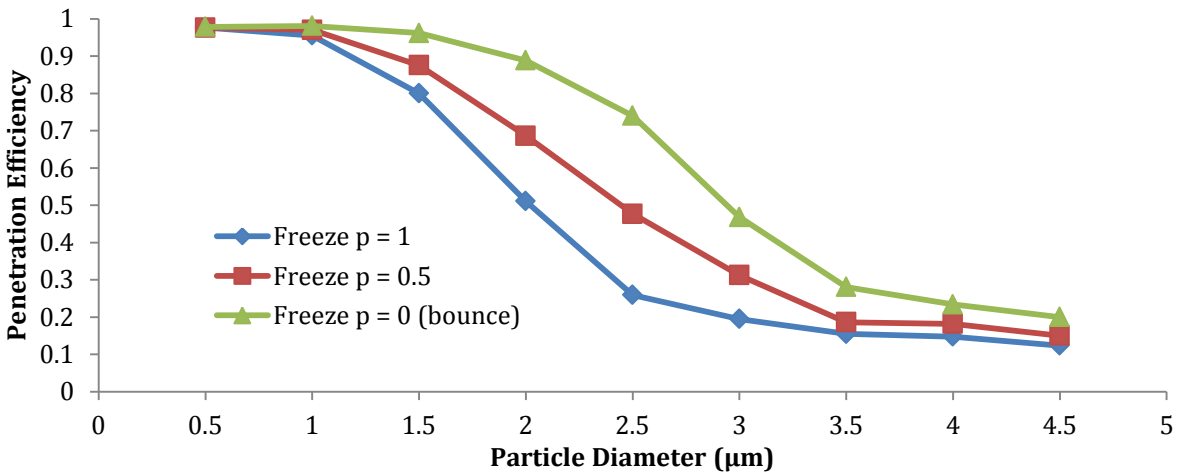


Figure 79 - Penetration efficiency for $W_i = W_0$ for freeze, 50% freeze and bounce wall condition

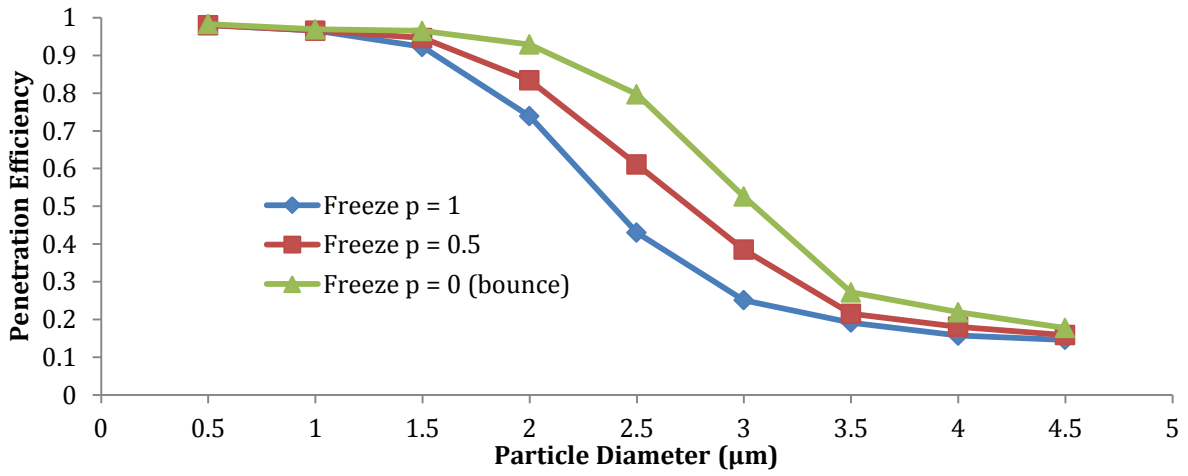


Figure 80 - Penetration efficiency for $W_i = 1.5W_0$ for freeze, 50% freeze and bounce wall condition

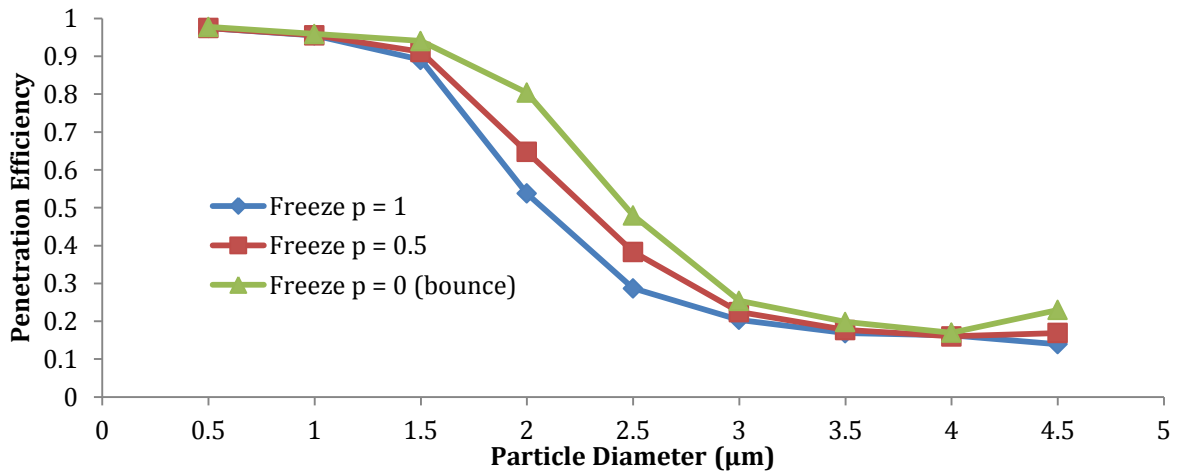


Figure 81 - Penetration efficiency for $W_i = 2W_0$ for freeze, 50% freeze and bounce wall condition